Die approbierte Originalversion dieser Diplom-/Masterarbeit ist in der Hauptbibliothek der Technischen Universität Wien aufgestellt und zugänglich.
http://www.ub.tuwien.ac.at

The approved original version of this diploma or master thesis is available at the main library of the Vienna University of Technology.
http://www.ub.tuwien.ac.at/eng

Diplomarbeit

$MgO/Mg(OH)_2$ as thermochemical energy storage materials in a fluidized bed reactor

carried out for the purpose of obtaining the academic degree of Diplom-Ingenieur (Dipl.-Ing.)
under the supervision of

Ao.Univ.Prof. Dipl.-Ing. Dr.techn. Andreas WERNER

and

Projektass. Dipl.-Ing. Felix Birkelbach

Institute of Energy Systems and Thermodynamics / E302

submitted at Vienna University of Technology

Faculty of Mechanical and Industrial Engineering

by

Alexander Bartik

01327352

Steudelgasse 36/20
1100 Vienna

Vienna, November 12, 2018

Affidavit

I, Alexander Bartik, hereby declare

1. that I am the sole author of the present thesis, '$MgO/Mg(OH)_2$ as thermochemical energy storage materials in a fluidized bed reactor', 110 pages, bound and that I have not used any source or tool other than those referenced or any other illicit aid or tool.
2. that I have not prior to this date submitted this thesis as an examination paper in any form in Austria or abroad.

November 12, 2018 Alexander Bartik

Acknowledgments

Es gilt an dieser Stelle einigen Menschen zu danken, die es mir ermöglicht haben, diese Arbeit in jenem Maße abzuschließen, in der sie jetzt vorliegt.
Allen voran bedanke ich mich bei Felix Birkelbach. Seine Tür stand für mich immer offen und durch seine Kompetenz und sein Wissen, sowie durch die unzähligen wertvollen Diskussionen, konnte ich mich dem Ziel schrittweise annähern. Danke Felix!
Mein besonderer Dank gilt auch Andreas Werner, der jederzeit ein offenes Ohr für mich hatte und durch dessen herzliche Art ich mich sofort willkommen geheißen fühlte.
Gerd Mauschitz und Thomas Laminger danke ich dafür, dass sie sich völlig uneigennützig bereit erklärt haben, mir bei meinen Fragestellungen bezüglich der Partikelcharakterisierung weiter zu helfen.
Dass ich mich auch in den fremden Gefilden der FH Wels zurechtfand, die den Startpunkt für diese Arbeit darstellte, bedanke ich mich bei Thomas Aigenbauer.
Auch möchte ich Sabrina Schönberger nennen, die mich im Zuge ihrer Bachelorarbeit bei der Versuchsdurchführung wesentlich unterstützte.
Nicht zuletzt danke ich auch meinen Freunden, die sich die Zeit genommen haben, diese Arbeit zu lesen und zu korrigieren.
Danke euch!

Abstract

Thermochemical energy storage (TCES) is a promising new technology to increase efficiency and support sustainable energy generation with distinct advantages compared to other thermal energy storage systems.

In this thesis, the magnesium oxide/magnesium hydroxide system is experimentally investigated in a fluidized bed reactor (FBR) for its applicability as a TCES material pair. Basic fluid dynamic quantities, mechanical stability, hydration and dehydration kinetics as well as reversibility under repetitive reaction conditions are determined. For testing, two different types of material are considered (carbonate-bases/hydroxide-based).

Overall, materials show good fluidization behavior. Mechanical stability is given for all investigated conditions, except for hydroxide-based material under stress of dehydration. The influence of reaction parameters on hydration/dehydration kinetics is clearly shown. At 0.4 bar partial steam pressure and 80 °C as well as 0.6 bar and 100 °C, 60 % to 80 % conversion is reached after 3 h with a maximum conversion rate of about $2 \times 10^{-4}\,\mathrm{s}^{-1}$. At 0.4 bar and 100 °C conversion stays below 20 %.

Carbonate-based material exhibits an acceleration of kinetics after the initial cycle up to a maximum of $5 \times 10^{-4}\,\mathrm{s}^{-1}$. Dehydration, with a fivefold increase in specific surface area (SSA) compared to initial material, is found to be the reason. Hydroxide-based material is accompanied by a surface area increase up to tenfold, but it shows fast deterioration for consecutive cycles. Carbonate-based material is more stable under repetitive reaction conditions.

Compared to lab-scale simultaneous thermal analysis (STA) experiments, kinetic improvement is achieved. From second cycle hydration on, a maximum discharge power of about $1\,\frac{\mathrm{kW}}{\mathrm{kg}}$ is possible. Discharge capacity is, however, limited to 50 % of maximum value, even if a lower discharge power is accepted.

The investigated reaction system shows sufficient properties for application as a possible low temperature storage material. Especially if materials are further optimized, also in regard to utilization in a FBR, their applicability as TCES system could be enhanced.

Kurzfassung

Thermochemische Energiespeicherung stellt eine vielversprechende, neuartige Technologie zur Effizienzsteigerung und zur Unterstützung bei der Erzeugung nachhaltiger Energie dar, wobei ausgeprägte Vorteile zu anderen thermischen Energiespeicherkonzepten bestehen.
Im Rahmen dieser Arbeit wird das Reaktionssystem bestehend aus Magnesiumoxid und Magnesiumhydroxid in einem Wirbelschichtreaktor experimentell auf die Eignung als thermochemisches Speichermaterial untersucht. Dabei werden fluiddynamische Grundgrößen, mechanische Stabilität, Hydratisierungs- und Dehydratisierungskinetik, als auch die Reversibilität der Reaktion unter mehrzyklischer Beanspruchung bestimmt. Zur Untersuchung stehen karbonatstämmige und hydroxidstämmige Materialien zur Verfügung.
Alle Materialien zeigen grundsätzlich gutes Wirbelverhalten. Mechanische Stabilität ist, bis auf hydroxidstämmiges Material unter Dehydratisierungsbedingungen, unter allen untersuchten Bedingungen gegeben. Auch der Einfluss von Reaktionsbedingungen auf die Hydratisierungs- bzw. Dehydratisierungskinetik geht eindeutig aus den Daten hervor. Bei einem Dampfpartialdruck von 0,4 bar und 80 °C sowie bei 0,6 bar und 100 °C können Umsätze von 60 % bis 80 % nach 3 h erreicht werden. Maximale Umsatzraten liegen dabei bei ungefähr $2 \cdot 10^{-4}\,\mathrm{s}^{-1}$. Hingegen führen 0,4 bar und 100 °C nur zu Umsätzen <20 %.
Karbonatstämmiges Material zeigt verbesserte Kinetik nach abgeschlossenem ersten Zyklus mit Umsatzraten bis $5 \cdot 10^{-4}\,\mathrm{s}^{-1}$. Eine gegenüber dem Ausgangsmaterial verfünffachte spezifische Partikeloberfläche nach abgeschlossener Dehydratisierungsreaktion wurde als Ursache für die gesteigerte Hydratisierungskinetik identifiziert. Hydroxidstämmiges Material geht mit einer bis zu Verzehnfachung der Oberfläche einher, nachfolgende Zyklen führen aber zu einer substantiellen Materialdegradierung. Karbonatstämmiges Material zeigt hierbei verbesserte Stabilität.
Im Vergleich zu Ergebnissen aus simultanen thermischen Analysen im Kleinstmaßstab, kann eine verbesserte Kinetik erreicht werden. Ab dem 2.Zyklus sind Ausspeicherleistungen bis zirka $1\,\frac{\mathrm{kW}}{\mathrm{kg}}$ möglich. Die Ausspeicherkapazität bleibt aber auf 50 % des Maximalwerts beschränkt, auch bei Inkaufnahme niedriger Leistungen.
Für die mögliche Anwendung als Niedertemperaturenergiespeicher besitzt das Reaktionspaar ausreichende Eigenschaften. Materialoptimierung, auch hinsichtlich Wirbelverhalten, könnte die Anwendbarkeit als thermochemisches Speichersystem weiter ausbauen.

Contents

1 Introduction

Scientific advancements have allowed humanity to prosper and flourish. However, technological innovations, which enabled the worlds population to grow rapidly in the first place, now need to provide a basis for the transition towards a sustainable future.

A main area of interest concerning this issue is the energy sector. Global energy consumption is rising constantly, especially in emerging countries. Total global energy demand is now at about 500 EJ [31]. It is estimated that the energy demand will continue to expand by 30 % until 2040. The total primary energy supply (TPES) grew by 27 % between 2000 and 2010, with Asia accounting for 70 % of the global TPES increment. China alone doubled its TPES during this time. Over 80 % of the total TPES growth in this time was accounted for by fossil fuels. It is therefore evident that fossil fuels still play a major role in the energy supply. An indicator for the long lasting use of fossil fuels are increasing greenhouse gas (GHG) emissions. In 2010, 35 % of all anthropogenic GHG emissions originated from the energy supply sector. Asia was the largest emitter, with a share of 41 % [7]. Another factor that supports a transition towards renewable energies, is the limited availability of fossil fuels. Today 50 % of the conventional oil reserves and 30 % of the natural gas reserves are consumed. Coal is available in large quantities, especially if the uneconomic resources are counted as well [23]. However, with fossil fuel reserves and resources that are currently estimated to be available, there is sufficient CO_2, if released, to exceed the targeted global mean temperature change of 2 °C by far [7].

Climate change can only be mitigated and global temperature can only be stabilized, if the total amount of CO_2 emitted is limited and emissions eventually approach zero [1]. Hence, mitigation options are necessary. Besides many others, renewable energy systems are a crucial technology to achieve this goal. In 2010 renewable energy provided 13.5 % of the TPES and 21 % of the global electricity supply. In 2040, renewable energy will account for 40 % of electricity production [32]. However, according to a scenario (global renewable energy supply until 2050) issued by WBGU [56], it is necessary to reduce energy consumption to achieve this goal.

Table 1.1 gives an overview of the theoretical, technical and economical potential of different renewable energy sources. The table shows that the required energy could be easily covered by renewable energy sources. It should be noted that the realized economic potential in the table is dated to the year 2000. Especially wind (5-fold) and solar energy (25-fold) grew substantially in this time (2005-2012)[32, 25].

In the following section the focus is laid on electricity production by renewable energies. In order to convert energy, there are various different technologies available. Hydropower is the largest contributor to the renewable energy mix with an installed capacity of over 950 GW out of nearly 1500 GW in 2012 (biomass is not taken into account) [32]. Other realizations are tidal power, ocean waves or ocean currents, which are rather limited.

Wind energy has a high theoretical potential. However, only a small amount is accessible. Furthermore the intermittent availability (20 percent of the total time on shore and 40 percent off shore) is a main obstacle [25]. Nevertheless, wind energy grew at a rate of 20 % annually in 2010 and 2011 [32].

Table 1.1: Annual potential of Renewable Energy in exajoule, adapted from [25]

Source	Theoret. potential	Techn. potential	Econ. potential (2000)
Sunlight	5,500,000	8,000	0.1
Wind	100,000	10 to 20	0.1
Hydro	120	15-20	10
Biomass	3000-3900	1,200	840
Heat from earth interior	600,000,000	1-4	1
Heat from air, water and soil	10,000	10-30	about 3

Solar energy offers by far the largest potential. Due to the recent cost reduction, photovoltaics exhibit the largest growth rates (78 % in 2010 and 41 % in 2011 [32]). Beside PV-cells, solar hot water production is also an important part in the energy mix. Solar energy, however, also has a downside: power supply is restricted by cloud coverage and daylight hours.

For the sake of completeness, other major renewable energy technologies are mentioned as well: biomass conversion (thermally and materially), geothermal power plants and heat pumps.

As mentioned, both wind energy and solar energy are dependent on weather conditions and thus highly fluctuating resources. Hence, they cannot provide baseload power or cover peak loads. Without the implementation of wind and solar energy (by relying solely on renewable baseload energy like biomass and hydropower), a shift towards total renewable energy supply is not realistic, if technical potentials of different technologies are kept in mind.

The following example demonstrates this problem on the basis of the Ontario electricity data (taken from [29]). Fig. 1.1a shows electricity demand and wind energy supply for Ontario from November 1st to November 16th, 2016. In order to balance demand and supply, assuming a complete transformation to wind power, the installed capacity would have to increase 13-fold. This theoretical scenario is shown in Fig. 1.1b. Supply and demand appear with temporal differences. Using the data, calculation shows, that an additional 900 000 MW h of energy storage is necessary in order to equalize fluctuations and thus ensure a stable electrical grid (graphics by [41]).

Energy storage technologies are therefore mandatory, if fossil fuels are to be gradually replaced by renewable energy carriers ([53] and [16] for example, also mention other aspects worth researching and provide deeper insights on why energy storage is necessary).

There are already many different technologies available, more being developed today. In general, it is possible to distinguish among the following principles:

- Mechanical storage: pumped hydro, compressed air energy storage, flywheels, ...
- Chemical storage: hydrogen, power-to-gas
- Electrochemical storage: batteries, supercapacitors
- Thermal storage: sensible, latent, thermochemical energy storage

Thermochemical energy storage is a novel concept enhancing the possibilities of thermal energy storage methods. These methods can be applied where heat is available as waste product or

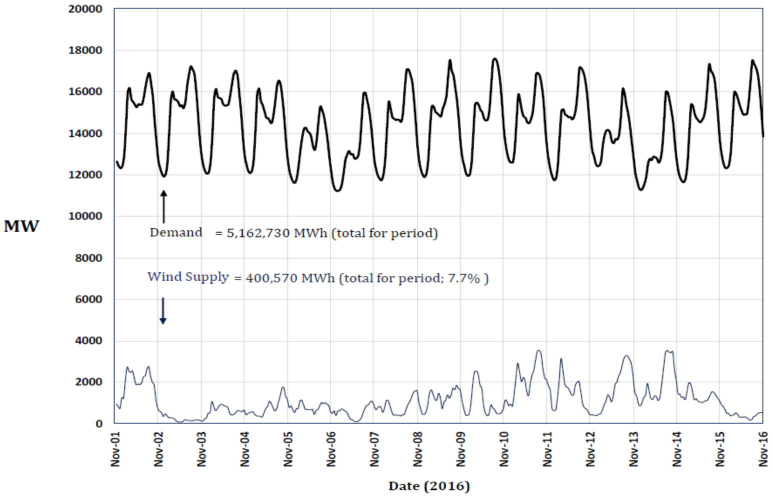

(a) original data

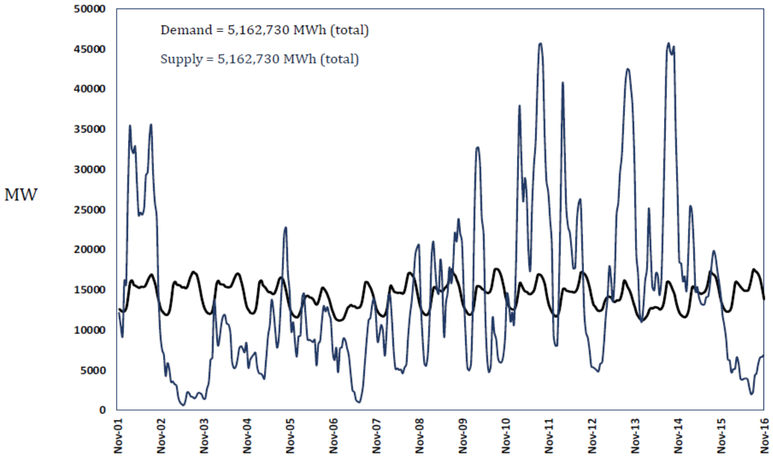

(b) Demand and supply balanced

Figure 1.1: Ontario electricity demand and wind supply, from [41]

temporal or spatial supply/demand discrepancies need to be bridged. Sensible and latent heat storage systems are already implemented, but show some drawbacks, e. g. low energy density, limited storage temperatures, losses due to storage at elevated temperature/pressure, ... As will be seen below, TCES can overcome these limitations and therefore poses a promising new technology.

2 Aim of this work

The thermochemical system of magnesium oxide (MgO) and magnesium hydroxide ($Mg(OH)_2$) was identified as a promising TCES material. Kato et al. already conducted a kinetic study [34] and determined durability characteristics [33] of the hydration reaction of MgO in fixed bed reactors. A thermogravimetric analysis (TGA) on the effect of calcination conditions on the properties of magnesia was done by Lui et al. [40]. However, so far, no data investigating the behavior of the materials and the overall reversible chemical reaction in a FBR is known to the author.

In the present work the performance of $MgO/Mg(OH)_2$ in a fluidized bed reactor is assessed. The goal is to determine limitations of the process with respect to thermochemical energy storage, optimal reaction conditions and to identify areas, where improvements can be made. To this end the following tests will be performed:

- Basic fluid dynamic quantities required for characterization in a FBR
- Qualitative fluidization behavior
- Abrasion and fragmentation under cold flow conditions
- Kinetic evaluation of hydration reaction under varying parameters
- Kinetic evaluation of dehydration reaction under varying parameters
- Cycle experiments and stability

The material is then quantitatively analyzed in order to answer the questions above. Planning, designing and construction of the test rig is not part of this work.

3 Theoretical background

In this work, different scientific disciplines are combined. A basic understanding of energy technology, thermodynamics, chemistry and fluid dynamics is beneficial to follow the outlined investigations. In this chapter some relevant information is provided.

3.1 Thermochemical energy storage

3.1.1 Basics

TCES is based on a reversible chemical reaction. Hence, the material changes its composition during the storage process. The fundamental process is given by the following reaction equation:

$$\nu_{\mathrm{A}}\,\mathrm{A}_{(\mathrm{s})} + \Delta\mathrm{H}_{\mathrm{R}} \rightleftharpoons \nu_{\mathrm{B}}\,\mathrm{B}_{(\mathrm{s})} + \nu_{\mathrm{C}}\,\mathrm{C}_{(\mathrm{g})} \tag{3.1}$$

Material B reacts with gaseous component C to form a solid component A while releasing energy in the amount of the reaction enthalpy ΔH_R. If the reaction occurs in this direction it is referred to as the discharging reaction. The charging reaction is therefore the reversed process, where material A decomposes into solid B and gas C, while storing energy. By storing the two components separately the reverse reaction cannot take place, enabling close to lossless storage at ambient temperature and pressure for an indefinite amount of time. By using gas-solid reactions, as depicted in Eq. 3.1, separation of components is simple. Additional energy may be required, depending on the aggregate condition of the gaseous component at standard conditions. TCES is not limited to gas-solid reactions. Solid-liquid or liquid-gas reactions can be used in a TCES system as well. The focus in this chapter is on gas-solid reactions.

Fig. 3.1 depicts the fundamental principle of TCES. In reactor 1 the charging reaction takes place. As heat carrier an inert gas is used, in general. Gas C is released and componenet B is formed. Depending on the reaction system, the gas may need to be stored (closed process). This is mostly the case when the gas should not be released into the atmosphere and/or heat recovery is intended. Such a design is more complex, because of the need for a condenser/evaporator. If water vapor is used, for example, an open process may be preferred due to its simplicity. The discharge reaction in reactor 2 utilizes gas C and solid B to form A and release stored heat. This setup allows the charging and discharging process to be done at different locations, transporting the material in between.

If heat supply and demand only differs temporally, but not spatially, an *integrated reactor concept* can be applicable. Here, both reactions are realized as batch process in the same reactor, reducing costs. As a result, all storage material needs to be kept in the reactor, resulting in large reactors, less storage efficiency and decreased response time. In an *external reactor concept* the reactor is separated from a storage material reservoir. The power of the storage system is decoupled from storage capacity, increasing its flexibility. Material transportation is required, however [35].

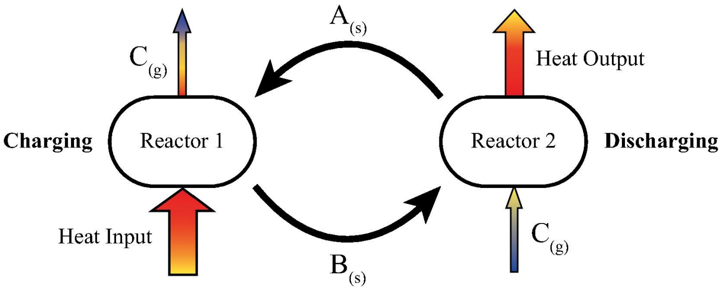

Figure 3.1: Fundamental TCES principle, from [12]

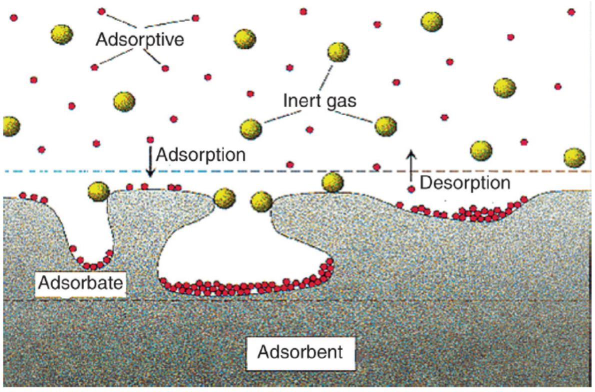

Figure 3.2: Schematic adsorption and desorption process, from [35]

Another type of TCES is the sorption process. The adsorption/desorption phenomena describes interaction between a fluid and the surface of a solid. The reaction equation can be written as (gas-solid reaction):

$$\mathrm{A_{(s)} + xB_{(g)} \longleftrightarrow A \cdot xB_{(s)} + \Delta H_{ads}} \tag{3.2}$$

Fig. 3.2 depicts the schematic adsorption/desorption process. If a molecule in the gas phase (adsorptive) approaches the adsorbent due to diffusion or convection, the molecule gets immobilized on the surface of the solid. The adsorbed molecule is called adsorbate. Due to this fixation, thermal energy is released (ΔH_{ads} in Eq. 3.2). Depending on the properties of the adsorbent, other molecules might get adsorbed to a certain degree or remain completely inert. If the process is reversible, the same amount of energy is needed to overcome bonding forces and release the adsorbed species back into the gas phase. A further differentiation leads to the terms of physisorption (physical adsorption) and chemisorption (chemical adsorption). In the first case only physical forces, like *van der Waals* forces are involved. Chemisorption, however, is defined by a chemical bond between adsorbent and adsorbate [35].

Equilibrium is typically given by adsorption isotherms. The solid loading X is expressed as a function of partial pressure p_i at constant temperature T (Eq. 3.3). Many models exist based on different assumptions (e. g. Langmuir, Freundlich, BET-model).

$$X = f(p_i)_T \tag{3.3}$$

These isotherms show, that adsorption processes are favored at low temperatures and high partial pressures, whereas desorption takes place at high temperatures and low partial pressures. In addition, adsorption enthalpy is a function of loading X. In order to calculate the stored/released energy Q, the integral of enthalpy over loading X needs to be solved. Often, a mean adsorption enthalpy is used instead.

$$Q = m_{\mathrm{ads}} \Delta X \int_{X_{\mathrm{des}}}^{X_{\mathrm{ads}}} \Delta h_{\mathrm{ads}}(X) \tag{3.4}$$

Preferred sorption materials possess properties including a high adsorption capacity, high heat of adsorption, fast reaction kinetics and, depending in the application, appropriate adsorption/desorption temperatures. They are characterized by a high porosity and a large inner surface area. Typical materials are silica gel, zeolite and activated carbon [35].

3.1.2 Applications

Possible applications for thermochemical energy storage are summarized here. TCES can utilize untapped industrial waste heat, which is unavoidable and therefore increase the limited efficiency inherent with these processes. The TCES system has to be simple enough for it to be economically feasible. Otherwise waste heat would have been utilized with existing processes already. It can also help in covering peak loads in power plant applications, where load changes are challenging and efficiency reducing.

In concentrated solar power (CSP) applications it can be used as a buffer to equalize supply/demand discrepancies or as the primary heat carrier medium. For domestic applications it can be used in combination with solar thermal energy. Especially in summer these systems are often stagnant, whereas in winter required energy is missing. TCES could promote implementation of a heat displacement system.

3.1.3 TCES materials

Various gas-solid reactions have been proposed and examined by different authors for the application in TCES. Research in this area is, however, still in an early stage. Most of the experiments are conducted on a lab-scale and no TCES material is commercially available today. In Table 3.1 a selection of possible reaction systems is given. The list should be seen as an excerpt and is not complete. Aydin et al. [2], Kerskes [35], Pardo et al. [45] or Cot-Gores et al. [10] provide overviews on researched reaction systems.

Table 3.1: Materials for TCES

Reaction type	Reaction
Salt hydrates	$MgSO_4 \cdot 7\,H_2O \rightleftharpoons MgSO_4 + 7\,H_2O$ $CaCl_2 \cdot 6\,H_2O \rightleftharpoons CaCl_2 \cdot H_2O + 5\,H_2O$
Ammonium chlorides	$CaCl_2 \cdot 4\,NH_3 \rightleftharpoons CaCl_2 \cdot 2\,NH_3 + 2\,NH_3$
Metal hydrides	$MgH_2 \rightleftharpoons Mg + H_2$ $CaH_2 \rightleftharpoons Ca + H_2$
Metal carbonates	$CaCO_3 \rightleftharpoons CaO + CO_2$ $PbCO_3 \rightleftharpoons PbO + CO_2$
Metal hydroxides	$Mg(OH)_2 \rightleftharpoons MgO + H_2O$ $Ca(OH)_2 \rightleftharpoons CaO + H_2O$
Metal oxides (Redox systems)	$2\,BaO_2 \rightleftharpoons 2\,BaO + O_2$ $2\,Co_3O_4 \rightleftharpoons 6\,CoO + O_2$

Salt hydrate and ammonium chloride systems are based on sorption processes and can be used in low temperature applications. Often, composite materials are used in order to enhance reaction kinetics, improve heat and mass transfer or to shift reactions temperatures to the required level for a certain application. Hongois et al. [27] used a $MgSO_4$/zeolite composite. Li et al. [39] proposes a $CaCl_2/NH_3$ working pair (T_{eq} <100 °C) for a radiant floor heating system. Metal hydrates are utilized at higher temperatures – CaH_2 for heat storage between 950 °C and 1100 °C [45]. MgH_2 was investigated, among others, by Bogdanovic et al. [6]. The operating temperature ranges from 250 °C to 500 °C. This system shows drawbacks, like slow reaction kinetics, sintering, high operating pressure and a need for doping [45].

A material, which is already well know from limestone production is $CaCO_3$. Temperature range is again high at 700 °C to 1000 °C. It has a high energy density, is readily available and cheap. Disadvantages include agglomeration, sintering and poor reactivity. It can also be used for carbon sequestration technology. An alternative system is $PbCO_3$ which was studied for CHP applications at temperatures from 300 °C to 1457 °C. It is problematic due to its toxicity and it also shows poor reversibility [45].

In the medium temperature range metal hydroxides are predominant. $Ca(OH)_2$ (350 °C - 900 °C) was already studied by many authors (e. g. [42, 49, 21]). Therefore a solid experimental basis exists. Another distinct advantage is the operating pressure at atmospheric conditions [45]. $Mg(OH)_2$ is discussed more comprehensively later.

Reactions that just recently got in the focus of the attention for solar applications, are redox reactions with metal oxides. BaO_2 (130 °C - 1000 °C) and Co_3O_4 (700 °C - 900 °C) are the most promising candidates. Wong et al. [57] investigated other metal oxides as well. Block et al. [5] used a binary system based on Co_3O_4/CoO and Fe_2O_3/Fe_3O_4 to adjust the reaction temperature suitable for CSP.

Requirements

In general, various reaction systems possess the fundamental thermodynamic properties (see section 3.2.1) to function as TCES materials. However, for a successful implementation or before large scale testing, most of the following prerequisites need to be fulfilled. Some of these requirements differ from application to application.

- A high energy density is required. This value represents how much energy can be stored per kg or m^3 of material.
- Equilibrium temperature needs to be at an appropriate level. This depends mainly on the application. Temperature ranges for possible applications cover a wide field and TCES systems need to be chosen accordingly.
- Kinetics should be sufficiently fast in order to release/store energy within an acceptable time span. One could talk about the storage power (how much energy can be stored in a certain amount of time). This depends on the application again. Kinetics have to comply with dynamics of the application. Furthermore, slow kinetics reduce efficiency. An important factor influencing kinetics, is the specific surface area of particles.
- Charge temperatures should not be too high, discharge temperatures not too low. The greater temperature deviations from equilibrium temperature at constant pressure, the lower the efficiency. Kinetics, however depend on the 'distance' from equilibrium as will be discussed later. A trade off is necessary.
- Mechanical stability: This includes effects like sintering, agglomeration, abrasion through mechanical stress and fragmentation.
- Chemical stability: No side reactions, complete reversibility and high yields. In order to be practically applicable, at least 100 cycles without significant material deterioration are required [33]. The required cycle stability, however, also depends on the intended amount of cycles for an economically feasible operation.
- Low cost per amount of energy stored; abundance and availability, non-corrosiveness as well as non-toxicity.
- Simple systems: There should only be one gaseous species. Otherwise, separation would be necessary.
- Stability of the substance; no reverse reaction while the material is stored.
- High heat conductivity.

Comparison

Compared to the other two types of thermal energy storage, namely sensible and latent heat storage, TCES is characterized by certain advantages. All the substances listed above have high energy densities. Therefore, less material is needed for the same amount of stored energy, resulting in smaller reactors and lower transportation and material costs. Also, energy can be stored over a theoretically unlimited time, because storage takes place at ambient temperature, thus eliminating energy losses due to heat transfer, in contrast to latent and sensible TES methods. Additionally, the solids are usually stable components and do not alter their physical properties over time, if the reverse reaction can be prevented (e. g. store in a dry place, if the gaseous component is water). The fact, that there are hardly any losses, enables long

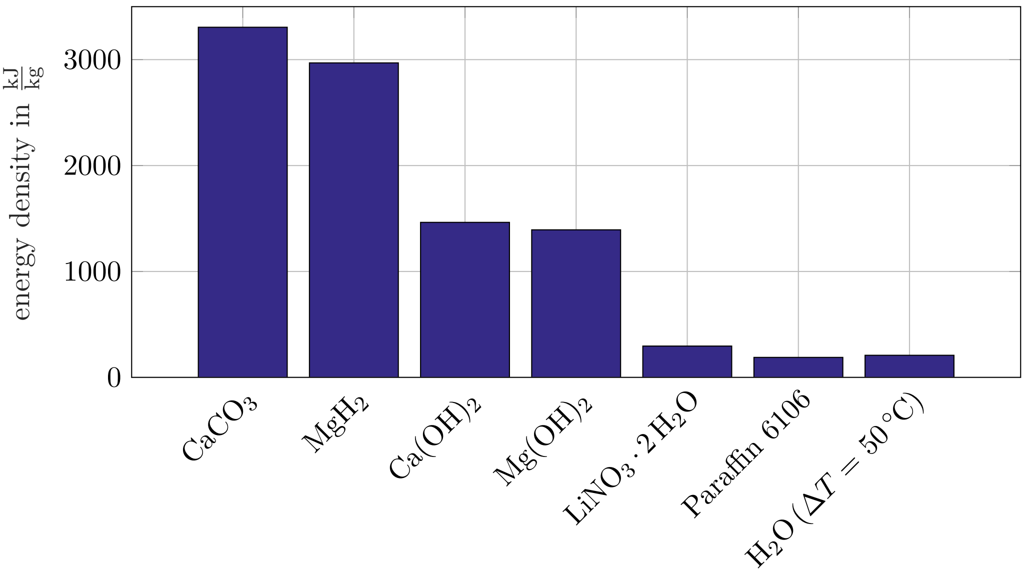

Figure 3.3: Comparison of energy densities

distance material transportation. However, considering energy requirement for transportation, efficiency might be reduced substantially.
These points pose main advantages compared to other systems and give reason to further intensify research. In particular, because TCES is a complex technology and the fundamentals of gas-solid interactions are not fully understood. Also, only lab-scale testing has been carried out so far.
In Fig. 3.3 energy densities of different types of TES materials are compared. The four substances starting from the left are TCES materials, as described above. Energy densities are much higher compared to other storage technologies. Note, that these values are calculated, using standard heat of formations ΔH_f^0 and molar masses taken from [8] and [24]. Thus, values are theoretical and represent a maximum, assuming ideal behavior. Phase change materials (PCM) are typically salt hydrates, such as $LiNO_3 \cdot 2\,H_2O$, or organic compounds like paraffin [51]. As the most important sensible storage medium, water is depicted.

3.2 Chemical equilibrium and kinetics

3.2.1 Chemical equilibrium

There are two phenomena dominating chemical reactions: chemical equilibrium and reaction rates. Knowledge of both is mandatory in order to fully describe a chemical reaction and therefore also to design a chemical reactor. In general, if a system is in a state of equilibrium, back and forth reactions occur at same speed (dynamic equilibrium). This state can be described by the equilibrium conversion. Note, that equilibrium is independent from kinetics, i. e. increased reaction speed does not influence equilibrium. However, equilibrium, as well as reaction rates are a function of temperature, pressure and composition of reactants, in general. If, for example, a certain reaction is exothermic, increased temperature diminishes conversion at equilibrium. Simultaneously, the reaction exhibits faster kinetics at higher temperatures.

Thus, a compromise has to be found. In other words, parameters exist with an economically optimal trade-off between kinetics and equilibrium.
In this work, the focus is on gas-solid reactions, since the investigated reaction (Eq. 3.5) is of this kind.

$$MgO_{(s)} + H_2O_{(g)} \rightleftharpoons Mg(OH)_{2(s)} \tag{3.5}$$

In the following section thermodynamic fundamentals are depicted.
One of the most important relations in chemical thermodynamics is Gibbs fundamental equation (Eq. 3.6). It is derived by combining the first and second law of thermodynamics.

$$\mathrm{d}H^t = V^t\mathrm{d}p + T\mathrm{d}S^t \tag{3.6}$$

The Gibbs energy is defined by Eq. 3.7.

$$G^t = H^t - TS^t \tag{3.7}$$

The complete differential according to Eq. 3.7 is $\mathrm{d}G^t = \mathrm{d}H^t - T\mathrm{d}S^t - S^t\mathrm{d}T$. Substituting $\mathrm{d}H^t$ with Eq. 3.6 results in

$$\mathrm{d}G^t = -S^t\mathrm{d}T + V^t\mathrm{d}p. \tag{3.8}$$

The complete differential of $G^t(T, p, \mathbf{n})$ for a multi-component system with $\mathbf{n} = [n_1\, n_2 \ldots n_N]$ species is

$$\mathrm{d}G^t = \left(\frac{\partial G^t}{\partial T}\right)_{p,n_i} \mathrm{d}T + \left(\frac{\partial G^t}{\partial p}\right)_{T,n_i} \mathrm{d}p + \sum_{i=1}^{N} \left(\frac{\partial G^t}{\partial n_i}\right)_{T,p,n_{j\neq i}} \mathrm{d}n_i. \tag{3.9}$$

Equating coefficients of Eq. 3.9 and Eq. 3.8 gives

$$\mathrm{d}G^t = -S^t\mathrm{d}T + V^t\mathrm{d}p + \sum_{i=1}^{N} \mu_i \mathrm{d}n_i, \tag{3.10}$$

where the last term is the definition of the chemical potential μ_i. The change of molar amount $\mathrm{d}n_i$ can be written as $\mathrm{d}n_i = \nu_i\, \mathrm{d}\varepsilon$ using reaction coordinate $\mathrm{d}\varepsilon$ and stoichiometric coefficient ν_i . ε is useful, because it describes reaction progress independent of species i.
In a closed system the second law of thermodynamic states that the equilibrium state is characterized by a maximum of entropy. Eq. 3.7 shows that this is equal to a minimum of Gibbs energy at constant T and p. Therefore, it can be written as $(\mathrm{d}G)_{T,p} = 0$. If this is applied to Eq. 3.10 at constant temperature and pressure, the condition for chemical equilibrium translates to

$$\left(\frac{\mathrm{d}G^t}{\mathrm{d}\varepsilon}\right)_{T,p} = \sum_{i=1}^{N} \nu_i \mu_i = 0. \tag{3.11}$$

In general, chemical potential of real gas in a mixture is given by Eq. 3.12. The first term denotes the chemical potential of the pure substance at T,p (subscript 0 stands for pure substance). The second term is the correction due to an ideal mixture and the third term accounts for real gas behavior.

$$\mu_i(T,p,x_i) = \mu_{0i}(T,p) + RT\,\ln x_i + RT\,\ln\varphi_i(T,p,\mathbf{x}) \tag{3.12}$$

The summability equation states, that the chemical potential of a pure substance is equal to the molar Gibbs-function.

$$\mu_{0i}(T,p) = G_{0i}(T,p) \tag{3.13}$$

Plugging Eq. 3.12 into Eq. 3.11 yields Eq. 3.14.

$$\sum_i^N \nu_i\mu_i(T,p) = \sum_i^N \nu_i\mu_{0i}(T,p) + RT\sum_i^N \ln x_i + RT\sum_i^N \ln\varphi_i(T,p,\mathbf{x}) = 0 \tag{3.14}$$

The first term can be written as

$$\begin{aligned}\sum_i^N \nu_i\mu_{0i}(T,p) = \sum_i^N \nu_i G_{0i}(T,p) = \sum_i^N \nu_i H_{f,i}(T,p) - T\sum_i^N \nu_i S_{f,i}(T,p) = \\ = \Delta H_R(T,p) - T\Delta S_R(T,p) = \Delta G_R(T,p).\end{aligned} \tag{3.15}$$

H_f is the heat of formation and S_f the entropy of formation. ΔG_R is called reaction Gibbs energy, ΔH_R reaction enthalpy and ΔS_R reaction entropy.

The pressure dependency of the Gibbs energy for the fluid phase (here: steam as ideal gas (IG)) is calculated with (superscript 0 denotes standard pressure p^0)

$$G_{0i}(T,p) = \mu_{0i}(T,p) = G^0_{0i}(T) + \int_{p^0}^{p} v_i \mathrm{d}p = G^0_{0i}(T) + \underbrace{RT\ln\frac{p}{p^0}}_{IG}. \tag{3.16}$$

The last variables which need to be calculated are molar Gibbs energies at operating temperature T and p^0. Using the definition of the Gibbs energy (Eq. 3.7), $G^0_{0i}(T)$ can be computed by calculating standard heat of formation and standard entropy of formation at T, p^0. These two variables are listed in thermodynamic tables for many different substances at thermochemical standard condition (TCSC) at $T = 298.15\,\mathrm{K}$, $p^0 = 1\,\mathrm{bar}$. Temperature correction to operating temperature T can easily be determined, using specific heat capacities c_p^0 according to Eq. 3.17 and Eq. 3.18.

$$\begin{aligned}G^0_{0i}(T) = G_{0i}(T,p^0) = H^0_{f,i}(T) - TS^0_{f,i}(T) = \\ = H^0_{f,i}(T_0) + \int_{T_0}^{T} c^0_{p,i}\mathrm{d}T - T\left(S^0_{f,i}(T_0) + \int_{T_0}^{T}\frac{c^0_{p,i}}{T}\mathrm{d}T\right)\end{aligned} \tag{3.17}$$

Temperature depency of specific heat capacity c_p^0 is often described by a polynomial. Coefficients a,b,c,d are specific for each substance and can be found in databases.[1]

$$c_p^0(T) = a + b\,T + c\,T^{-2} + d\,T^2 \tag{3.18}$$

For calculation of chemical equilibrium of the MgO/Mg(OH)$_2$ system, following Eq. 3.1, some assumptions are made. First, the solid species are assumed to be pure and to have negligible

---

[1] [8] gives a different polynomial with different coefficients

pressure influences. Second, steam is assumed to be an ideal gas, neglecting real behavior and therefore correction terms including fugacity f_i and fugacity coefficients φ_i.
For the MgO/Mg(OH)$_2$ system, Eq. 3.11 can thus be simplified to

$$-\mu^0_{0,\mathrm{MgO}} - \mu_{0,\mathrm{H_2O}} + \mu^0_{0,\mathrm{Mg(OH)_2}} = 0. \tag{3.19}$$

This translates to

$$-G^0_{0,\mathrm{MgO}}(T) + G^0_{0,\mathrm{Mg(OH)_2}}(T) - G^0_{0,\mathrm{H_2O}}(T) - RT\,ln\frac{p_{H2O}}{p^0} = 0. \tag{3.20}$$

Gibbs energy of the pure substance at standard pressure can be summarized to the reaction Gibbs energy similar to Eq. 3.15. This leaves a simple equation to determine equilibrium pressure for varying temperature T.

$$ln\frac{p_{\mathrm{H_2O}}}{p_0} = -\frac{\Delta G^R(T, p^0)}{RT} \tag{3.21}$$

This is in accordance with the phase rule. There is one degree of freedom. Therefore Mg(OH)$_2$ decomposes at fixed pressure at fixed T and vice versa. With the help of computational tools, the equilibrium curve as shown in Fig. 3.4 is created. Used values are summarized in Table 3.2.

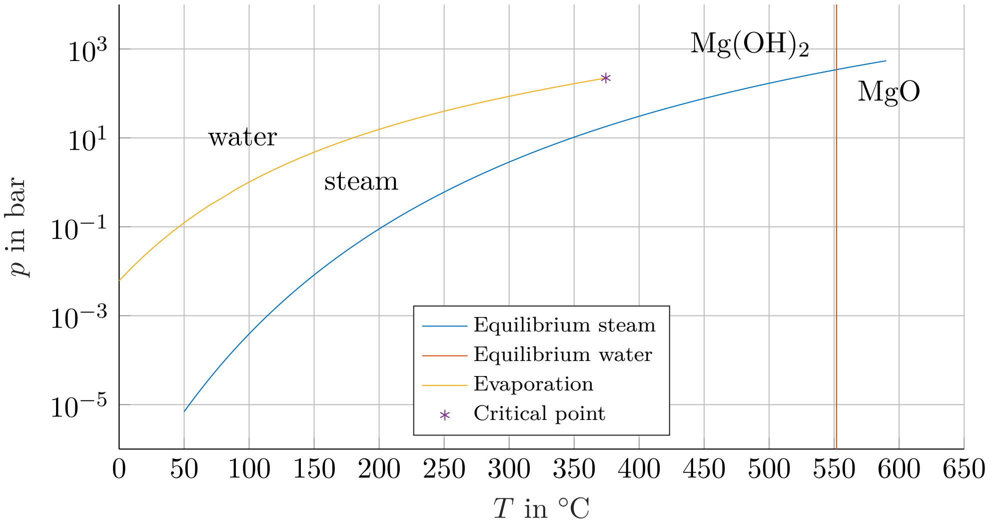

Figure 3.4: Equilibrium curve of MgO/Mg(OH)$_2$ for steam and water plus vapor pressure curve of water with critical point

For experimentation, partial pressures between 0.2 bar and 0.6 bar and temperatures between 75 °C and 100 °C are used. These values are very close to the dew point. They are chosen because reaction kinetics improve with distance to the equilibrium curve. The yellow line shows limitations of this process. Lower temperatures at constant pressure are not possible because condensation takes place. If parameters fall below the vapor pressure line, liquid water is present and the red equilibrium curve is valid. It is, in good approximation (assuming that water is incompressible), independent of pressure and lies at a temperature of 551.8 °C. For hydration this means that the driving force for the reaction is much higher and thus reaction rates should be higher. Or stated differently, much higher reaction temperatures are

Table 3.2: Thermodynamic data of MgO/Mg(OH)2 [2]

	MgO	H_2O	$Mg(OH)_2$
ΔH_f^0 in $\frac{\mathrm{kJ}}{\mathrm{mol}}$	601.6	241.826	924.664
ΔS_f^0 in $\frac{\mathrm{J}}{\mathrm{mol\,K}}$	26.95	188.832	63.137
a in $\frac{\mathrm{J}}{\mathrm{mol\,K}}$	47.485	28.408	100.055
b in $\frac{\mathrm{J}}{\mathrm{mol\,K^2}}$	4.648	12.447	18.337
c in $\frac{\mathrm{J\,K}}{\mathrm{mol}}$	-10.34	1.284	-25.255
d in $\frac{\mathrm{J}}{\mathrm{mol\,K^3}}$	-0.268	0.360	-0.017

theoretically possible. Steam would have to be pressurized to 343 bar to achieve the same equilibrium temperature. Dehydration can nevertheless be done at lower temperatures using the steam equilibrium curve. The problem is, that the reaction heats up excessive water. Its heat capacity would increase, but temperatures would stay low. Also, liquid water would evaporate before it can react with the solid and the blue curve applies again. A lot of energy would be ‘lost’ to evaporation. Pressure would have to be increased to allow higher temperature reactions with water.

3.2.2 Kinetics

Reaction kinetics provide information on the speed of a reaction. It determines whether thermodynamic equilibrium can be reached. For example, species B of a certain reaction might be thermodynamically stable under predominant conditions. The reaction A $\longrightarrow$ B might still never occur on a measurable level, because of extremely slow kinetics. Presence of catalysts or inhibitors can have a strong influence. The overall reaction rate is not solely dependent on reaction kinetics. Flow conditions, diffusion, heat and mass transfer also affect reaction rates. This fact poses the main reason why the reaction system in this work is investigated in a fluidized bed reactor.

For heterogeneous gas-solid reactions kinetics are described differently than in homogeneous systems. These types of reactions are not exclusive to TCES, but have been studied for a long time, for example, in solid fuel combustion. The predominant concept is given by differential equation 3.22.

$$\frac{\mathrm{d}\alpha}{\mathrm{d}t} = k(T)h(p)f(\alpha) \tag{3.22}$$

Reaction rate $\frac{\mathrm{d}\alpha}{\mathrm{d}t}$ is described by three independent functions. Temperature dependency $k(T)$, pressure dependency $h(p)$ and conversion dependency $f(\alpha)$. Conversion α is defined by the molar amount of reacted material $(n_{i,0} - n_i(t))$ to the initially available molar amount $n_{i,0}$. It is also possible to express conversion via the reaction coordinate ε (Eq. 3.23).

$$\alpha(t) = \frac{n_{i,0} - n_i(t)}{n_{i,0}} = \frac{\nu_i\,\varepsilon}{n_{i,0}} \tag{3.23}$$

---

[2] Data taken from the Hsc-database

Deutsch [11] gives a comprehensive overview on currently used functions and models. Following his work, some of the most important concepts are discussed.

Temperature dependency is in most cases described by the Arrhenius equation.

$$k(T) = A\, e^{\frac{-E_a}{RT}} \tag{3.24}$$

Experiments are often carried out isothermally or with constant heating/cooling rate (isokinetic $\frac{\mathrm{d}T}{\mathrm{d}t} = const.$). If differential rate laws are used, $k(T)$ can be directly inserted in Eq. 3.22. If integral rate laws are needed for an identification method, Eq. 3.22 has to be integrated. At isobaric-isothermal conditions, integration is readily achieved. If the temperature profile is time-dependent, the integral has no analytical solution (Eq. 3.25 – due to isobaric conditions the pressure dependency is included in the pre-exponential factor A'). Approximations for isokinetic measurements are available.

The Arrhenius equation predicts higher reaction rates at higher temperatures. For systems like the hydration of MgO, reaction rates appear lower at higher temperatures if partial pressure is kept constant. This is no contradiction, as will be explained once the pressure function is introduced. The Arrhenius equation reflects temperature influence very well and is thus used as a mathematical description.

$$g(\alpha) = \int_0^\alpha \frac{1}{f(\alpha')}\mathrm{d}\alpha' = \int_0^t A' e^{\frac{-E_a}{RT(\tau)}}\mathrm{d}\tau \tag{3.25}$$

To determine the conversion dependency $f(\alpha)$ various conversion models are available. Further distinction happens based on the shape of the $\frac{\mathrm{d}\alpha}{\mathrm{dt}}$ - α curve. Acceleratory models show increased conversion rates with increased α. The opposite effect, where $\frac{\mathrm{d}\alpha}{\mathrm{dt}}$ decreases with higher conversion, is referred to as deceleratory models. Sigmoidal models are bell-shaped, accelerating at low conversion, leveling-off and decelerating at higher conversions. Constant models show no relation of $\frac{\mathrm{d}\alpha}{\mathrm{dt}}$ and α.

Four main classes of mechanistic models are distinguished.

Nucleation models are often used to describe solid-state reactions. It is assumed that nucleation takes place at imperfections of the crystal lattice, so called nucleation sites, where the activation energy is lowered. Using the general chemical equation (Eq. 3.1) as example, the solid B is formed in the lattice of A while the latter is decomposing. The Avrami-Erofeyev models are commonly used nucleation models (Eq. 3.26) [28]. Dehydration of $Mg(OH)_2$ was found by McKelvy et al. [43] to be of this kind.

$$g(\alpha) = [-\ln(1-\alpha)]^{1/n} \tag{3.26}$$

Interface models or geometrical contraction models assume rapid development of nuclei on the whole surface area. Overall kinetics of a reaction are then determined by the surface area of the particle. Conversion is thus directly dependent on the (with time) changing characteristic particle radii. For a sphere this yields

$$\alpha(t) = 1 - \frac{r(t)^3}{r_0}. \tag{3.27}$$

Resulting in

$$f(\alpha) = 3(1-\alpha)^{2/3} \tag{3.28}$$

Order based models are commonly used in homogeneous reaction systems. The reaction rate is proportional to the concentrations of the reacting species to the power of n, which is the respective reaction order. n equals the sum of all involved molecules in an elementary reaction. Elementary steps are often not known in heterogeneous system. Without resembling the underlying model, order based models are nevertheless used for gas-solid reactions, because of their mathematical simplicity.

Diffusion controlled models: Product layer diffusion controlled models assume that a product layer forms around the educt, hampering the reaction. This mechanism only occurs in systems where one phase is immobile (e. g. gas-solid reactions). The reaction rate is controlled by diffusion and is proportional to the thickness of the product layer. The simplest model assumes one-dimensional diffusion between the particle surface and the product/educt interface. The thickness of the product layer is described by Fick's law of diffusion. Again, using the standard TCES reaction (Eq. 3.1), the gaseous component C diffuses through the built up product layer of substance A in order to react with the remaining solid B.
Not only diffusion through the product layer can be rate limiting. The inner surface area of particles is accessible by open pores. Diffusion through these pores can be rate limiting. Diffusion through the boundary layer between the particles surface and the surrounding gas phase is called bulk diffusion and can also be in control of the reaction rate.

For the pressure dependency there is no physical foundation and models are generally empirical. $h(p)$ is often incorporated in the Arrhenius equation, allowing an identification only by varying A and E_a at different pressure levels. A novel method for directly identifying $h(p)$ and $k(T)$ without relying on kinetic models and the Arrhenius law was proposed by Deutsch [11]. It is well established, that reaction rates for a system like the one investigated in this work (Eq. 3.5), depends on the difference between the actual partial pressure p_i and the equilibrium pressure $p_{i,eq}$ of the gaseous component (the 'driving force' of the reaction) [9, 49]. An empirical model for $h(p)$ is therefore given in Eq. 3.29, β being a model parameter [9].

$$h(p) = (p_{i,eq} - p_i)^{\beta} \tag{3.29}$$

If this parameterization is applied to describe pressure dependency, temperature dependency follows the Arrhenius equation again. I. e. at constant distance to equilibrium pressure, higher temperatures deliver higher reaction rates. At constant partial pressure, however, distance to the equilibrium curve is a function of temperature. Hence, the opposite effect to what the Arrhenius equation states, is observed, if partial pressure and not distance to equilibrium pressure is chosen as parameter. Temperature dependency of equilibrium pressure outweighs the temperature effect according to Arrhenius.

3.3 Fluidization technology

Because of the importance of fluidization technology to this work, a few relevant basics are discussed in this section. Hofbauer [26], for example, gives an excellent overview and Kunii [36] provides a more comprehensive insight.
Fluidized beds can be distinguished by their flow type. At low fluidization velocities particles are not moving. A fixed bed is the result. With increasing velocity the bed starts to expand and particles start to move. Minimum fluidization velocity is reached. From this point on

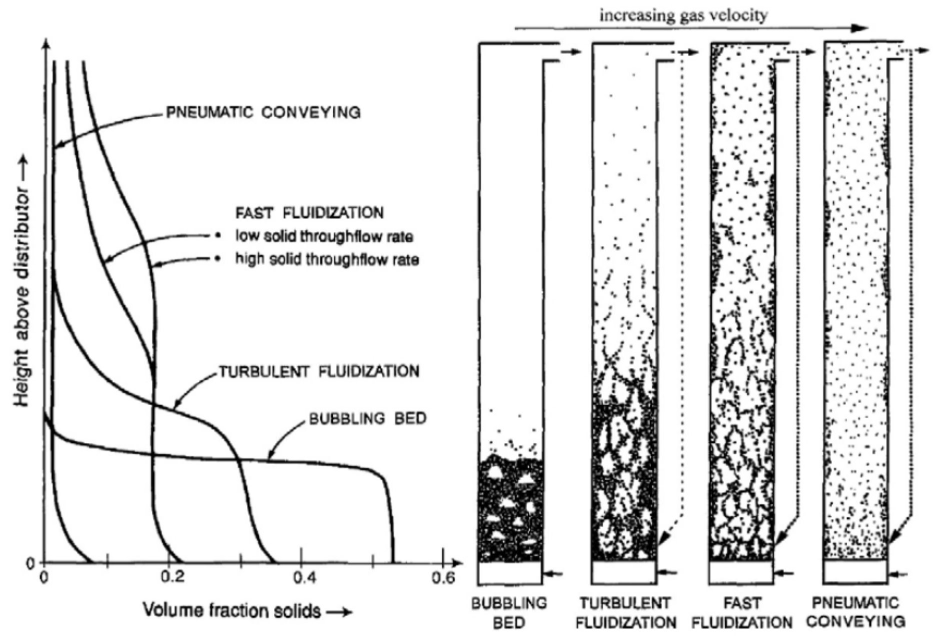

Figure 3.5: Flow regimes with particle distribution, from [36]

the term fluidized bed is used. Further increase in velocity leads to the formation of bubbles (bubbling fluidized bed).
Fluidized beds can be operated over a wide velocity range. Bubbling fluidized beds exist between minimal fluidization velocity and terminal velocity. At a certain point the flow type changes again. Bubbles are rejoining and particles appear in strands (turbulent fluidized bed). Depending on particle size, this can be the case already below, but also above terminal velocity. The term fast fluidization is used, once a considerable amount of bed material is carried out of the reactor and particles are distributed over the whole reactor height (Fig. 3.5). In order to maintain stationary operation solids have to be recycled. This is mainly achieved by using a cyclone. These flow types can often be used advantageously in applications. However, for a reactive fluidized bed, as it is presented here, bubbling FBRs are favored. They exhibit higher heat and mass transfer rates and leave more time for the reaction to occur. Operation should therefore be at low fluidization velocities. Also, turbulent or fast FBRs would require a much more complex testing plant as well as increased steam production rates in order to maintain partial steam pressure. If particles are dispersed widely and only a lean phase is present, even directly above the distributor, pneumatic transport of solids prevails.
In order to characterize behavior of materials in a FBR some basic quantities need to be introduced.
Most of the materials used, deviate geometrically from a perfect sphere. Hence, equivalent diameters are defined. Important for this work is the Sauter-diameter d_{SV} (sphere with the same surface to volume ratio as the particle).

$$d_{SV} = \frac{6 * V_p}{SAp} \tag{3.30}$$

The sphericity ϕ_s describes deviation of particles from a sphere. It is difficult to evaluate this parameter, but influence on fluidization behavior is substantially.

$$\phi_s = \left(\frac{\text{surface of sphere}}{\text{surface of particle}}\right)_{\text{of same volume}} \tag{3.31}$$

An accepted method to determine sphericity is to determine d_{SV} and d_V separately. In contrast there is the particle diameter d_p. It can be explained as the diameter of a particle that just barely fits through a sieve with a certain mesh size. There is no geometrically exact correlation between d_{SV} and d_p, but depending on the particle's shape, an approximation using sphericity is applied.

Porosity or bed voidage is a function of particle shape, particle size and size distribution. It can be calculated using Eq. 3.32.

$$\varepsilon_p = 1 - \frac{\rho_b}{\rho_p} \tag{3.32}$$

ρ_b denotes the bulk density, which can be easily measured. ρ_p is the particle density. Particles often have porosity themselves. For many applications including TCES, this is crucial. For determination of ρ_p however, the 'absolute' density of the material is not applicable, because the internal void fraction has to be respected. Measurement can be done with a gas pycnometer, in general.

Only specially prepared particles (e. g. glass beads) have a uniform size. Technically used particles show a more or less wide size distribution. The wider the distribution, the greater is deviation from ideal behavior and the more restricted application of formulae, describing real behavior sufficiently, is. One way of calculating a mean diameter is using the harmonic mean. This parameter weighs fine fractions more than coarse ones, reflecting the influence of small particles on fluidization better.

$$d_{SV} = \frac{1}{\sum\limits_i \frac{x_i}{d_{SVi}}} \tag{3.33}$$

This is not applicable for bimodal size distributions. Here, both fractions have to be treated independently.

Geldart distinguishes between four different kinds of particle behavior. These groups are depicted in Fig. 3.6. Group boundaries are defined by a certain particle size (x-axis) and particle density (y-axis – to be exact the density difference of particles and fluidizing gas). **Group C** are very fine powders (e. g. flour). They show cohesive behavior, because interparticle forces are dominant to forces imposed by fluidization. Materials in this group are difficult to fluidize. Channeling occurs in the bed. Fluidization is often only possible by introducing coarser particles or apply vibration energy. **Group A** (aeratable) exhibit smooth fluidization behavior. The bed expands before bubbling starts. Materials are easy to fluidize. Bubbles coalesce and split frequently and do not exceed a certain size (e. g. FCC catalyst). Sand-like **Group B** particles also fluidize well. Bubbling usually starts immediately and they coalesce and grow with higher velocities, resulting in more violent spouting. **Group D** represents large particles, which can be difficult to fluidize. Exploding bubbles, channeling or spouting is characteristic for this group (e. g. coffee beans, grains). From this overview it becomes clear that Group A and B are desirable.

As already mentioned, an important quantity to determine the point where fluidization starts is minimal fluidization velocity u_{mf}. It can be determined experimentally by measuring pressure loss through the bed and plotting it versus superficial velocity. Fig. 5.3 shows a typical curve.

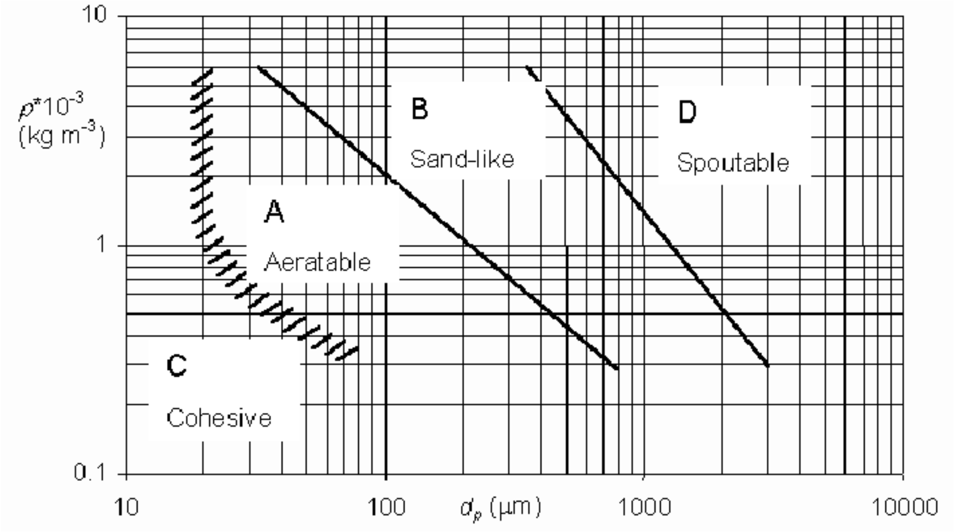

Figure 3.6: Geldart classification of particles, from [36]

As long as the bed is fixed, pressure drop increases linearly. In a fluidized bed pressure drop is constant. Pressure difference equals the weight of bed material. Theoretically, when using monodisperse material, u_{mf} is defined unambiguously by the intersection of the two lines. Especially when using materials with a wide size distribution, the curve might look like Fig.5.3 and u_{mf} is determined by extending the lines as shown.

Mathematically u_{mf} can be found by combining equations for pressure loss in a fixed bed and in a fluidized bed. An equation quadratic in u_{mf} is the result. Simplified equations exist which give rough estimates. Especially if the void fraction at minimum fluidization $\varepsilon_{p,mf}$ and the sphericity is not known these equations may be used (Eq. 3.34).

$$u_{mf} = \frac{\mu_g}{\rho_g * d_{SV}} \left(\sqrt{33.7^2 + 0.0408 * Ar} - 33.7 \right) \qquad 0.001 < Re < 4000 \tag{3.34}$$

Where Ar is the Archimedes number

$$Ar = \frac{d_{SV}^3 \rho_g (\rho_p - \rho_g) g}{\mu_g^2}. \tag{3.35}$$

In order to determine the point where particles are carried out of the FBR, terminal velocity is calculated. It is derived from fluid dynamics as the terminal free-fall velocity for a single particle. To describe non-spherical particles the sphericity is used again[3]. One possible approximation is given by Eq. 3.36.

$$u_t^* = \left(\frac{18}{(d_p^*)^2} + \frac{2.335 - 1.744\phi_s}{(d_p^*)^{0.5}} \right)^{-1} \tag{3.36}$$

With $d_p^* = Ar^{\frac{1}{3}}$ and

$$u_t^* = u_t \left(\frac{\rho_g^2}{\mu_g (\rho_p - \rho_g) g} \right)^{\frac{1}{3}} \tag{3.37}$$

---

[3] It is used as approximation, but does not describe real fluid dynamic phenomena.

Distributor plates used in industrial processes include perforated plates, perforated pipes (spargers) and tuyeres with nozzles or bubble caps. The latter uses pipes or a wind box to supply gas. If pipes are used, the distributor is open and material or ash (in combustion) can be removed from below. Tuyeres are more expensive, but mechanically more stable and can be used in high temperature applications or with highly reactive environments. For lab-scale plants ceramic or sintered metal porous plates as well as perforated plates are used. Porous plates are readily used because they give uniform gas distribution due to their high pressure drop. Also, they are much simpler than tuyeres, for example. For industrial applications there are drawbacks. High pressure drops results in increased pumping power, mechanical and thermal stability are poor and clogging by fine particles might occur. To achieve uniform distribution on the one hand and limited pumping power on the other hand a rule of thumb is followed. Pressure drop through the distributor should be at 20 % to 40 % of bed pressure drop. For lab-scale plants economical optimization is of no concern and pressure drops in the reactor used here, are actually much higher.
As already mentioned, distinct advantages of FBRs are increased heat and mass transfer rates due to the constant material circulation. This is described by dispersion models. Isothermal conditions are the result and low heat conductivity is compensated. This is especially favorable here, because magnesium oxide/hydroxide is characterized by low heat conductivity coefficients. Also, heat transfer between fluidized bed and heat exchanger, which is immersed in the bed, is increased by an order of magnitude. Heat transfer coefficients of $200\,\frac{\mathrm{W}}{\mathrm{m^2\,K}}$ to $400\,\frac{\mathrm{W}}{\mathrm{m^2\,K}}$ are usual. Particle sizes and fluidization velocities have an influence. Highest coefficients are reached just above minimum fluidization. Particle size is optimal around 20 µm to 50 µm, sharply dropping for smaller Geldart C particles.

Gas flows through a fluidized bed in bubbles and in the emulsion phase, with gas exchange constantly taking place in between. Fluidization velocity and bubble size influence gas interchange and therefore conversion. The presented reaction is used as an example. Increasing fluidization velocity (at constant water loading) results in more steam provided to the reactor per unit of time which leads to enhanced particle-to-gas mass transfer and higher concentration of steam within the bed. However, also residence time of the reactant gas is reduced, leading to lower gas conversion. Low gas conversion is detrimental to power consumption, because most of the (energy intensely) produced steam passes the reactor unchanged. In addition, a higher mass flow rate itself significantly increases power consumption. For TCES, fluidization velocities close to minimal velocity is thus preferred.

Small bubbles are advantageous, because gas interchange between bubble and emulsion phase is again increased. Bubble size meanwhile is again dependent on fluidization velocity and bed height. Larger bubbles are observed at higher velocities. They also grow and coalesce as the rise through the bed. Higher beds therefore reduce the bubble - emulsion interchange surface area. Residence time is however increased in larger bed heights. Many influencing factors have now been mentioned. As will be seen in the experimental section, a big effort has been made to keep these parameters constant or influence is neglected if not avoidable.

3.4 TCES in a fluidized bed reactor

Using a fluidized bed reactor is one way to utilize TCES. So far, most authors investigating TCES proposed fixed bed reactors [52]. FBRs, however, are characterized by improved heat and mass transfer rates, as well as a homogeneous temperature distribution across the entire bed (isothermal conditions). This can allow faster kinetics and operation closer to the equilibrium curve. Also, high heat transfer coefficients allow high energy transfer rates to heat exchangers. On the other hand, FBRs require more energy for fluidizing the bed material, resulting in higher blower power. Additionally, partial pressures are mostly limited to ambient pressure, since pressurized FBRs are not common. Advantages however often outweigh drawbacks. For the reaction to occur, a certain partial pressure level has to be maintained. Both, the integrated reactor concept as well as multiple reactors can be utilized. Using a bubbling fluidized bed reactor is preferred over turbulent or fast FBRs for reactive beds.

An process utilizing multiple FBRs in a cascade was proposed by Flegkas et al. [18] (Fig. 3.7). Only the storage process is depicted. For high efficiency, multiple reactions at different temperature levels are necessary. Because of isothermal conditions, a FBR is unable to cool the heat source below reaction temperature (turning temperature). If only a material pair with a high turning temperature is used, residual heat cannot be utilized. A TCES system with a low turning temperature would result in intolerable exergy losses, because heat is downgraded to a lower temperature level. Hence, they propose a three stage process utilizing the $CaO/Ca(OH)_2$ system, cooling waste heat from 576 °C to 460 °C. At intermediate temperatures $MgO/Mg(OH)_2$ is used to cool from 460 °C to 272 °C (in this work it will be shown that, at a temperature of 272 °C, kinetics are too slow to be technically interesting). For low temperature levels a sorption process based on calcium oxalate (CaC_2O_4 /$CaC_2O_4 \cdot H_2O$) is proposed.

In order to utilize the process most efficiently, a few heat exchange steps are implemented downstream. In the first stage, water loaded air, as a result of the dehydration reaction, is cooled twice before entering an additional reactor which utilizes a portion of the produced calcium oxalate. Besides providing additional heat, the intention is to reduced water content of the air. This reduces parasitic energy needed for water condensation. After condensation dry air is preheated in the fluidization air recuperator and enters the reactor again. The fluidized bed recuperators are designed to utilize sensible heat in the CaO product stream, which would be lost otherwise. Also, $Ca(OH)_2$ entering the system, coming from the external hydration reaction, is heated up before entering the reactor. This increases reactor performance.

Stages two and three are in principle designed the same way. Only for calcium oxalate no heat recovery of sensible heat of solids is intended. Utilizing recuperators increases the system's complexity and economical considerations will determine the number of subsequent steps implemented. Making use of fluidized bed recuperators increases theoretical heat available for the hydration process by 35 %.

For hydration a similar cascade process is thinkable. Alternatively, transportation of materials to different sites, customized to required temperature levels is also possible. This is, of course, only one example. If only time discrepancies of heat supply/demand must be bridged, the integrated reactor concept, where both reactions take place in one reactor, is an interesting alternative.

Chemical heat pumps (CHP) are another way of utilizing TCES. Here, heat can be upgraded to a higher temperature level having the same result as a 'normal' heat pump (see [58] for further information). Kato et al. [34] proposed a CHP based on the $MgO/Mg(OH)_2$ system.

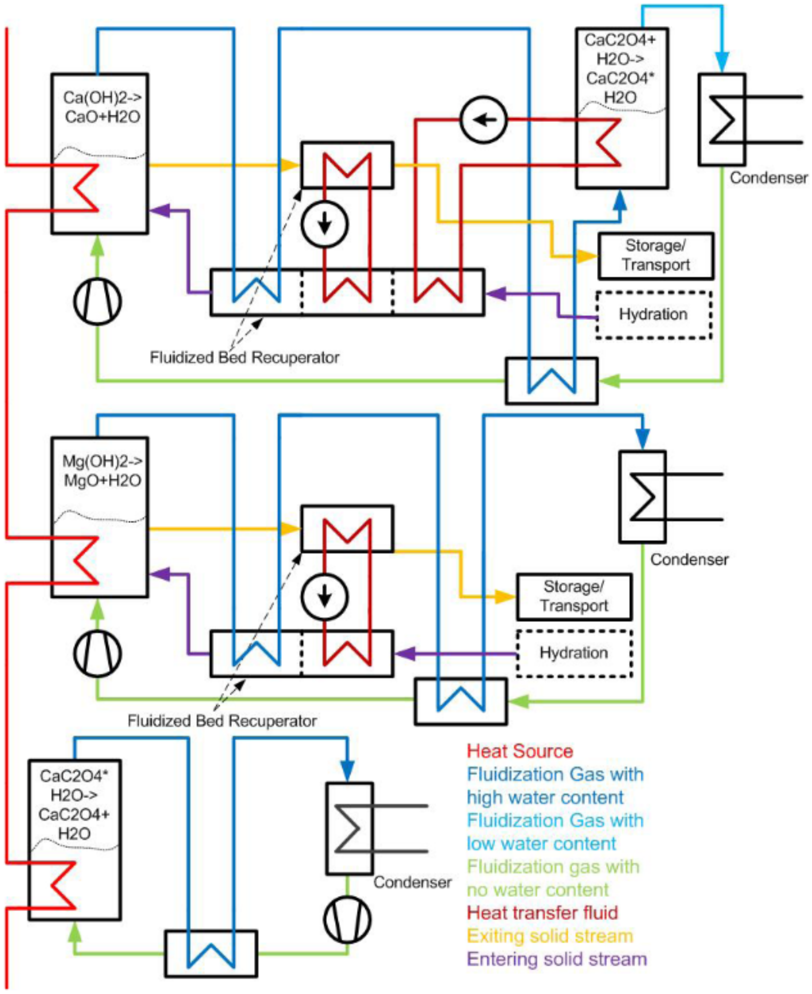

Figure 3.7: Three stage cascade process, from [20]

4 Experimental setup

Design and construction work for this experimental plant is carried out by AMMAG[1]. Installation of measurement and control technology is carried out by TU Wien. The design has been the topic of another thesis. In this section the most important facts for experimentation are summarized. The experimental plant used in this work, is explicitly designed for testing of materials and not optimized for industrial application. **It is designed for a maximum reaction temperature of 400 °C.**

4.1 P&ID

Fig. 4.1 shows the Piping and Instrumentation Diagram (P&ID) of the testing plant. Two different experimental setups were used. In the first setup, steam generator S-1 is used as depicted in the diagram. Also, the electrical heating of reactor R-1 is not installed. The second setup uses steam generator S-2 and the additional reactor heating. Availability of the steam generator and excessive heat losses made the change necessary. In order to successfully operate steam generator S-2 a few adaptions according to Fig. 4.2 are necessary (explanation see section 4.2). Also, the oxygen sensor (I-09) is only used with the first setup. Numbering assigned in the figures is used in the following sections.

A description of the basic principle of the experimental plant follows. Air is sucked in through filter (F-1) and compressed by compressor C-1. Air heater H-1 heats the air to a certain temperature, before it is being mixed with steam coming from steam generator S-1 or S-2. Moist air, with a defined steam partial pressure enters the tempered (with H-2) FBR (R-1) from the bottom, flowing through the distributor plate. Air works as fluidizing medium and as carrier for the reactant. Material is placed in the reactor through funnel Fu-1. After dust separation in filter F-2 humid air leaves the plant as exhaust gas.

4.2 Components

To better understand the operation capacities and the functionality of the plant a short description of its components is given in this section. Table 4.1 gives an overview over components and their most important operational data.

---

[1] https://www.ammag.at/

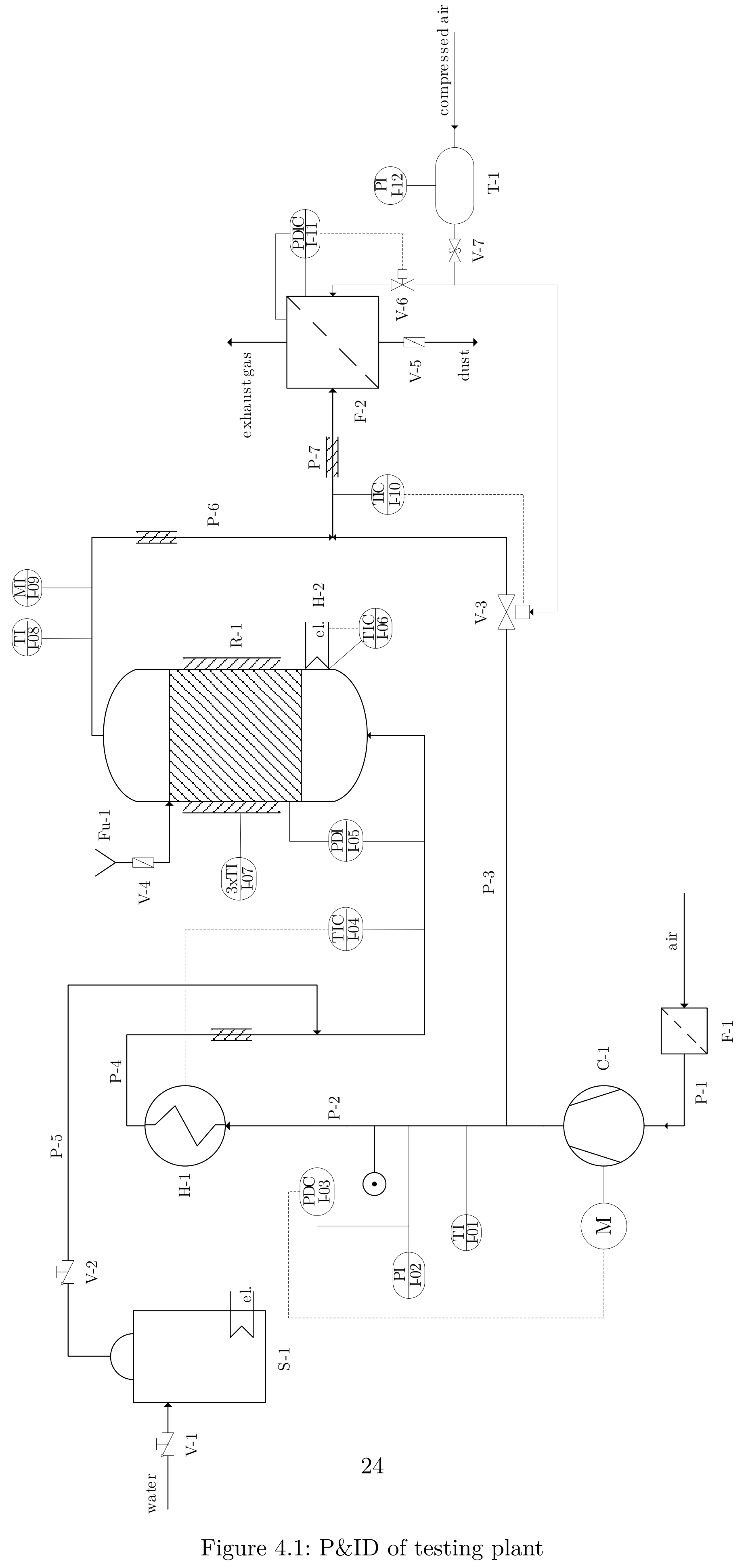

Figure 4.1: P&ID of testing plant

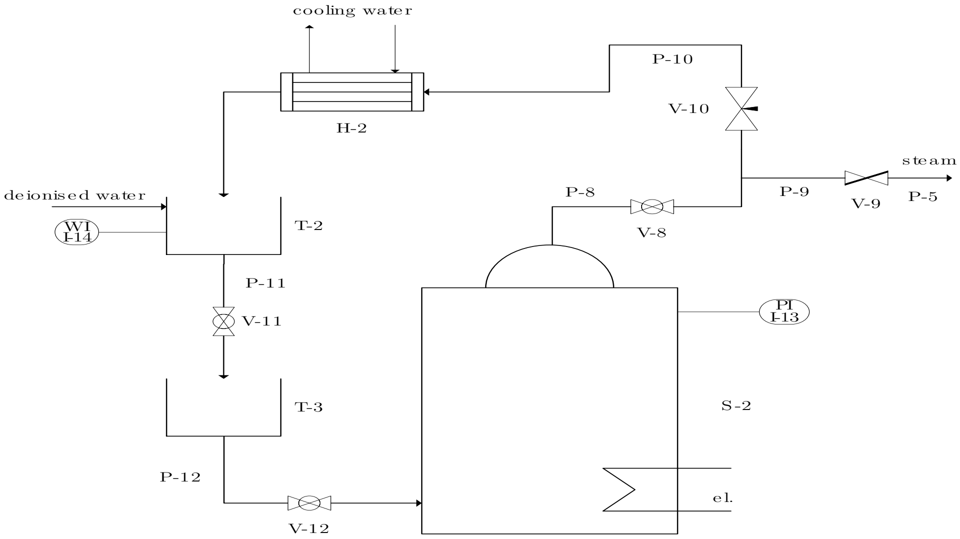

Figure 4.2: P&ID of Ghidini steam generator (S-2)

Figure 4.3: Experimental plant, front view

Figure 4.4: Experimental plant, back view

Table 4.1: Component specification

P&ID-Number	Name	Manufacturer and type	Data
C-1	compressor	Elektror SD 6	max. pressure difference: 300 mbar max. volume flow rate: 4.6 $\frac{m^3}{min}$ rated output: 2.2 kW RPM: 2870 $\frac{1}{min}$ Voltage: 400 V
H-1	air heater	Leister LHS 61S	max. outlet temperature: 650 °C max. inlet temperature: 65 °C rated output: 8.5 kW min. air flow rate (at rated output): 800 $\frac{L}{min}$ Voltage: 400 V
H-2	reactor heater	Isoheat MiL-HT-G	max. surface temperature: 450 °C length: 7 m rated output: 1.4 kW not protected against moisture Voltage: 230 V

Table 4.1: (continued)

P&ID-Number	Name	Manufacturer and type	Data
I-09	O_2 sensor	J.Dittrich Electronic MF420-O	measurement range: 0.1 - 25 Vol% oxygen accuracy: ±1 % of ultimate value reproducibility: < ±1 % max. temperature: 450 °C max. gas velocity: 10 $\frac{m}{s}$
I-09	humidity sensor	Testo humidity transmitter (6681) and cable probe (6613)	measurement range: 0 $\%rF$ to 100 $\%rF$ temperature range: −40 °C to 180 °C reproducibility: < ±0.2 $\%rF$ accuracy: $\pm(1.0\%rF + 0.007 * \langle value \rangle)$ and 0.02 $\%rF$/K max. response time: 15 s
S-1	steam generator	Condair RS 5	max. steam mass flow: 5 $\frac{kg}{h}$ rated output: 3.8 kW control accuracy: ±5 % rF max. excess pressure in channel: 1500 Pa Voltage: 400 V
S-2	steam generator	Ghidini Maxi 16	rated output: 6(12) kW max. pressure in vessel: 4 bar voltage: 400 V
I-02 I-03 I-05 I-11	pressure transmitter	Kalinsky Sensor Elektronik DS2-420	power supply: 24 V output signal: 4 mA to 20 mA pressure range: I-02: 0 - 250 mbar I-03: 0 - 10 mbar I-05: 0 - 25 mbar I-11: 0 - 10 mbar

Table 4.1: (continued)

P&ID-Number	Name	Manufacturer and type	Data
I-04 I-06 I-07 I-08	sheath resistance thermometers	Sensorshop 24 Pt100 1/3DIN	max. temperature: 600 °C diameter: 3 mm material: stainless steel 1.4541 cable: glass fiber max. cable temperature: 400 °C accuracy: not standardized[a]
I-01 I-10	sheath thermocouple	Sensorshop 24 Typ J	max. temperature: 850 °C diameter: 3 mm material: stainless steel 1.4541 cable: glass fiber max. cable temperature: 400 °C accuracy: DIN 43710-class 1[b]
V-10	needle valve	Burde Fig. 110-1"	material: stainless steel DN/PN: 12/200
I-14	parcel scale	EOB 15K5-2017	weighing range: 15 kg reproducibility: 5 g readout: 5 g

[a] ±0.1 °C at 0 °C [48] is usually abided by manufacturers

[b] Standard is not valid anymore; new standard (DIN 60584-1 [15]) specifies: ±0.5 °C or $0.004 * t$

Compressor

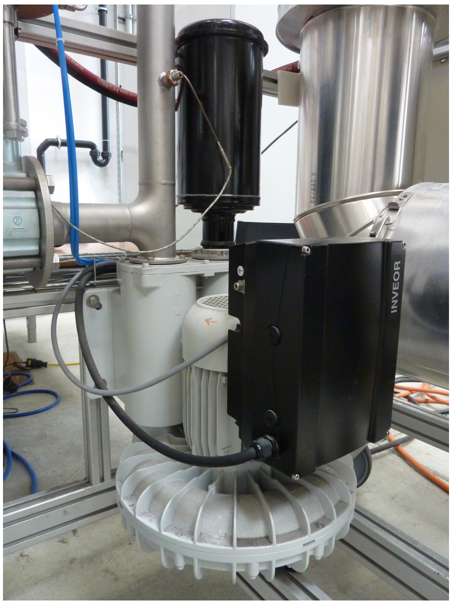

Figure 4.5: Elektror Compressor with frequency converter and filter

The compressor consists of a package containing the compressor itself, the motor, a filter for the suction inlet (F-1) and the INVEOR frequency converter to enable motor control.

Air Heater

Figure 4.6: Leister air heater [38]

Operation with dry air only. Humidity causes the air heater to malfunction. The ceramic body inside can shatter due to humidity or excessive mechanical stress. In order to stay below the maximum allowed temperature, the heater power is limited and controlled with respect to the air flow rate. A sudden shutdown of the compressor should be avoided when the heater is in operation. Due to the heat build-up overheating might occur, even if the heater is turned off. It is recommended to maintain air flow for several hours after experiments using steam, in order to prevent any humidity entering the air heater.

Humidity measurement

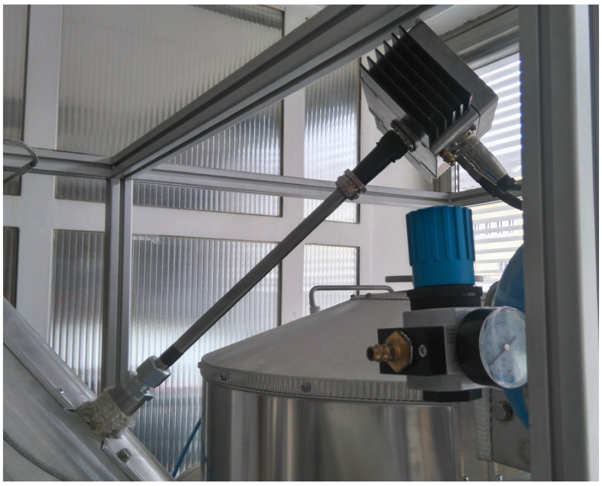

Figure 4.7: Oxygen sensor

The oxygen sensor measures the O_2 content (in Vol%) of the exhaust gas directly. This value is in relation to the water content. It consists of rod sensor and transmitter and is designed especially for use in high temperature environments. The sensor itself sits at the top of the rod and is protected by a cover tube. Its operating principle is based on the Nernst cell (a solid-state electrochemical fuel cell producing an ouput voltage proportional to the O_2 concentration difference of exhaust gas and reference air; also called lambda sensor). As membrane, zirconium dioxide is used. Fig. 4.7 shows the sensor installed on the plant. During experimentation, the probe was found to be unsuitable for this application. In order for the principle to work, the membranes have to be permeable. This, however, also enables dust to pass the barrier and enter the sensor. Especially the first batch of material used for testing – as will be seen in section 5.1.3 – shows a high dust load, destroying the probe in the process.

Since the oxygen sensor is unfit for use in this case, Testo humidity sensor is tested. It consists of two electrodes and a polymer dielectric working as capacitor. Change in capacity due to changing humidity is measured. The transmitter is able to directly indicate partial pressure. Since the probe is unheated (contrary to the oxygen probe), condensation poses a problem and the transmitter reports an alarm accordingly. Because of the operating principle, the same issue as with the oxygen probe arises. One electrode has to be permeable to water vapor. This again allows dust to alter results. Also, because of its limited accuracy exact measurements cannot be performed.

Thus, for the second setup no measurement of water content was possible.

Steam generator

The Condair steam generator (S-1) is electrically powered. Water is heated up internally using resistance heating elements. Tap water is continuously supplied via a water hose. The steam generator is connected with a steam hose to the plant (P-5). It can be controlled remotely or via the integrated control. For the purpose of this work, the mass flow rate of steam is controlled remotely (continuously variable adjustment possible). The operating range is however limited. 5 $\frac{\mathrm{kg}}{\mathrm{h}}$ does not suffice for the full planned experimental scope. Some

restrictions have to be imposed in the first stage of experimentation. The lower limit is found to be at 2.5 $\frac{\text{kg}}{\text{h}}$. Below this limit steam is given off at intervals, pausing in between (pulsing). This behavior is not feasible. For experiments, continuous steam production would be optimal. Due to the integrated automatic level control system, water is only refilled when the level sinks below a certain point (at intervals). If this occurs, the newly drawn water needs to be heated up to saturation temperature first, before evaporation takes place. At constant heater power, this results in diminished steam production.
As listed in Table 4.1 the excess counterpressure (the excess pressure in the pipe at the point where the steam hose is connected to the plant) is limited. If it is exceeded, steam production breaks down and water is pressed out reversely through the emptying pipe of the steam generator. In order to validate the set steam production rate, measurements are taken. Steam is simply condensed directly into a water bucket over a certain period of time, measuring the weight difference. Fig. 4.9 shows determined values and standard deviation calculated by taking multiple measurements. Set value indicates the value used for calculating partial pressure.

In principle, the steam generator from Ghidini (S-2) works the same way. There are a few differences, however. In contrast, it has increased power. Thus, higher flexibility in terms of experimental parameters is achieved. It can be operated from ambient pressure up to 4 bar. Hence, the problem with pressure limitation is solved. The drawback is, however, that this model cannot be controlled in any way. It is only possible to switch between 6 kW and 12 kW of heater power. To implement the steam generator in the plant, adaption is necessary. The solution is presented in the P&I diagram (Fig. 4.2). A picture of the actual construction is given in Fig. 4.8.
To increase working life of the steam generator, it is operated with deionized water. Steam exiting the generator is divided in copper pipes into two separate streams. One, continuing to the plant via valve V-9 and steam hose P-5, the other part being condensed and reused. The ratio of the two streams can be adjusted by turning needle valve V-10 to a certain position. It works as a throttle, adjusting pressure differences and therefore mass flow between the two pipes. Condensation takes place in heat exchanger H-2 (blue barrel). The blue barrel is filled with cooling water via the upper hose (yellow garden hose at the back of the barrel). The return hose is placed at the lower part of the barrel, enabling continuous cooling water throughput (flow rate of cooling water is adjusted via a valve connected to the return hose–maximum flow rate is determined by the hydrostatic pressure). Steam is condensed in the copper pipe, which is running through the barrel in a spiral. A short calculation shows, that about 4 m of water cooling line is needed – air cooling does not suffice. Hence the chosen design. Condensed water is then gathered in tank T-2. By opening ball valve V-11 it flows back into storage tank T-3. Note, that T-3 needs to be placed at a minimum height of 20 cm above water inlet of the steam generator. The internal pump needs pre-pressure in order to work.
To determine the correlation between position of the needle valve and mass flow into the reactor, balance I-14 is installed. Weighing the condensed amount of water over a certain period of time gives the required information. It is found, that continuous measurement with the scale is not possible. Two measurements (before and after a certain time period) have to be done, taring the scale at every measurement. Mass flow rates of water are apparently too small and the scale shows wrong values when measuring continuously. Initially, the maximum steam production rate has to be determined by closing valve V-9, thus condensing steam entirely. Note, that the determined value is only valid for a particular fluidization velocity. Changing

Figure 4.8: Ghidini steam generator (S-2) with construction for adjusting steam mass flow rate

fluidization, changes the pressure at the steam inlet and therefore steam distribution. Also, the integrated pressure gauge (I-13) must not show any deviation from ambient pressure (also changing steam production rate). Results are displayed in Fig. 4.9. The theoretical value of $1.27\,\frac{\mathrm{kg}}{\mathrm{h\,kW}}$ (assuming $\Delta T = 80\,\mathrm{K}$) is not far off from the measured value of $1.33\,\frac{\mathrm{kg}}{\mathrm{h\,kW}}$. Accuracy is deemed sufficient for experimentation.

Flow measurement

The measurement principle chosen to determine mass flow rate of air is the orifice plate. Design is shown in Fig. 4.10. The orifice plate works as throttle device and is simply a disk with a central bore mounted in between two flanges. Pressure difference between two exactly predefined positions (before and after the orifice plate) is measured (I-02, I-03). Together with physical properties at operating conditions and geometrical data, the flow rate can be determined. Operating conditions are given by measuring temperature (I-01) and absolute pressure (I-02). Requirements and necessary calculations are described in standards DIN EN ISO 5167-1 [13] and 5167-2 [14]: Measurement of fluid flow by means of pressure differential devices inserted in circular cross-section conduits running full.

Because of limited pressure ranges of the pressure transmitters, orifice plates with varying borehole diameters have to be used in order to accommodate for the wide range of superficial velocities required for experimentation. To validate calculated flow rates, pressure difference across the distributor plate is plotted versus superficial velocity in the reactor (Fig. 4.11). Ideally, all the curves should align perfectly. This is (with high accuracy) true for the three

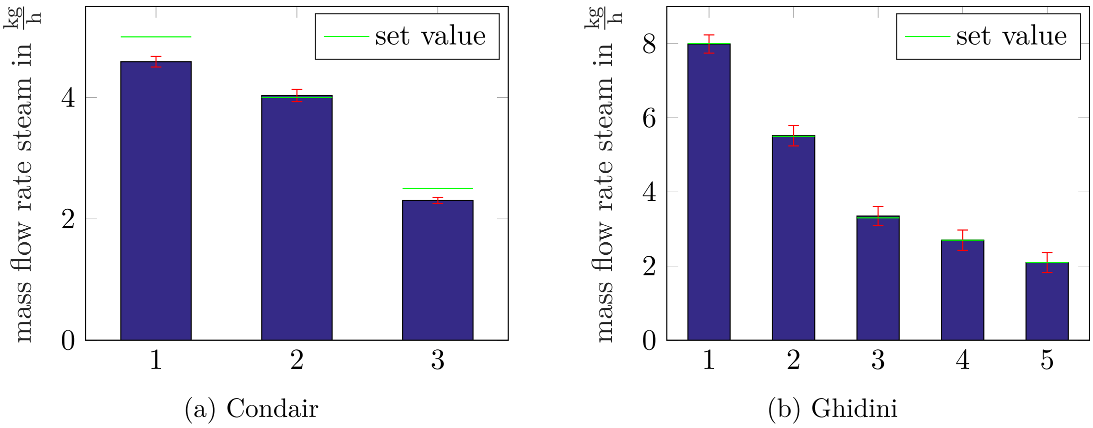

(a) Condair (b) Ghidini

Figure 4.9: Steam generator: determination of mass flow rate at different set points

Figure 4.10: Flow measurement with orifice plate

smallest diameters. The 20 mm bore already shows deviation. For experimentation mostly 12.5 mm, 15 mm and 17 mm orifice plates are used. The 20 mm plate is acceptable as well. Orifice plates with diameters greater than 20 mm (there are plates with 25 mm, 30 mm, 35 mm, 40 mm available) exhibit unacceptable deviations and cannot be used for experimentation. It is assumed that values acquired with the three smallest plates are true values. The reason for the wide margin is not found. Design of flow measurement was carried out according to standard.

The graph also gives information on distributor plate characteristics. Discussion follows below.

Reactor

The reactor is the central part of the plant. Here, the reaction takes places. It is designed as a bubbling fluidized bed. Two different types are in use. For cold flow experiments the glass reactor is used (Fig. 4.12b), because fluidization behavior of material can be monitored

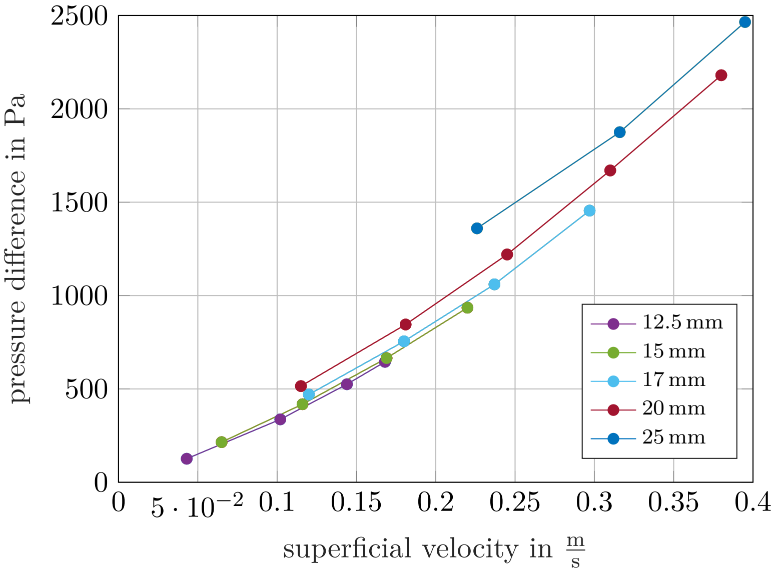

Figure 4.11: Validation of flow measurement

easily. The metal reactor is used for hot experiments. Fig. 4.12a shows it in mounted condition, already equipped with reactor heating H-2. It is swivel-mounted in order to facilitate emptying. Additionally, removable insulation can be mounted. Both reactors are mounted with flanges and are therefore interchangeable. Sealing is achieved with flat gaskets of graphite. As distributor plate an interchangeable sinter metal plate is used. With the glass reactor sealing between the plate and the reactor is achieved by using Teflon tape. For high temperature usage of the metal reactor, a carbon fiber sealing is installed. Since possible leakage (side flow at reactor wall) cannot be determined visually, pressure losses across the plate are compared between the two reactor types. Values are in the same order of magnitude, thus tightness is assumed. The distributor plate causes a pressure drop much higher than used in industrial application (see section 3.3). This should result in uniform gas distribution. The freeboard is design sufficiently high, for particles not to be carried out of the reactor. Note, that inner diameters of the two reactors are different (metal: 15.1 cm, glass: 16.04 cm). This has to be respected when calculating fluidization velocity.

Temperature measurement is done by four resistance thermometers, two of them in the interchangeable part of the reactor (2x I-07), as the photo shows. A third one is just below the distributor plate (I-04), the fourth one just above the interchangeable part of the reactor (I-07). On the right side of the reactor three threaded bores are provided. They are unused, because thermometers, for example, would have to be removed every time insulation is mounted/removed.

Pressure loss across distributor plate is measured directly with I-05. Pressure loss characteristics of the sinter metal plate are depicted in Fig. 4.11. It is found, however, that pressure loss is not constant over time due to plugging with fluidized material.

In the first stage of experimentation (first setup), it is found that heat losses are too dominant and the required temperatures for dehydration cannot be reached. Note, that air heater and compressor would allow much higher heat capacity flow rates, reducing heat losses proportionately. Because of experiment design, fluidization number is kept within a certain limit,

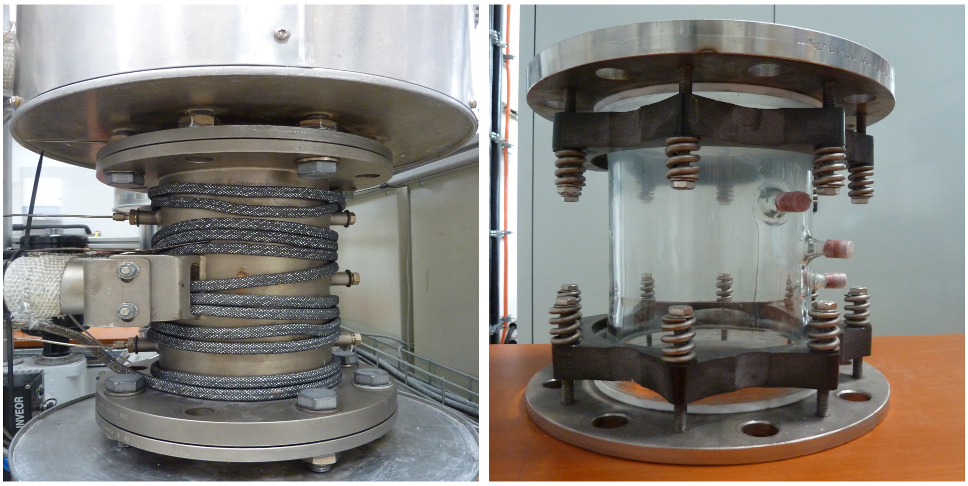

(a)

(b)

Figure 4.12: Reactor types: (a) metal reactor, (b) glass reactor

prohibiting higher flow rates. Therefore reactor heater H-2 is installed, a fiberglass-insulated heating tape. To control temperature, a Pt-100 element (I-06) is placed on the outer reactor wall. By controlling the temperature of the wall, so that it is equal to the inlet temperature, the reactor can be modeled as adiabatic.

Other components

Components that have not been mentioned so far include valves (denoted by V-x) and piping (P-x). Piping is made out of stainless steel and is insulated starting after air heater H-1 in direction of flow. Note, that P-5 is not a pipe, but a steam hose connecting the steam generator to the plant. V-4 is a butterfly valve used to release material stored in the funnel into the reactor. Valve V-5 is of the same sort, used to clear out dust gathered in the filter. V-3 is a pneumatic actuated valve controlling mass flow rate of air through the bypass into the filer F-2. V-6 is an electrical actuated valve, used for cleaning the filter by releasing a short pressurized air blast. I-12 and I-13 are pressure gauges integrated in the pressurized air tank and the steam generator, respectively.

4.3 Measurement data acquisition & control

For programming the control system and implementing data acquisition Automation Studio (V 4.2.6) by B&R is used. The program includes control for compressor, air heater, reactor heater and bypass. Measured variables are transformed and saved into a csv-file. All calculations, which are necessary to compile the required output, are performed within the program. Its content is not presented here. For further information read script documentation or contact the programmer Felix Birkelbach [2].
Here, only the user interface (UI) is discussed. It consists of several pages. In Fig. 4.13 the control room is depicted. Blower, bypass, heater and reactor heater have a drop-down menu

---

[2] Dipl.-Ing. Felix Birkelbach, TU Wien, Institute of Energy Systems and Thermodynamics (E302)

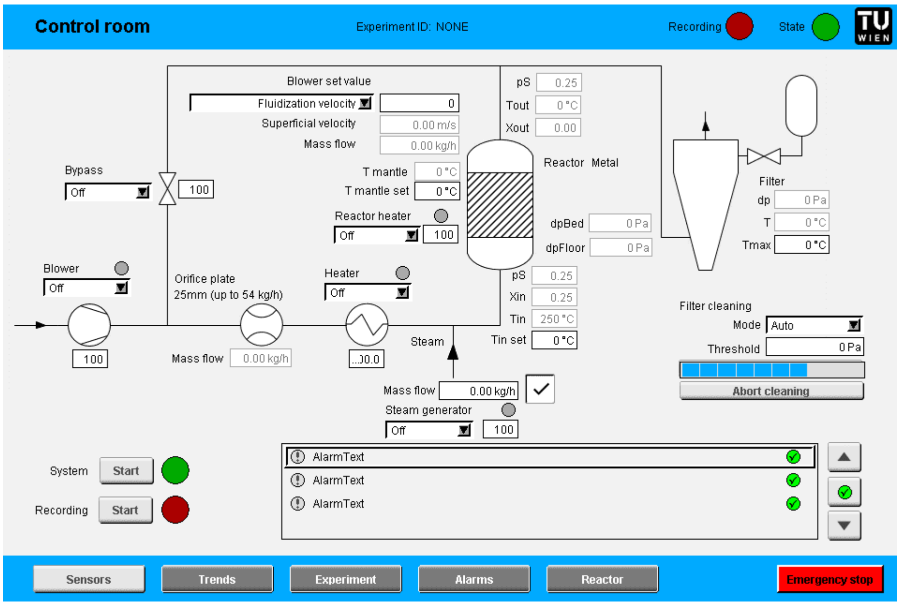

Control room

Experiment ID: NONE

Recording ●

State ●

Blower set value: Fluidization velocity 0

Superficial velocity 0.00 m/s

Mass flow 0.00 kg/h

Bypass: Off 100

T mantle 0 °C

T mantle set 0 °C

Reactor heater: Off 100

Blower: Off 100

Orifice plate 25mm (up to 54 kg/h)

Mass flow 0.00 kg/h

Heater: Off ...)0.0

Steam

Mass flow 0.00 kg/h ✓

Steam generator: Off 100

pS 0.25

Tout 0 °C

Xout 0.00

Reactor Metal

dpBed 0 Pa

dpFloor 0 Pa

pS 0.25

Xin 0.25

Tin 250 °C

Tin set 0 °C

Filter

dp 0 Pa

T 0 °C

Tmax 0 °C

Filter cleaning

Mode Auto

Threshold 0 Pa

System Start ●

Recording Start ●

AlarmText ✓

AlarmText ✓

AlarmText ✓

Figure 4.13: UI: Control room

containing operating modes. ‘Manual’ takes a percentage value as input, thus operating at constant power. ‘Auto’ enables control and ‘hold’ allows fixation at a constant value (e. g. the value determined by control once the system is in steady state). Control parameter for the blower is chosen at the drop-down menu ‘Blower set value’. It can be advantageous to control either fluidization velocity, volume flow rate or mass flow rate. Control parameter for the air heater is reactor inlet temperature I-04 (T_{in}), for the reactor heater, temperature I-06 (T_{mantle}). Bypass is necessary for filter (F-2) temperature to be controlled. Maximum allowed temperature (T_{max}) is set to be 150 °C. Also, the filter has an integrated cleaning system. Pressurized air is stored in vessel T-1 and released into the filter if button ‘clean now’ is pressed. In auto mode, filter cleaning starts automatically once a set threshold value is exceeded. Mass flow rate of steam is set manually. Together with the air mass flow rate, water content (X_{in}) and partial pressure (p_{in}) at reactor inlet is calculated. Note, that this value is of theoretical nature and is not being measured. This makes the importance of determining steam mass flow rate as shown in section 3.1.3 evident [3].
At reactor outlet, water content (X_{out}) and partial pressure (p_{out}) are calculated by measuring oxygen content with the O_2-probe (I-09, first setup only) together with temperature I-08 (T_{out}). Additional calculation values, which are displayed, are pressure difference in the bed (*dpBed*) and heat produced by the reaction (*Qdot*). The former is calculated by taking the difference of measured pressure loss minus predetermined pressure loss over the distributor plate. *Qdot* is calculated by taking temperature difference $T_{out} - T_{in}$. Because of the importance of partial pressure as a parameter for experiments, its calculation is shown here.
First, the mole flow rate of steam, taking ambient humidity into account, is calculated (index

---

[3] Value can be measured using the O_2 sensor if reactor is empty. This, however, only applies for the first setup, where the sensor is still available.

Table 4.2: Control parameters

	Blower	Air heater	Reactor heater	Bypass
Gain	1500	1	3	1
Integration time	3	60	20	15
Differentiation time	-	-	74	-
Filter time	-	-	30	-

s. . . steam, a. . . dry air).

$$\dot{n}_s = \frac{\dot{m}_s}{M_{\mathrm{H_2O}}} + \left(0.622 * \frac{p^s_{\mathrm{H_2O}}(T_{amb})}{\frac{p_{amb}}{\varphi} - p^s_{\mathrm{H_2O}}(T_{amb})}\right) * \frac{\dot{m}_a}{M_{\mathrm{H_2O}}} \tag{4.1}$$

The mole fraction of steam is then

$$x_s = \frac{\dot{n}_s}{\dot{n}_s + \dot{n}_a} \tag{4.2}$$

and finally the partial pressure at reactor inlet is

$$p_{in} = p * x_s. \tag{4.3}$$

Another useful quantity is water loading X_s, because it is based on the amount of dry air, which is not changing throughout the reactor.

$$X_s = \frac{\dot{m}_{\mathrm{H_2O}}}{\dot{m}_a} \tag{4.4}$$

The ‘Sensors’ page shows measured values including temperatures in the reactor (T_1, T_2 and T_3 (3x I-07)). ‘pDiff’ is pressure difference over the orifice plate (I-03) and ‘pAmbient’ overpressure before the orifice plate with respect to ambient conditions (I-02).
At the ‘Experiment’ page additional information regarding the currently conducted experiment can be entered (e. g. an experiment ID can be assigned). ‘Trends’ page makes it possible to view, for example, temperature profiles over time in order to get a better overview. The ‘Alarms’ page lists all programmed alarms which might occur. To set control parameters without the need of opening Automation Studio, the ‘Reactor’ page was created. Here, also the size of the used orifice plate and the type of reactor (‘metal’ or ‘glass’) can be adjusted. For these values to be accepted by the control system, operation has to be shut down (‘System’ button turned off at control room page). Table 4.2 lists used control parameters. To find values for air heater and reactor heater is challenging. For dehydration suitable parameters are found. They allow almost stationary operation. For hydration different values are tried throughout the experiments. However, no really satisfactory result is found just by varying parameters manually. Effort in control unit design would give better results. The difficulty lies in the wide operating range and disturbance variable compensation. Varying superficial velocities and changing mass flow rates of steam are main influence factors.

4.4 Issues and solutions

From an experimental point of view, some aspects concerning the testing plant should be considered. Condensation is an issue which needs to be addressed. If reactions are to be carried out close to the dew point, condensation after wet air exits the fluidized bed, must be prevented, either by additional heating, better insulation or geometrically different reactor design. Especially the funnel must be considered, since it was found to act as a condenser.

Ideally a steam generator is available, which produces steam on a constant basis (i. e. constant mass flow rate). Fluctuations are considerable with the presently available generator, which not only influences the hydration reaction, but also the operational stability of the plant (condensation). Construction of a steam drum could also solve the problem. Additionally, the connection point of the steam hose is too close to the air heater. Steam can easily damage the ceramic body and electronics of the heater. Installation of a safety device, which automatically seals off the area in between, in the case that there is no air flow present, could help protect the air heater.

Also, a strategy for reactor control should be created. Especially temperature control needs attention, including modeling and robust control design.

Furthermore, an inline measurement for calculation of conversion needs to be implemented again. Manual sampling, as it was done in this work, is time-consuming, discontinuous and is only possible at low temperatures (in this instance only for hydration reactions but not for dehydration). RECENDT[4], for example, offers near infrared and Raman-spectroscopy for inline monitoring in industrial environments. This could be a future method for inline measurement of material composition, if research is promoted in this direction.

---

[4] https://www.recendt.at

5 Material testing

This work focuses on the investigation of $MgO/Mg(OH)_2$. In this chapter information on the properties of $MgO/Mg(OH)_2$ in general, as well as on the material used for testing is given, before conducted experiments are explained.

5.1 Material properties

As a possible TCES system Pardo et al. [45] lists the following properties. A high theoretical energy density of $380\,\frac{\mathrm{kW\,h}}{\mathrm{m^3}}$ is possible. Reaction can be realized at an operating pressure of 1 bar. No catalyst is needed, no by-product is formed and it is readily available at a reasonable price. High reversibility is found to be one of the most promising advantages. Drawbacks include, that MgO reacts at ambient conditions to a certain degree. The reaction is also accompanied by a large volume change (~50 % [43]) and low thermal conductivity impeding heat exchange. For $Mg(OH)_2$ in a packed bed Lager [37] evaluates effective thermal conductivity as low as $0.11\,\frac{\mathrm{W}}{\mathrm{m\,K}}$. To overcome this limitation a FBR can be used.

5.1.1 Magnesium oxide

Magnesium oxide (MgO), also known as magnesia, occurs naturally in the form of the white mineral Periclase. Major deposits are found in China, Europe and Canada. MgO has a density of $3.58\,\frac{\mathrm{g}}{\mathrm{cm^3}}$ and a high melting point of 2852 °C. It is hardly soluble in water, but it is hygroscopic and reacts to $Mg(OH)_2$ [47]. It is identified by the CAS number 1309-48-4. Safety statements include: 'harmful if MgO fumes are inhaled'; 'MgO dust causes slight irritation of eyes and nasal mucosa'; 'not toxic' [30].

Many other forms of magnesium exist in nature. It is found in carbonates ($MgCO_3$, magnesite), chlorides ($MgCl_2 \cdot 6\,H_2O$), sulfates ($MgSO_4 \cdot H_2O$), silicates ($3\,MgO \cdot 2\,SiO_2 \cdot 2\,H_2O$) or hydroxides ($Mg(OH)_2$) to give a few examples. Production is mainly based on decarbonization of $MgCO_3$ or extraction from seawater or brines [22]. The known global reserve base for magnesite is about 13 billion tonnes [50]. MgO produced from $MgCO_3$ is manufactured by calcining at high temperatures in a multi-deck oven, for example, and is available in different grades. Depending on the calcination temperature, there is dead-burned magnesium oxide with hardly any reactivity (1500 °C to 2000 °C), hard-burned MgO produced at 1000 °C to 1500 °C and light-burned magnesium oxide (caustic magnesia) with relatively high reactivity at 700 °C to 1000 °C. Magnesite is often found as a mixed crystal of magnesium carbonate and iron(II) carbonate with calcium or small amounts of manganese, cobalt or nickel.

MgO is used in industry as refractory material in linings for blast furnaces, kilns or incinerators, for example. It is a component in sorel cement and used in building boards because of its fire resistance. In agriculture it is a source of magnesium in fertilizers. For the same reason it is used as animal feed supplement. It neutralizes acid streams and precipitates heavy metals in wastewater treatment plants. Many more applications could be listed, including many in chemical industry [47].

5.1.2 Magnesium hydroxide

Magnesium hydroxide ($Mg(OH)_2$), also known as brucite, is found in association with calcite, dolomite, magnesite,.... It occurs at many locations but rarely in crystalline masses [44]. It has a density of 2.345 $\frac{g}{cm^3}$ and is hardly soluble in water [47]. It can be produced by hydration of magnesium oxide. Since most applications utilize MgO instead of $Mg(OH)_2$, the hydroxide is, however, often used as a precursor for production of magnesium oxide through dehydration. About three quarters of the annual $Mg(OH)_2$ production are used for this purpose [50]. Ways to synthesize $Mg(OH)_2$ include processes using seawater or brine. Magnesium is present in seawater at a concentration of about 1.3 $\frac{g}{l}$ of Mg^{2+}-ions associated with chloride and sulphate ions. It can be extracted using lime.

$$MgCl_2 + Ca(OH)_2 \longrightarrow Mg(OH)_2 + CaCl_2 \tag{5.1}$$

Or by decomposing dolomite

$$CaMg(CO_3)_2 \longrightarrow MgO \cdot CaO + CO_2 \tag{5.2}$$

followed by hydration (this works because of the high temperature calcination in the first step – MgO is not reactive)

$$MgO \cdot CaO + H_2O \longrightarrow MgO \cdot Ca(OH)_2 \tag{5.3}$$

and reaction with magnesium salts (seawater) [4].

$$MgO \cdot 2\,Ca(OH)_2 + MgSO_4 + MgCl_2 \longrightarrow MgO \cdot 2\,Mg(OH)_2 + CaSO_4 + CaCl_2 \tag{5.4}$$

Milk of magnesia – a suspension of $Mg(OH)_2$ in water – is sold for medical applications. The use as an alkali to neutralize acidic wastewater is already mentioned in the section above. Because of its endothermic decomposition to MgO it has smoke suppressing and fire retarding properties [47].

5.1.3 Testing material

Four different batches of MgO and two different batches of $Mg(OH)_2$ are available for testing. Batches differ in particle size and calcination conditions.

First of all, the production process is described. $MgCO_3$ is extracted from a mine and crushed. In the lab it is grained and sieved. The fraction in between two sieves is taken and calcinated in an oven at about 650 °C. Temperature is intentionally kept low in order to achieve highly reactive material. At this temperature level the highly porous structure of $MgCO_3$ is kept intact whereas at high temperatures sintering occurs, resulting in low specific particle surface areas (i. e. large crystals) and/or porosities. The surface area is in direct correlation to material reactivity. This behavior can be explained as follows. For a chemical reaction to occur in a heterogeneous gas-solid system, the gaseous reactant has to be adsorbed on the solid's surface first. This is an important step not only in systems based entirely on sorption processes, but also with chemical reactions. Hence, increased surface area allows more molecules to be adsorbed. Liu et al. [40] correlates calcination temperatures to SSA. They conclude that surface area is strongly dependent on temperature, influencing the consecutive hydration reaction. Note, that temperatures applied in their experiments are much higher than in the FBR.

(a) MgO(2) coarse (b) $Mg(OH)_2$ coarse

Figure 5.1: Microscope images

Calcination is done in a lab-scale top-hat oven, where no movement of material can be achieved. Thus, 20 kg of material is burned multiple times in order to achieve high conversion rates. In order to obtain 20 kg of MgO about 40 kg of $MgCO_3$ is necessary. The rest escapes in form of CO_2. Because of immovable material and low burning temperatures, full decarbonization is not achieved. A few weight percent of carbonate are still present in the sample material.

The available six batches of material are assigned short names in order to reference them easily. The first batch of MgO is delivered with a nominal particle size distribution of 63 µm to 200 µm (referred to as MgO(1) fine) and a nominal particle size distribution of 500 µm to 700 µm (referred to as MgO(1) coarse). As TGA shows, carbonate contents are still high and vary strongly. The second batch has nominal particle size distributions of 200 µm to 500 µm (MgO(2) fine) and 500 µm to 1000 µm (MgO(2) coarse). This particle size range is determined by sieves used by the manufacturer of the materials, real size range differs. This second batch is also calcinated differently. Only a 1.5 cm thick layer is laid out in the oven. The assumption is that this results in a more uniform decarbonization.

Fig. 5.1a depicts a microscopic image of MgO taken with a light microscope. It is not purely white, but shows a slightly red discoloration. As mentioned above, this most likely stems from iron compounds. Additionally it is found, that about 1.8 wt% of CaO is present. Both occur naturally in magnesite. For the evaluation of experiments these components are not taken into account.

$Mg(OH)_2$ originates from seawater. On the exact production process no information is available. Again two different particles size fractions are available. 63 µm to 200 µm, which is referred to as $Mg(OH)_2$ fine, and 500 µm to 700 µm referred to as $Mg(OH)_2$ coarse. As can be seen in Fig. 5.1b $Mg(OH)_2$ is purely white. It is assumed that it is not contaminated with other elements (purity >99 %). In contrast to magnesium oxide it appears powdery and very soft.

In order to characterize materials better, basic measurements are carried out. Table 5.1 gives an overview.

Bulk density ρ_b is measured according to the respective standard DIN EN ISO 60. An apparatus is used, which simply consists of a measuring cylinder with a defined volume and a funnel with a somewhat larger volume than the cylinder, placed directly above. The funnel is filled with material. Opening the bottom lid allows material to flow into the cylinder. Since the funnel is bigger than the cylinder, material overflows. Excessive material is removed and the cylinder

Table 5.1: Measured and calculated properties of $MgO/Mg(OH)_2$

	ρ_b in $\frac{kg}{m^3}$	ρ_p in $\frac{kg}{m^3}$	$d_{SV}(d_p)$ in mm	$u_{mf,calc}$ in $\frac{cm}{s}$	$u_{mf,exp}$ in $\frac{cm}{s}$	$u_{t,calc}$ in $\frac{cm}{s}$	SSA in $\frac{m^2}{g}$
MgO(1) coarse	905	1811 (1790)	185	2	-	112	-
MgO(1) fine	713	1427 (1790)	107	0.53	-	39	-
MgO(2) coarse	702	1404 (1790)	179	1.5	-	95	44-56
MgO(2) fine	624	1249 (1790)	162	1.2	6.5	82	44-56
$Mg(OH)_2$ coarse	544	1089 (1173)	108	0.43	9.3	31	~ 27
$Mg(OH)_2$ fine	533	1067 (1173)	47	0.08	-	6.6	~ 27

filled to the top, is weighed.

Particle density can be measured using helium pycnometer or mercury porosimetry. With small, porous particles, like the investigated material, these techniques cannot be used. There is no appropriate method known to determine particle density in this case. Approximations can be applied. One way is to use Eq. 3.35 and guess void fraction ε_p. For spherical, not too small particles, a void fraction of 0.4 to 0.45 is a good approximation. The lower sphericity and the smaller particle diameters the higher porosity is. A void fraction of 0.5 is thus assumed. Results are listed in the table. Another approach is to calculate particle density based on absolute material densities. These values were already given in section 5.1.1 and 5.1.2. According to the manufacturer these particles can have porosities up to 50 %. Using this value, particle densities can be calculated applying Eq. 5.5.

$$\rho_p = \rho_{p,abs} * (1 - \varepsilon_p) \tag{5.5}$$

Values are given in brackets in Table 5.1. Both calculation methods are based on vague approximations and deviations from true values can be large. For calculation of u_{mf} values from the first method are used, because they are based on experimental results of bulk density. Values show expected behavior. Comparing MgO batches gives higher bulk densities for coarse fractions and for material with wider size distribution (MgO(1) has more dust).

For determination of the Sauter-diameter d_{SV} two different approaches can be applied. First, note that no differentiation between d_{SV} and d_p is made, since spherecity is unknown (cf. section 3.3). One method is to use a sieve tower. This, however, turns out to be not applicable. Fine material fractions tend to coagulate on mesh sizes far greater than their actual diameter. Sieving aides improve the situation, but the result is still not sufficient. Errors would be to great. The second method is to use a particle size analyzer. This method is further pursued (description of method see section 6.1.6).

Initial particle size distribution for all used materials is given in Fig. 5.2. It can be clearly seen, that the actual distributions differ considerable from nominal sizes given above. Two reasons come to mind. One is, that sieving is not done properly. The other is, there might be alterations during the calcination process, because sieving is done before and not afterwards. Mode values[1] of coarse materials are much smaller than expected. For example, MgO(1) coarse shows a mode of about 300 µm, where a value between 500 µm to 700 µm is expected. All mate-

---

[1] The particle size, which occurs most often in the collective

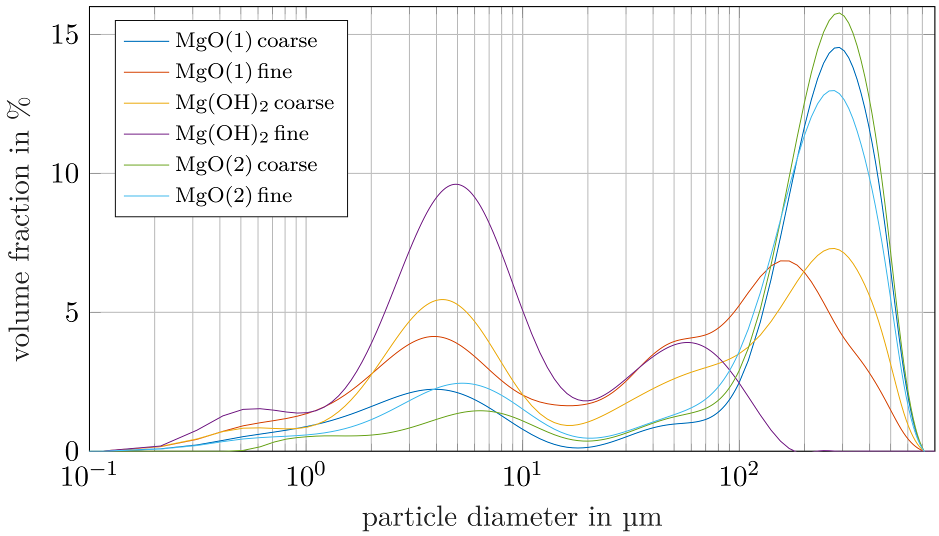

Figure 5.2: Particle size distribution of initial material created with Mastersizer 2000

rials have in common, that particle size distribution is bimodal (i. e. has two peaks). Bimodal distributions have adverse effects on fluidization behavior and hydration. This bimodal distribution consists of the main fraction and a dust fraction with a mode value of about 4 µm. This fraction is unwanted and most likely results from inadequate sieving and/or fragmentation during calcination. For Mg(OH)$_2$, another explanation for the dust fraction is found. Mg(OH)$_2$ is produced by agglomerating small primary particles of about 4 µm. If the agglomeration process is incomplete residual primary particles can be present.
Especially Mg(OH)$_2$ fine shows such a high dust load, that it constitutes the main part of the material. MgO(2) coarse shows lower dust loads. This can be confirmed visually in the fluidized bed reactor. The mode value, however, is identical to MgO(1), even though different sieves were used. MgO(2) fine shows only a minimal smaller mode value than the associated coarse fraction. This surprises, because visually, the material appears to be finer and also fluidizes at lower velocities (Mastersizer analysis is usually very reliable). In general, further batches should aim at a narrower, unimodal distribution.

For calculation of d_p and u_{mf}, the two fractions have to be considered separately. A new distribution is calculated by separating the two fractions at the local minimum in volume fraction (at about 20 µm). Values given in Table 5.1 only show the main fraction, dust fraction is not displayed. Calculating terminal velocity for the dust fraction shows, that at parameters used for experiments, terminal velocity is by far exceeded. Thus, dust is entrained from the reactor. d_p is calculated by using the harmonic mean (Eq. 3.33) and presented equations for u_{mf} in section 3.3 (Eq. 3.34 and Eq. 3.35). Terminal velocity is calculated using Eqs. 3.36 and 3.37. Sphericity is not known and therefore u_t for spherical particles is calculated. Unfortunately, calculations underestimate u_{mf} by far as visual confirmation in the next section shows. Values are given in the table, but should not be used for further consideration.

With determined values classification according to Geldart can be accomplished (Fig. 3.6). Keep in mind, that these values are approximations and the diagram itself does not separate

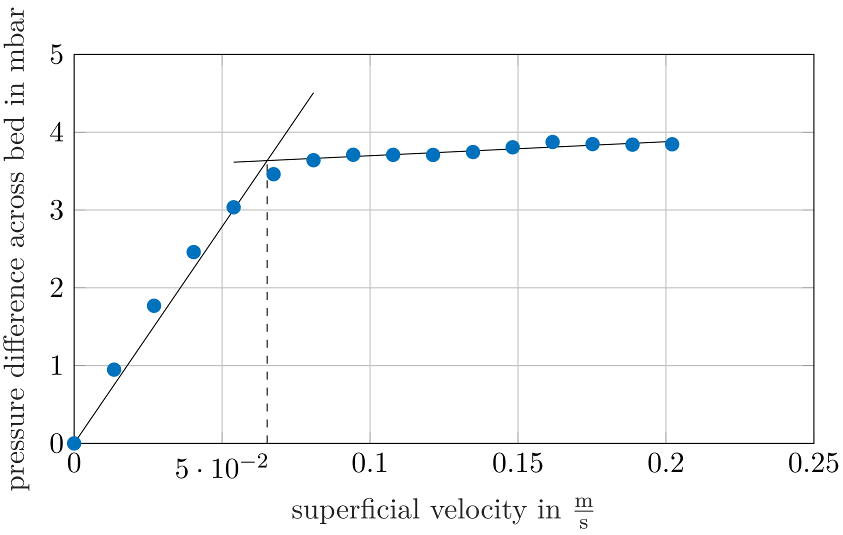

Figure 5.3: Determination of u_{mf} of MgO(2) fine

groups at a distinct point. Passages are fluent. Both MgO batches (coarse and fine) are categorized in the AB region. $Mg(OH)_2$ fractions are in category A. However, the used diameters do not take the dust fraction into account. Especially $Mg(OH)_2$ fine shows partly behavior of a category C material. Considering the high dust load, this comes as no surprise. Also, MgO(2) appears much coarser in comparison to MgO(1) because dust fraction is reduced.

In order to measure u_{mf} experimentally, some attempts were made to record the pressure drop across the distributor plate in an empty reactor and with material. The difference gives pressure drop across the bed. From this value minimal fluidization velocity, as described in section 3.3, can be calculated. Two factors, however, make the determination impossible. On the one hand, minimum flow rates are too high for measurement under fixed bed conditions. On the other hand, the sinter metal plate tends to clog, changing pressure drop over time. After cleaning the plate with pressurized air and a wire brush, pressure drops can be reduced again. Another test rig, specifically designed to measure minimum fluidization velocities is used instead. It is based on the same principle. A quadratic perspex box with a perforated plate as distributor is perfused by air. Pressure difference is again measured across plate and bed material. Fig. 5.3 depicts pressure difference across the bed over superficial velocity. u_{mf} is calculated by determining the intersection point of the two regression lines.
This method gives – in this case – higher minimal fluidization velocities as the definition would suggest. Vigorous, uniform bubbling can be observed. First bubbles already occur at 4 $\frac{\mathrm{cm}}{\mathrm{s}}$.
Unfortunately this approach only works with MgO(2) fine and $Mg(OH)_2$ coarse. All other materials do not show the characteristic pressure drop curve. Minimal fluidization velocities are therefore determined visually. Further discussion follows in section 5.2.
Specif surface area (SSA) gives the (inner) surface area per gram of material. It is an important value, because it allows statements on the reactivity of the material and it is also directly related to the crystal size. The higher SSA, the more surface area is available and the faster kinetics will be. Later, effects of dehydration temperature on SSA will be discussed. Values depicted in Table 5.1 are surface areas of the initial material after the calcination process.

Table 5.2: Visually determined u_{mf}, discharge and median of volume distribution

	u_{mf} in $\frac{\mathrm{cm}}{\mathrm{s}}$	discharge in g		median in µm		
		low	high	initial	low	high
MgO(1) coarse	13	4.2	25	212	235	260
MgO(1) fine	4	27.4	29.3	75	129	139
MgO(2) coarse	17	-	-	228	-	-
MgO(2) fine	6	-	-	188	-	-
$Mg(OH)_2$ coarse	13	3.1	2.0	54	85	109
$Mg(OH)_2$ fine	(6)	28	25.1	5.7	5.7	5.8

5.2 Cold flow experiments

In this section results of cold flow experiments are summarized and discussed. The aim is to qualitatively assess fluidization behavior, visually determine minimum fluidization velocity and evaluate the effects of mechanical stress on particles (fragmentation, abrasion). The glass reactor is used in order to monitor processes visually.

Minimum fluidization velocity was already discussed in the last section to some extent, but results were unsatisfying. Thus, a more viable alternative is to determine it visually. Here, observations from the glass reactor are used. Values are depicted in Table 5.2. They are estimated at a point where uniform smooth bubbling occurs for the first time. This is a very practical approach which is not consistent with the definition of u_{mf} – true values are actually smaller. Nevertheless, these values are referenced in all other experiments. For example, if a fluidization number of 2 is mentioned, it refers to the values defined here. Note, that the point where uniform bubbling occurs depends on the gas distributor. The perforated plate used in the perspex box is able to achieve uniform bubbling at lower velocities. The sinter metal plate tends to distribute the gas unequally, resulting in higher velocities at the point of uniform bubbling.

For $Mg(OH)_2$ fine no distinct point can be defined. It shows behavior of a class C material according to Geldart, where cohesive forces are strong. Already at low velocities (below 1 $\frac{\mathrm{cm}}{\mathrm{s}}$) jets of material, like fountains, start to shoot out from the bed (similar to channeling). There is no bubbling going on and labeling this state a fluidized bed would be incorrect. With increasing velocity bubbles start to appear. Fluidization is already violent, but a phase in between does not exist. Since u_{mf} cannot be defined reliably, after careful consideration 6 $\frac{\mathrm{cm}}{\mathrm{s}}$ is chosen as a representative value. High dust load, which is clearly categorized in class C, in combination with the actual class A material, results in this fluidization behavior. All other batches fluidize easily.

The following example should give an explanation why the above mentioned state of uniform bubbling is chosen for u_{mf}. For MgO(1) coarse 0.13 $\frac{\mathrm{m}}{\mathrm{s}}$ is picked, because below this velocity small channels start to appear on the bed surface. This only happens in some areas of the bed, the rest of the material is still fluidized and theoretically minimum fluidization velocity is still exceeded. However, this state is detrimental, because some material is immobilized and thus the advantages of a fluidized bed cannot be utilized. Same behavior can be seen with

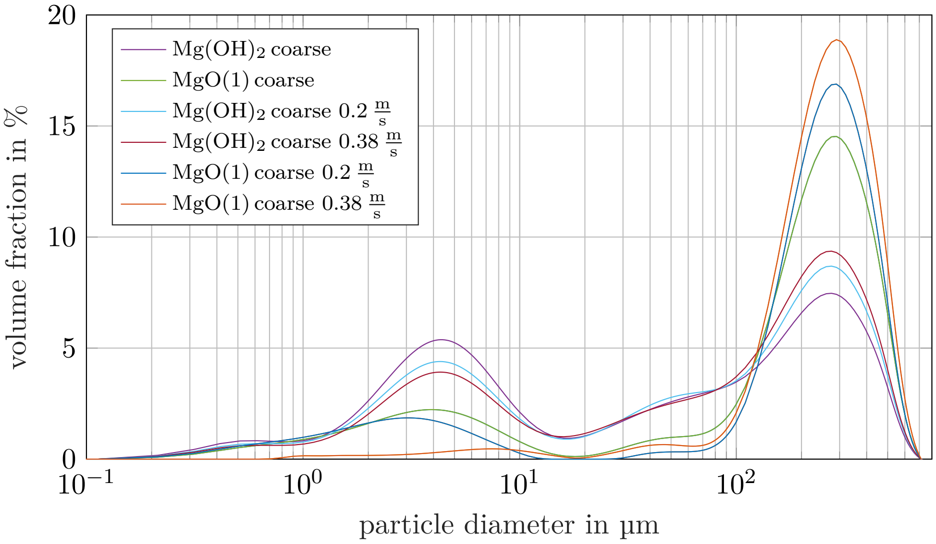

Figure 5.4: Particle size distribution: Comparison before/after fluidization, coarse mat.

$Mg(OH)_2$ coarse. Clogging of the sinter metal plate is suspected to be the cause.
Note, that all experiments in this section are carried out at ambient conditions. Hydration and dehydration, however, take place at elevated temperatures. Minimum fluidization velocity is a function of temperature. Both Eqs. 3.34 and 3.35 need gas density and dynamic viscosity as a parameter, which are, of course, temperature dependent. For hydration a temperature of 100 °C is assumed, for dehydration 350 °C. Minimum fluidization velocity is decreasing at higher temperatures. At 100 °C a reduction of 17 % and at 350 °C a reduction of 42 % is calculated. For experimentation this deviation is not further respected. Values of gas density and dynamic viscosity are taken from VDI-Wärmeatlas.

In order to determine if abrasion or fragmentation occurs, all batches are fluidized for 24 h and particle size distributions after the experiment are compared to the initial material. This is done at two different fluidization velocities in order to determine the dependency of it on abrasion or fragmentation. For all experiments 400 g of material is used. This value is chosen, because on the one hand the bed height should not be too low. On the other hand, only about 20 kg of material is available.
In Fig. 5.4 the influence of abrasion and fragmentation is depicted for MgO(1) coarse and $Mg(OH)_2$ coarse. Both materials are fluidized at $0.2\,\frac{m}{s}$ and $0.38\,\frac{m}{s}$, which equals a fluidization number of about 1.5 and 3, respectively. The curves show that no particle alteration occurs due to mechanical stress during fluidization. Only the dust fraction is carried out of the reactor to some extent. In the diagram this is reflected by a proportionately higher peak for the main fraction and a lower peak for the dust fraction. For MgO(1) coarse at $0.38\,\frac{m}{s}$ dust is almost completely removed. Analyzing the carried out dust confirms the assumption that no fragmentation occurs since the exactly same dust fraction is found again. $Mg(OH)_2$ exhibits only a small reduction in dust load even though terminal velocity is exceeded by far. It appears that small particles adhere on larger ones or form agglomerates, simulating larger particles with a higher terminal velocity. Fig. 5.5 depicts same results for MgO(1) fine and $Mg(OH)_2$ fine. Here, also most of the dust fraction, especially for $Mg(OH)_2$ fine, is not carried

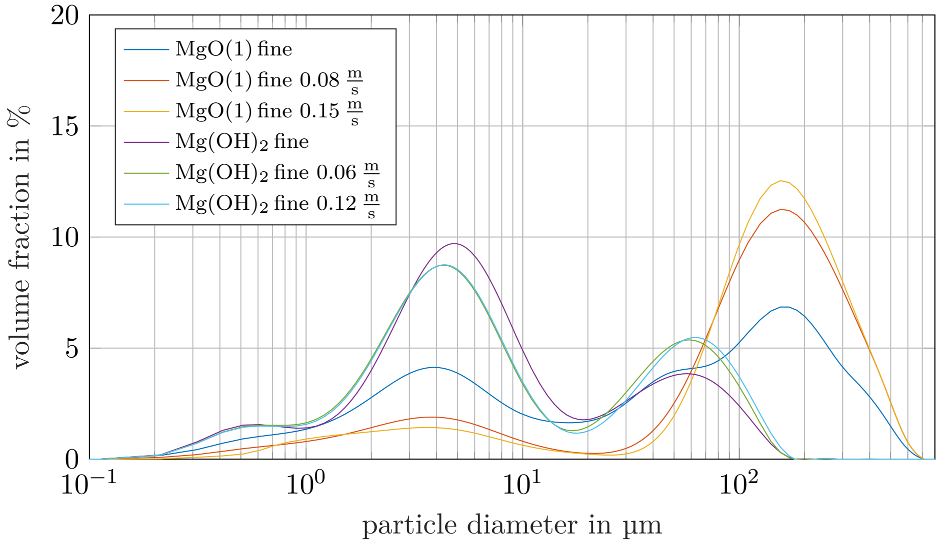

Figure 5.5: Particle size distribution: Comparison before/after fluidization, fine mat.

out. Superficial velocities are chosen accordingly.

Table 5.2 summarizes the amount of dust carried out from the reactor which is gathered in the filter. 'Low' and 'high' refer to velocities used for cold flow experiments as they are depicted in Fig. 5.4 and Fig. 5.5. In order to retrieve dust, the filter is cleaned twice with pressurized air. By opening the butterfly valve dust is collected and weighed. Note, that the amount of dust does not necessarily constitute all material that is lost during fluidization. Some is retained in the pipes or the filter and some might not be separated and thus conveyed with the exhaust air. Results are not explicit, a few deductions can nevertheless be made. MgO(1) coarse shows low amounts of dust at a low velocity. Fluidization at 0.38 $\frac{m}{s}$ is sufficient, to carry out most of the dust. Mg(OH)$_2$ coarse does not exhibit major dust loss even at high velocities. Both is in accordance with Mastesizer curves. All fine materials show high amounts of discharged dust. Mg(OH)$_2$ fine seems to have such a high dust load, that even 28 g of carried out dust does not seem to change particle size distribution much.

From the results in this section it becomes clear, that the amount of carried out material highly depends on the material. The fact that the terminal velocity for the dust fraction is exceeded does not seem to have an impact.

Some other effects during 24 h of fluidization can be detected. When the experiments are started, dust is present in the reactor. This can be visually confirmed, because small particles fill the upper part of the reactor (above the actual bed). After 24 h (or presumably earlier) a clear view is given and no material is seen above the bed height. Some of the dust was carried out and u_{mf} is therefore shifted to slightly higher velocities. With MgO(1) fine, after 24 h, parts of the bed are not fluidized anymore. It is assumed that fine particles block the distributor plate. This would also explain varying pressure drops, as was mentioned before.

Another observed effect is that MgO reacts within 24 h of fluidization at ambient conditions to a certain degree. By adding up the weight of material taken out of the reactor and the weight of the dust fraction, it is seen, that the sum exceeds the initial weight. This is proof that material reacts with the water in the ambient air. Especially MgO(1) coarse shows unusually high conversion. 450 g of material are taken out of the reactor when initially 400 g are weighed

in.
Table 5.2 also depicts the median diameters of volume distribution[2] for each material. 'Initial' stands for material as it is delivered (before experimentation). 'Low' and 'high' was already explained above. It is obvious, that the median is increasing the more dust is carried out. $Mg(OH)_2$ fine hardly shows any change – dust fraction is still predominant.
In the perspex box setup, different bed heights are tested. Observation complies with theory. Increased bed height allows the bubbles to coalesce. Bigger bubbles result in less surface area of the bubble phase and can therefore have adverse effects on kinetics. Also, spouting on bed surface is more violent.
Many videos and pictures recording the above mentioned effects were made and are available as supplementary material on request.

5.3 Hydration

Hydration constitutes the energy discharge reaction of the TCES process. Steam is added to MgO, which then reacts to $Mg(OH)_2$, releasing energy in the process.

$$MgO_{(s)} + H_2O_{(g)} \longrightarrow Mg(OH)_{2(s)} \tag{5.6}$$

Theoretically a reaction enthalpy of $\Delta H_R = -81.23\,\frac{\text{kJ}}{\text{mol}}$ or $\Delta H_R = -2015.63\,\frac{\text{kJ}}{\text{kg}}$ of magnesium oxide can be released at standard conditions. If the temperature dependcy of the reaction enthalpy is considered (according to formulas in section 3.2.1), slightly different values result for a temperature of 100 °C ($\Delta H_R = -80.49\,\frac{\text{kJ}}{\text{mol}}$ and $\Delta H_R = -1997.2\,\frac{\text{kJ}}{\text{kg}}$ of MgO).
For experimentation steam is electrically generated. This approach works well for testing, but for actual applications, producing steam just for the purpose of releasing stored heat consumes too much energy. Calculations show that more than 50 % of the stored energy would be required for steam production this way – assuming full conversion (!). If conversion is lower, energy needed for steam production might even outweigh the released amount of energy. Additionally, heating up solids from ambient to reaction temperature again requires heat (about 37 % of the produced heat [19]). Solid pre-heating, like it was proposed in section 3.4, would increase efficiency. A different approach currently being investigated, utilizes liquid water as reactant. The reaction enthalpy is lowered to $57.4\,\frac{\text{kJ}}{\text{mol}}$ but the equilibrium temperature rises to 552 °C. Additional problems, like clumping, arise. Also, using stoichiometric amounts of water makes uniform water distribution necessary. If more water is added, most of the energy would again be wasted on heating up and evaporating water, only this time in the reactor itself. This was already discussed on the basis of the equilibrium curve in section 3.2.1.

Investigations focus on the kinetic behavior of MgO. Results should be able to answer questions on how fast the reaction occurs, how long it takes until reaction is finished or if complete conversion is even possible. Additionally, the obtained material is examined regarding its particle size distribution in order to see if any change in grain size occurs.
Many parameters come to mind, when thinking about experiments. Considering kinetics, reaction temperature and steam partial pressure are important as was shown with Eq. 3.22. These two parameters are varied. More specifically, a temperature range from 80 °C to 120 °C

---

[2] Median represents the diameter where 50 % of all particles in the probe are smaller than the median diameter and 50 % are larger. Here, values are given for volume distribution. Meaning that 50 % of the particles have a smaller volume and 50 %have a larger volume than the median diameter.

Table 5.3: Parameter combinations for investigation of MgO(1)

MgO(1) coarse		MgO(1) fine	
p_{H_2O} in bar	T_R in °C	p_{H_2O} in bar	T_R in °C
0.2	80	0.2	80
	100		
	120		
0.4	80	0.4	80
	100		100
0.6	110	0.6	110

is considered. Partial pressures range from 0.2 bar to 0.6 bar. These values are chosen, because chemists at TU Wien already conducted small scale hydration experiments using continuous STA measurements within these parameter ranges. This allows comparison of results. Also, operation closer to the equilibrium curve (which is actually desirable in order to achieve high exergetic efficiencies) would result in kinetics far too slow to achieve high conversion within a reasonable amount of time [19]. As a third parameter the available four different batches of MgO can be seen. Another parameter is fluidization velocity. Influence of different fluidization numbers on kinetics is neglected. It is chosen according to results of cold flow experiments. A certain limitation is imposed by the operating range of the experimental plant itself. Also, bed height and thus the amount of material utilized with the reaction could have an influence, as was discussed before. This is neglected as well.

Again, the two different setups, as described above, have to be considered. With the first setup, using the Condair steam generator, the oxygen probe but no reactor heating, only MgO(1) is investigated. In the following section only these experiments are described.

5.3.1 First setup

Table 5.3 depicts all parameter combinations which are investigated. The goal is, to vary partial pressure at constant temperature and vice versa. That way, influence of both parameters on kinetics can be treated separately. But also knowledge on which parameters result in high conversion and fast kinetics is generated. Superficial velocities are set to 0.2 $\frac{\mathrm{m}}{\mathrm{s}}$ for both fractions. The steam generator makes this necessary. Minimum steam production rate is 2.5 $\frac{\mathrm{kg}}{\mathrm{h}}$, as already mentioned. In order to set partial pressure to 0.2 bar, the fine material has to be fluidized at a higher velocity. The amount of material is again set to be 400 g. Reaction time is 3 hours.

Before experiments are discussed a few idiosyncrasies concerning operation of the plant need to be considered.

Note, that temperature T_{in} is controlled. It is measured just below the gas distributor plate. T_1 is measured about 5 cm above the sinter metal plate. If material is fluidized, temperature sensor T_1 is in direct contact with material. T_2 and T_3 measure gas temperature above the bed at distances of about 10 cm. T_{out} is placed in vicinity of the oxygen probe and therefore measures temperature about 2 m after the reactor.

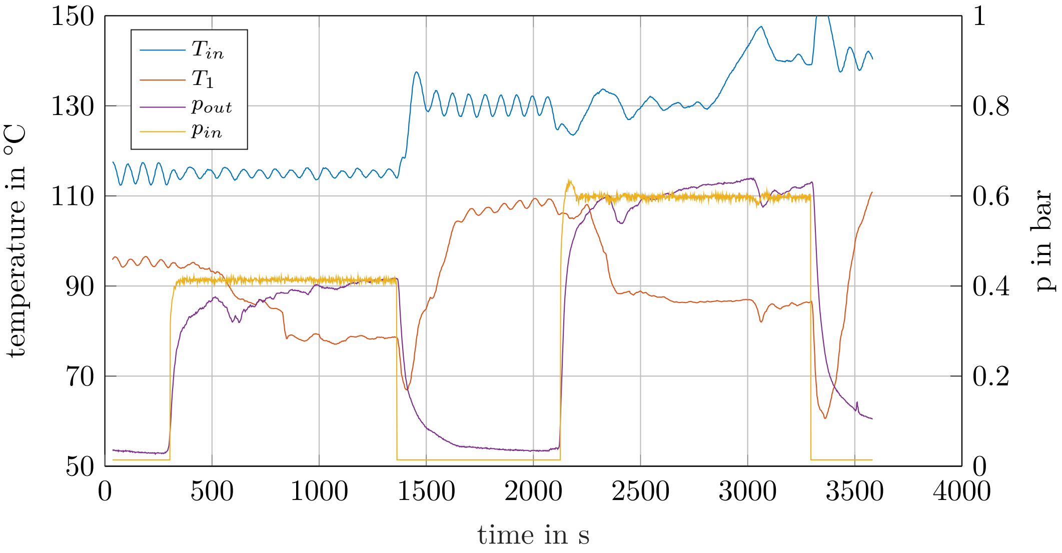

Figure 5.6: Influence of steam on temperature, Condair steam generator

Experiments are carried out by preheating the reactor without material first . If equilibrium condition (constant temperatures) is achieved, steam is added. Here, first difficulties are encountered as Fig. 5.6 depicts. Calculated partial pressure at reactor entry and measured partial pressure at reactor exit as well as T_{in} and T_1 are displayed. Once steam is added, it takes a while for p_{out} to reach p_{in}. But eventually deviation of calculated and measured values is minimal. Unfortunately p_{out} shows a value greater than zero when no steam is present. Steam is added at ambient pressure, hence, it has a temperature of 100 °C. Nevertheless temperature T_1 drops considerably once steam is present. T_{in} is controlled and does not show any change. This behavior is however not based on a perfect controlling system. At least a little disturbance should be seen before control adjusts temperature again. The only other explanation remaining is, that there is no influence on T_{in} and drop in T_1 results from phenomena occurring while wet air flows through the distributor plate. Temperature differences between T_{in} and T_1 are already high without steam, but are tremendous with steam. Remember that these two temperature sensors are only 10 cm apart. The increased drop with steam might be caused by increased heat transfer coefficients of wet air in relation to dry air. Problematic is, that at 0.4 bar saturation temperature is at 76 °C, for 0.6 bar at 86 °C [55]. Below these temperatures condensation occurs, which has to be prevented. Practically at least a reserve of 5 °C should be abode.

When steam production is stopped, temperature decreases shortly before initial values are restored. Another important result can be seen at about 3000 s on the time axis. An increase in T_{in} of 10 °C does not have any effect on T_1 when steam is present. The ability to control reaction temperature T_1 is reduced. Nevertheless, control of T_1 is tried. It turns out that T_1 shows such a slow response to the manipulated variable that controlling is not feasible (or only with increased effort in designing the control system). Hence, T_{in} is controlled in all following experiments.

Fig. 5.7 depicts temperature curves for hydration at 0.4 bar and 80 °C. $\bar{T}_1$ gives mean temperature over the full length of the experiment and is represented by the dashed line. T_1 is

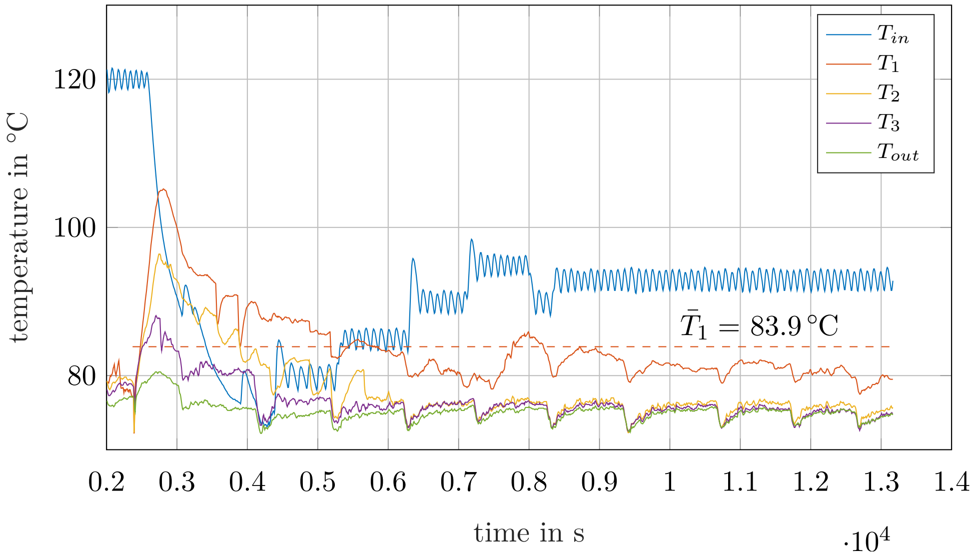

Figure 5.7: Temperature curves of hydration reaction at 0.4 bar and 80 °C, MgO(1) coarse

measured within the fluidized bed material and therefore is the best available representative for reaction temperature. The first few minutes displayed in the graph show preheating conditions. Temperatures in the reactor are held at about 80 °C. Again a substantial temperature difference to T_{in} can be seen. The point, when material is added by opening the butterfly valve below the funnel is denoted by a minimal temperature drop followed by a steep incline. The decrease originates from sensible heat, because material is added at ambient temperature and needs to be heated up first. However, reaction enthalpy almost immediately outweighs this effect and temperature starts to increase. The temperature peak within the first hour encourages the assumption that kinetics are fast in this time frame. Later on reaction slows down or halts completely if temperature curves are an indicator for conversion rates. As can be interpreted from the graph, T_{in} is manually adjusted. In this stage of experimentation different approaches are attempted in order the find the best solution. One approach is to try and keep T_1 as constant as possible by lowering reactor inlet temperature. A limitation imposed by the system is, however, condensation temperature, which must not be undercut. The graph already forestalls, that the temperature peak cannot be prevented.
T_2, T_3 and T_{out} each show a temperature difference to T_1. Heat losses are substantial. In this case, these temperatures converge at condensation temperature of 76 °C. This poses another problem. Even if condensation is prevented at reactor inlet or in the bed itself, heat losses above the bed material can lead to condensation, resulting in a return flow of water back into the bed. In order to prevent this, reaction temperatures need to be on a higher level. Interesting is, however, that 76 °C is the saturation temperature for a partial pressure of 0.4 bar. This could be another validation that partial pressure is indeed at the desired level.

The associated pressure curves are shown in Fig. 5.8. Measured value p_{out} follows calculated value p_{in} closely. This confirms again, that both calculation and measurement methods are applicable. Periodic fluctuation in partial pressure arises from the fact, that the steam generator draws water periodically, resulting in diminished steam production, as is described in section 3.1.3. This decrease in partial pressure also influences temperature. The same

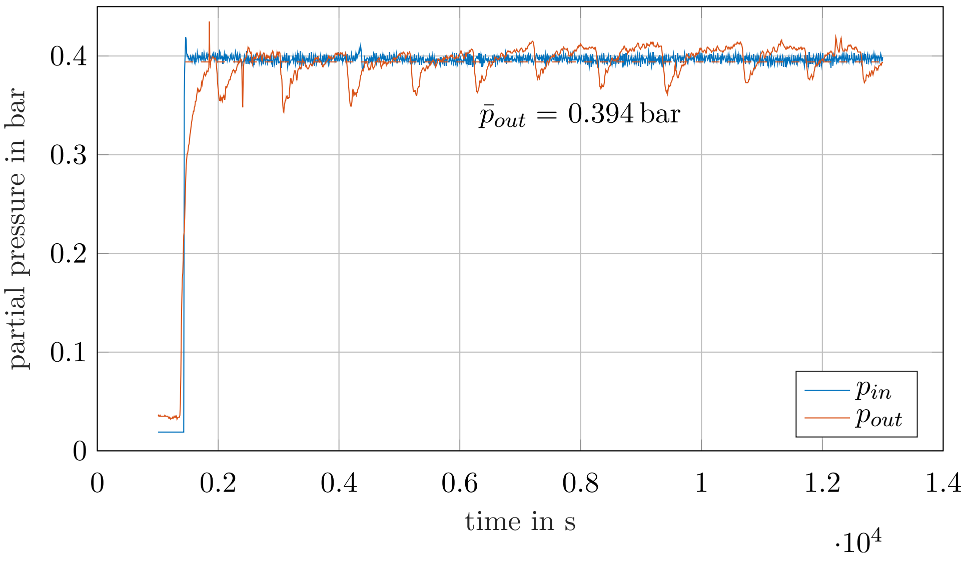

Figure 5.8: Pressure curves of hydration reaction at 0.4 bar and 80 °C, MgO(1) coarse

periodic fluctuation can be seen in temperature curves, where a drop in pressure results in a temperature drop. Especially at 0.6 bar variation can go up to ±0.05 bar. As long as mean partial pressure does not deviate largely, influence on results is neglected. The most important statement is, when adding material and reaction takes place (at about 2400 s on the time scale), no change in partial pressure can be seen. This affects evaluation methods as will be seen later.

Another example is given in Fig. 5.9. Here, the other method (keeping T_{in} constant) is tested. This allows experiments to be theoretically reproducible since T_{in} is clearly defined. The drawback is, however, that T_1 remains at a temperature level much higher than intended. Note, that preheating conditions are the same as before, and temperature cannot be lowered any further because of condensation. Thus, a mean reaction temperature around 80 °C cannot be achieved this way. In contrast to temperature curves shown before, all temperature curves stay above condensation temperature. Temperature differences due to heat loss can be observed over the whole duration of the experiment. Interesting is, that T_{out} does not follow the characteristic trend. Partial pressure curves are not depicted here, but according to the oxygen probe measurement, mean p_{out} is at 0.444 bar.

An experiment (MgO(1) fine at 0.6 bar and 110 °C) which does not show the intended outcome is depicted in Fig. 5.10. Once steam is added, temperatures start to plummet. As countermeasure material is added, which immediately results in an temperature increase. If material would not have been added, temperatures would have continued to drop below condensation temperature. This should illustrate, that the condition where steam is present, but no material, is very unstable. A small deviation, like the steam generator drawing water, can lead to a collapse of the system. With the second setup this is discussed further. The further course of the reaction is characterized by slight increase in temperature and stabilization at 115 °C. A characteristic temperature drop, once conversion rates decline, cannot be observed. The same behavior is observed at the reaction of MgO(1) fine at 0.4 bar and 100 °C. The cause for this behavior has not been identified. Another peculiarity is, that

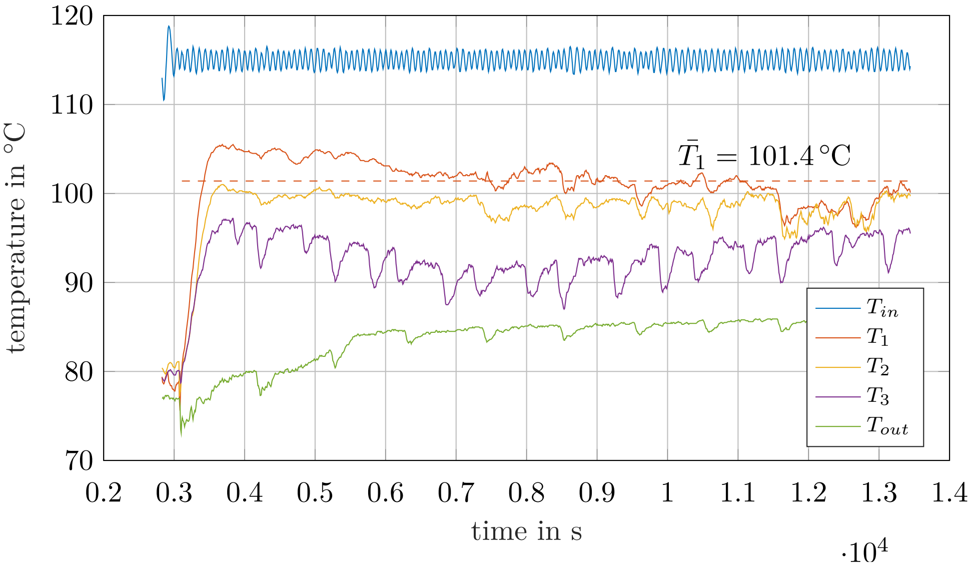

Figure 5.9: Temperature curves of hydration reaction at 0.4 bar and 100 °C, MgO(1) coarse

T_3 falls below T_{out} and is suddenly increasing within the last 2500 s, conditions unchanged. It is physically impossible for T_3 to fall below T_{out}, since no heat source is installed which would allow temperature to increase again.

Visual appearance of material after hydration is depicted in Fig. 5.11. Fine MgO(1) tends to form agglomerates as is shown in Fig. 5.11a and Fig. 5.11b. At 0.4 bar and 100 °C platelets of MgO are present. These fragments were part of a plate covering the gas distributor before material was taken out of the reactor. If looking closely, an imprint of the surface structure of the sinter metal plate can be seen. It is assumed, that this occurred mainly because of water already being present when material is introduced into the reactor. Temperature curves are (only in the beginning) similar to Fig. 5.10, where temperatures plummet before material is added. Condensation might have already occurred.

Fig. 5.11b shows a different form of agglomeration. Pellets of about 1 cm in diameter are forming. This is believed to be caused by water condensing on the reactor walls and flowing back down into the bed, where together with material movement due to fluidization, pellets are formed. The assumption that condensation occurs is supported by the temperature curve given in Fig. 5.10. Also, marks, showing traces of runlets on the reactor wall – as depicted in Fig. 5.11c, are present. This behavior is only observed with these two reactions. Condensation, together with the high amount of fine particles is believed to be the cause.

Coarse material forms clumps of wet material on the reactor wall (Fig. 5.11c). This is observed with nearly all reactions. The reason is the same as with fine material. Water is running down along the reactor wall until it gets into contact with spouted material from the fluidized bed. A nucleation site is forming, where the clump starts to grow over time.

Observations show, that clumping on the reactor wall always occurs at the same place. The funnel is found to be the reason. It lies outside the insulation and is not heated. Hence, it basically works as a condenser. Steam is condensed inside and flows back down the reactor wall, forming clumps directly beneath.

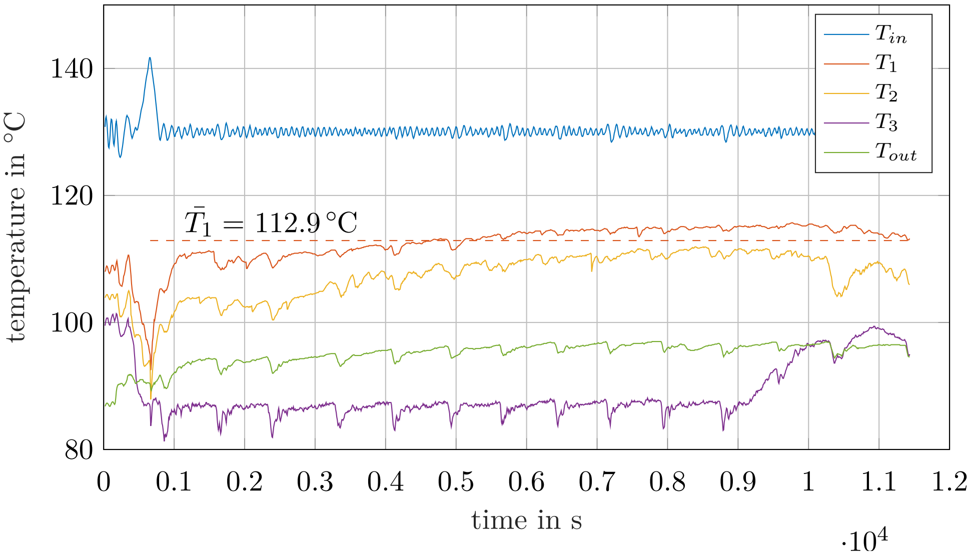

Figure 5.10: Temperature curves of hydration reaction at 0.6 bar and 100 °C, MgO(1) fine

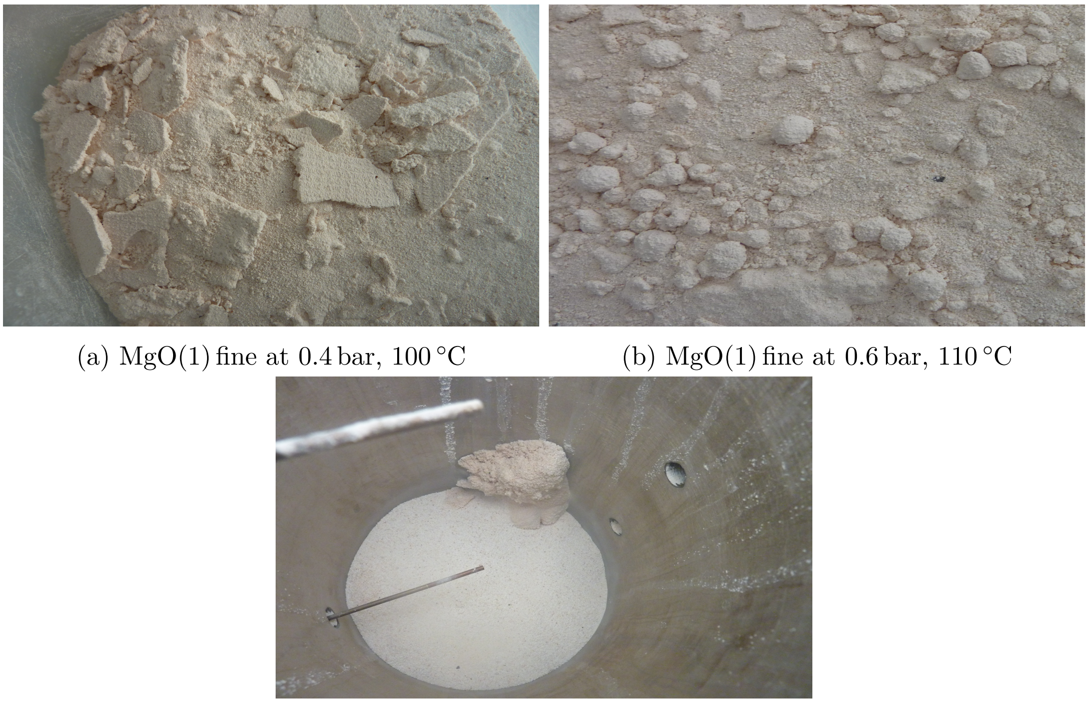

(a) MgO(1) fine at 0.4 bar, 100 °C

(b) MgO(1) fine at 0.6 bar, 110 °C

(c) MgO(1) coarse at 0.4 bar, 100 °C

Figure 5.11: Visual appearance of material after hydration

Table 5.4: Parameter combinations for investigation of MgO(2)

MgO(2) coarse		MgO(2) fine	
p_{H_2O} in bar	T_R in °C	p_{H_2O} in bar	T_R in °C
0.4	80	0.4	80
	100		100
0.6	100	0.6	100

In general, experiment control turns out to be challenging. As is made clear by the depicted tests, reaction temperature varies from experiment to experiment. Mean temperature is therefore a function of the used material and varying experimental procedure (e. g. it is difficult to anticipate when temperature drops and therefore condensation occurs). Additionally, if temperature control according to Fig. 5.7 is chosen, it depends on the ability of the person conducting the experiment, to guess the mean temperature beforehand. When thinking about it, the question arises, if mean temperature even has any significance. Reaction temperatures are deviating by far from this value, especially in the beginning of the reaction where conversion rates are high. Nevertheless, it is used for identification of experiments.

In general, hydration experiments conducted with the first setup are, in hindsight, considered to be important for generating knowledge on plant operation. Results are (as will be seen) of less significance.

5.3.2 Second setup

The goal in this section is to repeat some of the experiments from the first setup. Only this time, a different batch of magnesium oxide is used (MgO(2)) and evaluation is carried out differently. The goal is to acquire conversion - time curves. Material is thus taken out of the reactor at certain time intervals. The metal reactor has three unused boreholes as is shown in Fig. 4.12a. A small curved tube is inserted through the lower borehole into the fluidized bed, where the tube is filled with material. This is repeated multiple times to gather enough material for one sample.

Remember that the Ghidini steam generator is used with this setup. Fluidization velocities can be adjusted more flexible, because of the wider operating range of the steam generator. For MgO(2) coarse it is set to be 0.33 $\frac{\mathrm{m}}{\mathrm{s}}$, for MgO(2) fine to 0.12 $\frac{\mathrm{m}}{\mathrm{s}}$. This is equivalent to 2x u_{mf} for both fractions. Other parameters are unchanged. 400 g of material is hydrated for 3 h. Table 5.4 lists investigated parameters. Because of low conversions found for 0.2 bar these settings are not repeated.

First, behavior of the steam generator is tested. Fig. 5.12 depicts the recorded temperature curves.

The experiment is carried out at 0.6 bar and a superficial velocity of 0.33 $\frac{\mathrm{m}}{\mathrm{s}}$. Steam is added at second 750. Besides increase in T_{out}, no change in temperature is noticeable within the first minutes. Soon temperatures start to drop slightly. This is also characterized by an increase in pressure drop across the distributor plate from 600 Pa to 2200 Pa and increased compressor power (pressure curves are not displayed in this graph). Temperatures are as low as 87 °C in this area, ergo condensation is an issue and explains increased pressure drop. Once steam supply is suspended, temperature drops as low as 40 °C. Condensed water is evaporated and

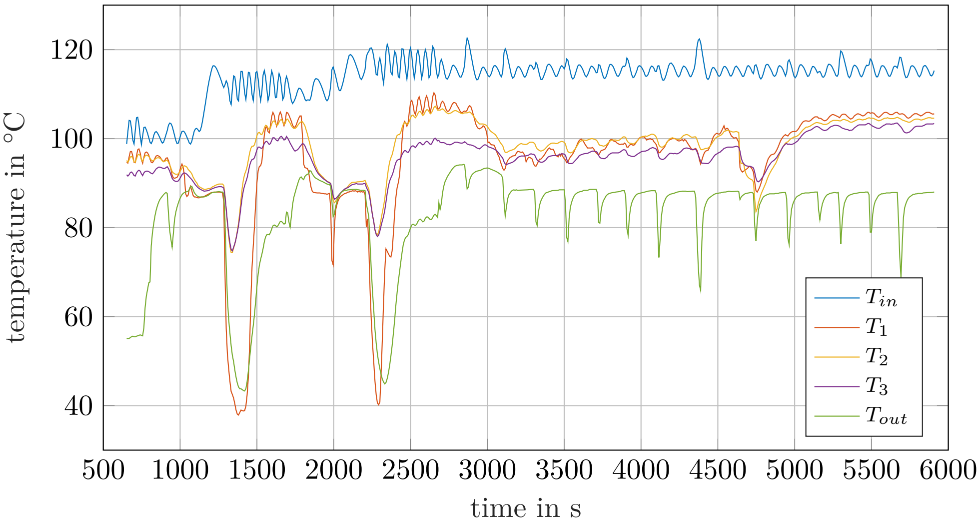

Figure 5.12: Influence of steam on temperature, Ghidini steam generator

temperatures rise again. The whole process is repeated ,with the difference, that at second 2000, steam production is lowered (because the steam generator draws water), resulting in a temperature drop. This should again clarify, that unsteady steam mass flow rate is an important factor in the stability of the system.

At second 3000, T_{in} is chosen high enough for temperatures to stabilize at just below 100 °C. T_{out} clearly indicates when the steam generator is drawing water. While the interval is at 1000 s with the Condair steam generator, intervals are reduced to about 200 s with the Ghidini steam generator. This is unfortunate and does not contribute to the goal of constant operating conditions.

At about 4600 s on the time axis, sand is filled into the reactor. After an initial drop due to sensible heating, temperatures stabilize at 5 °C above the initial level. Sand is an inert material and therefore no reasonable explanation can be found. Somehow, adding material reduces heat losses across the distributor plate. Also, the system's inertia is increased – temperature fluctuations are reduced.

Fig. 5.13 shows temperature curves for fine material at 0.6 bar and 100 °C. Here, T_3 does not drop to condensation temperature. A different problem, however, arises here. T_1 keeps falling below the intended temperature level. As a countermeasure T_{in} is increased again. However, because of the low fluidization velocity (and the low heat capacity flow of air), T_{in} only increases slowly. At roughly 7500 s fluidization velocity is increased. Only now temperatures rise to the intended level again. This behavior is especially problematic with fine material because of low mass flow rates of air. Condensation and unstable conditions before material is added, is a bigger issue than with coarse material. This effect is more problematic with the Ghidini steam generator, because fluctuations in steam mass flow rate are more distinct, resulting in more unstable conditions.

The other five temperature curves of hydration experiments are depicted in the appendix (Figs. A.1.1 - A.1.5). Especially hydration of MgO(2) fine at 0.4 bar and 80 °C (Fig. A.1.2) shows very unstable conditions before material is added. This is also the only material, which shows clumping of material on the reactor wall, similar to Fig. 5.11c.

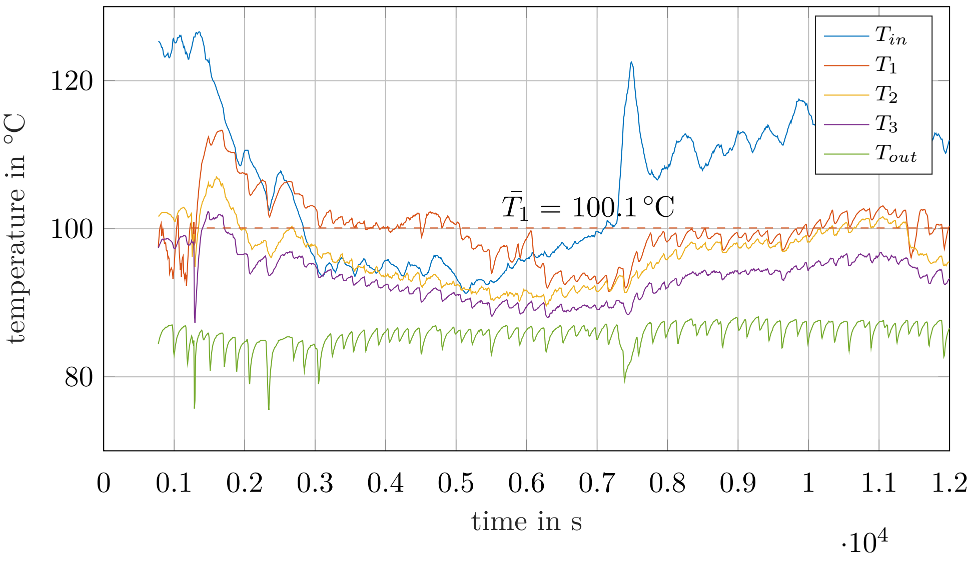

Figure 5.13: Temperature curves of hydration reaction at 0.6 bar and 100 °C, MgO(2) fine

5.4 Dehydration

Dehydration constitutes the charging reaction of the TCES process. (Waste) heat is utilized to decompose magnesium hydroxide into magnesium oxide according to the endothermic chemical reaction

$$Mg(OH)_{2(s)} \longrightarrow MgO_{(s)} + H_2O_{(g)} \tag{5.7}$$

The theoretical amount of heat needed is, of course, the same as for the hydration reaction. Per kilogram of $Mg(OH)_2$ this amounts to $\Delta H_R = 1393.3\,\frac{kJ}{kg}$ at standard conditions. For a mean dehydration temperature of 350 °C values change to $\Delta H_R = 76.46\,\frac{kJ}{mol}$ or $\Delta H_R = 1311.5\,\frac{kJ}{kg}$ per kilogram of magnesium hydroxide.

Dehydration is found to be a nucleation process with oxide lamella formation at the cost of the parent $Mg(OH)_2$ on an atomic level. Dehydration is also accompanied by a large volume decrease of about 50 % [43]. The overall particle size and the idiomorphic shape of the $Mg(OH)_2$ crystals are, however, preserved during heat treatment, implying that a highly porous structure is formed[46]. The highly porous structure is most likely evenly distributed over the entire particle volume. Nanostructured MgO crystals grow as pseudomorphs within the parent $Mg(OH)_2$ platelet [46, 43]. These small crystals on a nanometer scale result in high SSA. Pimminger et al. [46] achieves a maximum surface area of 317 $\frac{m^2}{g}$ after heat treatment at 350 °C for 2.5 h. Temperatures of dehydration influence specific particle surface areas. Higher temperatures diminish surface areas due to sintering of nanostructured MgO [54] and hamper reaction rates for the consecutive hydration reaction.

Experimental parameters are, in this case, reduced to reaction temperature and holding time. Steam partial pressure adjusts according to equilibrium pressure and kinetics. Again, 400 g of $Mg(OH)_2$ is used and fluidization velocities are tried to be kept at the same level as for hydration. As already mentioned minimum fluidization velocity changes with temperature – these deviations, however, are neglected. The procedure is the same as with hydration experiments. The reactor is preheated to the required level before material is added through the funnel. This ensures reproducible experiments. If the reactor is heated with material already inside, the reaction would start before the target temperature is reached, making the assumption of an isothermal reaction invalid.

5.4.1 First setup

For dehydration high temperatures, roughly between 300 °C to 400 °C, are necessary. A first experiment reveals high heat losses, as already expected from findings in the hydration section. Losses approximately increase linear with temperature. In order to achieve 340 °C at T_1, T_{in} is heated to 420 °C at a fluidization velocity of 0.48 $\frac{\mathrm{m}}{\mathrm{s}}$. This value is much higher than intended, but is unavoidable in order to reach this temperature level. In order to reach equilibrium (i. e. all temperatures are constant) at least 2 h are necessary. Even then, there is a temperature gradient of 60 °C between T_{in} and T_1 and 100 °C between T_{in} and T_3! Since the plant is only designed for a temperature of 400 °C, further increase is not advisable. Together with the fact that fluidization velocities are too high, this setup is deemed unsuitable for the intended investigations. Reactor heater H-2 is installed to improve the situation.

5.4.2 Second setup

Experiments are carried out in order to find correlation between conversion, reaction time, reaction temperature and SSA. Because of high reactor temperatures no samples can be taken during experiments. Only after completion and a sufficient long cooling time, the reactor can be unmounted and material can be taken out for analysis. This makes it unpractical to conduct experiments, establishing a correlation between conversion and reaction time, because time requirement would increase dramatically. Thus, an experimental series is conducted, where reaction time is kept constant at 75 minutes and reaction temperatures are varied. Reaction temperature (T_1) curves for all four experiments are shown in Fig. 5.15b. As representative temperature for dehydration, not the arithmetic mean is chosen, but reaction end temperature[3]. Values are given in the graph. Temperature profile depicted for the reaction at 369 °C is characteristic for dehydration. Once material is added, temperature drops drastically, but also reestablishes after a short time to a certain (lower) level. This mainly constitutes sensible heat needed to heat up particles. The incline from second 800 s to 4500 s is an indication for reaction heat consumed by the endothermic process. Once reaction temperature climbs to the (almost) constant level at 4500 s reaction progress is considered to be close to zero. All other dehydration experiments confirm this behavior (not graphically displayed). Depicted experiments at 342 °C and 327 °C would show the same behavior, if they would have been allowed more time to react, i. e. reactions under these conditions are not complete (sample analysis confirms this)[4]. As confirmation, an experiment with a similar thermal mass of inert material (sand) is conducted. Temperature profile confirms the above made assumption. Only the effect of sensible heat can be seen with sand (Fig. 5.14).

Looking again at Fig. 5.15b also shows that reaction end temperatures differ from initial preheating temperatures. The cause for this is unknown, but makes clear that it is difficult to carry out experiments resulting in the same end temperature. Especially because identical preheating conditions can lead to different end temperatures.

---

[3] The temperature at the end of the experiment.

[4] Reaction kinetics at 308 °C are too slow in order to affect the temperature curve.

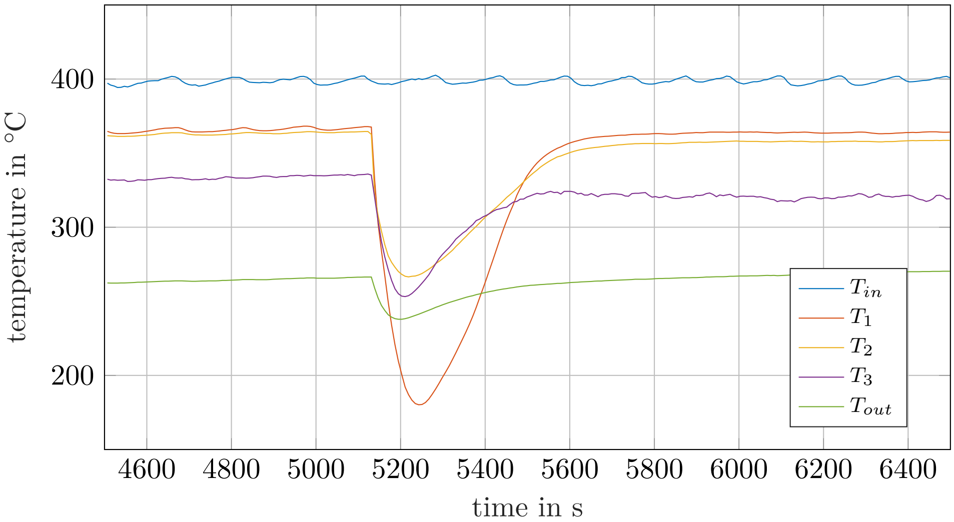

Figure 5.14: Validation of temperature profiles for dehydration with sand as inert material

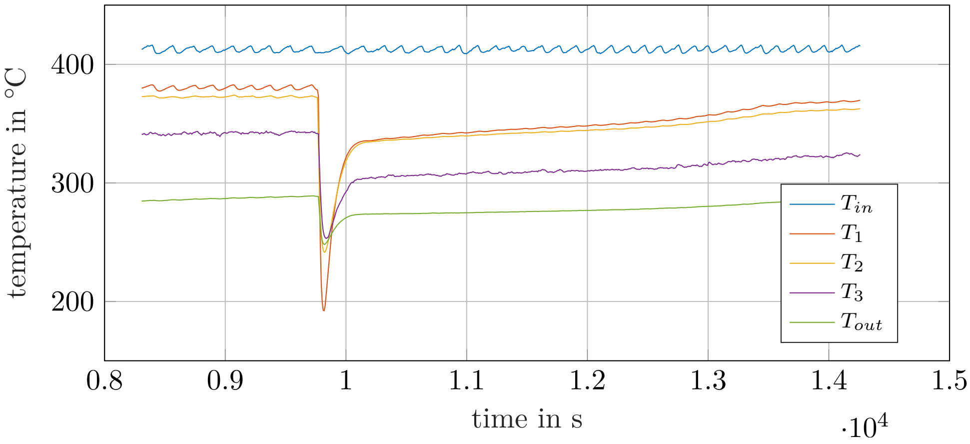

(a)

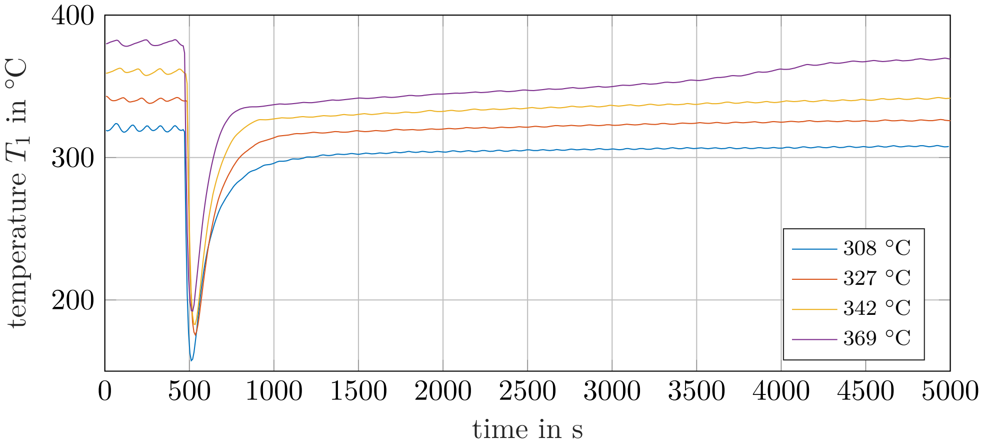

(b)

Figure 5.15: (a) Temperature curves for dehydration at 369 °C and (b) T_1-curves for dehydration at different temperatures for 75 minutes

In Fig. 5.15a all measured temperatures for the reaction at 369 °C are depicted. Reduction in temperature loss compared to the first setup is clearly visible. Especially T_1 and T_2 are almost on the same (higher) level.

Some other experiments, applying the same experimental procedure, are conducted, varying reaction temperatures and/or reaction time. The goal is to determine maximum conversion for a certain temperature and evaluate its SSA. Also, some experiments are conducted, where dehydration temperature is tried to be kept constant but reaction time is varied. Some relevant experiments are presented below, together with results.

5.5 Cycle experiments

A full cycle consists of the hydration reaction followed by dehydration or vice versa, depending on the initial material. For application in TCES, materials need to be stable over a large number of consecutive cycles. On one hand, the term stability refers to mechanical stability. Under cold flow conditions and for single reactions, this was already analyzed. However, it is possible, that long term stress results in changing particle sizes. Remember, that both hydration and dehydration are associated with large volume expansion and contraction, respectively. This intraparticle stress can cause fracture over time. On the other hand stability also refers to reversibility of the reaction. Under the same hydration/dehydration conditions, the final conversion could be reduced with every consecutive cycle. Furthermore, reaction rates might decrease over time. The last two points would diminish storage capacity, as well as storage power and round-trip efficiency.

First, nomenclature needs to be clarified. In this section it is not expedient to simply talk about magnesium oxide or magnesium hydroxide. The important factor is the initial material used for cycle experiments. Therefore, distinction between carbonate-based $MgO/Mg(OH)_2$ and hydroxide-based $MgO/Mg(OH)_2$ is made.

With regard to experimental procedure, a few points have to be considered. During hydration or dehydration particles sizes are not changing (at least not for single reactions). Thus, particle densities have to change. Both factors influence minimal fluidization velocities. The difference is, however, neglected and fluidization velocities are chosen according to values found in the cold flow experiments section for hydroxide-based and carbonate-based material. Another factor are heating and cooling phases. There are two ways to conduct the experiment. The reactor can be preheated to reaction conditions before material is added, just as it is done with hydration/dehydration experiments. This provides the advantage of comparability to previous experiments. However, one cycle experiment takes a long time, limiting maximum cycles achievable within a reasonable amount of time. Also, this procedure allows more samples to be taken (e. g. for Mastersizer analysis). The other possibility allows reduction of cycle time, because material is left within the reactor and no mounting/unmounting is necessary. Additionally, dehydration time reduces because reaction already starts during the heating phase. However, no experience has been collected on how this affects necessary dehydration times. Also, only small amounts of material can be taken out of the reactor for analysis (Mastersizer analysis after every cycle is not possible). The latter, however, also brings the advantage of nearly constant material inventory and therefore bed height. Both approaches are considered.

Parameters for hydration are again steam partial pressure and mean reaction temperature. Here, 80 °C and 0.4 bar are chosen, because previous results show high conversion. As materials MgO(2) coarse and $Mg(OH)_2$ coarse are chosen because the reactor is easier to control with them. For dehydration relevant parameters are reaction end temperature and reaction time.

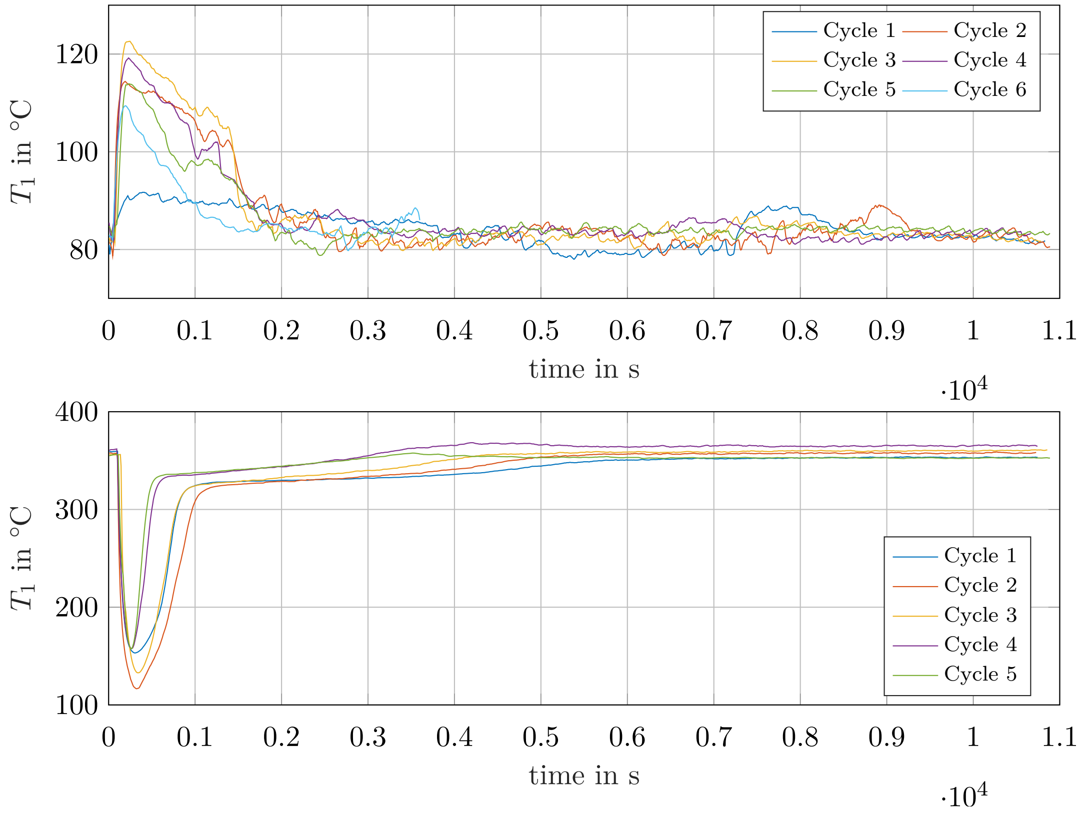

Figure 5.16: Temperature curves of cycle experiments with carbonate-based MgO(2) coarse, material removed after every reaction

Fig. 5.16 depicts T_1-temperature curves of hydration (above) and dehydration (below) for carbonate-based material. In this case, the reactor is preheated without material. 400 g of material is added at second zero on the graph. Duration of the reaction is set to 3 h again. Fluidization velocity is $0.33\,\frac{\mathrm{m}}{\mathrm{s}}$ for both reactions. Due to higher temperatures, fluidization number is theoretically higher at dehydration. Control of temperature T_{in} is the same at every cycle. Once the hydration reaction starts, temperature T_{in} is lowered to 80 °C, until reaction rates decrease and T_{in} has to be increased again. Here, small deviations in controlling T_{in} are unavoidable. T_{mantle} is always set to the same value as T_1. For dehydration T_1 and T_{mantle} are set to 400 °C.

Some interesting deductions can be made from Fig. 5.16. The first hydration cycle shows a temperature profile as expected, with a maximum at about 90 °C. Initial temperature is reached after roughly 4000 s. Every consecutive hydration reaction shows temperature surges much higher in comparison. Decline to initial temperatures is also faster. Both observations indicate faster kinetics. However, temperature curves are not representative for conversion and sequencing cycles (in particular cycles 2 to 6) according to this, can easily lead to misinterpretation (cf. section 6.1.2). Misinterpretation can be caused by the fact, that the material inventory of the reactor decreases with every consecutive cycle (because of sampling). For the 6th cycle only 200 g of material is available. Temperature profiles of dehydration also differ from cycle to cycle. This can also be an indication for faster kinetics but less material would show the same influence. Again reaction end temperatures differ, even though T_{in} and T_{mantle} are always set to the same level. This is problematic and can affect reaction rates of the successive cycle. Hence, reaction end temperatures for this and all following cycle experiments are given in Table 5.5.

Table 5.5: Dehydration end temperatures of cycle experiments

	$T_{1,end}$ in °C			
	Fig. 5.16	Fig. A.2.1	Fig. 5.17	Fig. 5.19
Cycle 1	353	355	351	341
Cycle 2	358	350	348	341
Cycle 3	360		350	341
Cycle 4	365			343
Cycle 5	353			341
Cycle 6				343
Cycle 7				342
Cycle 8				341

As was described in the section about dehydration, temperature profiles are characteristic for the reaction. A cycle procedure is therefore applied, where dehydration reaction is stopped once temperature gradients are minimal (meaning that temperature is not changing more than 1 °C within several minutes). Other parameters are identical. Temperature curves are given in the appendix (Fig. A.2.1). Interesting is, that again the third cycle shows the highest surge in temperature, not the second one.

Fig. 5.17 depicts cycle experiments with hydroxide-based material. For hydration, fluidization velocity is chosen at $0.2\,\frac{\mathrm{m}}{\mathrm{s}}$ in order to be consistent with the definition made for u_{mf}. Dehydration is carried out at $0.33\,\frac{\mathrm{m}}{\mathrm{s}}$, because establishment of equilibrium temperature takes a very long time at lower velocities.
In principle, temperature profiles are similar to carbonate-based cycle experiments, except that already the first hydration reaction shows temperature gains similar to consecutive cycles. Temperatures do not rise as high but stay on an elevated level about 1000 s longer compared to the first cycle with carbonate-based material in Fig. 5.16.
Cycle experiments are subject to condensation in the funnel as well and materials are more or less wet after hydration. Fig. 5.18 shows hydroxide-based material after the first hydration reaction. Here in particular, a lot of material is wet and does not fluidize any more. Channels are forming and material is inhibited (except for the reaction with water). This affects consecutive cycles, because water has to evaporate first (the more pronounced temperature decrease with the second dehydration is believed to be an indicator for this). Also, it can have an influence on crystal structure and conversion. For evaluation, samples are always taken from dry material.

For one cycle at least 9 h are needed. As was already mentioned above, a different approach is tried. Starting again with carbonate-based MgO(2) coarse, only the first hydration reaction is carried out for 3 h. Subsequent hydration reactions are carried out for 30 min. Dehydration reactions only until temperature gradients are small (as above). Also, heating up to dehydration temperature is done with material inside and hydration is started right after T_1 has cooled down to 80 °C. Material is thus never removed from the reactor. Among other advantages (see above) this reduces cycle time by two thirds and it resolves the condensation issue. The latter has two reasons: Within the first 30 minutes temperatures increase because of the reaction.

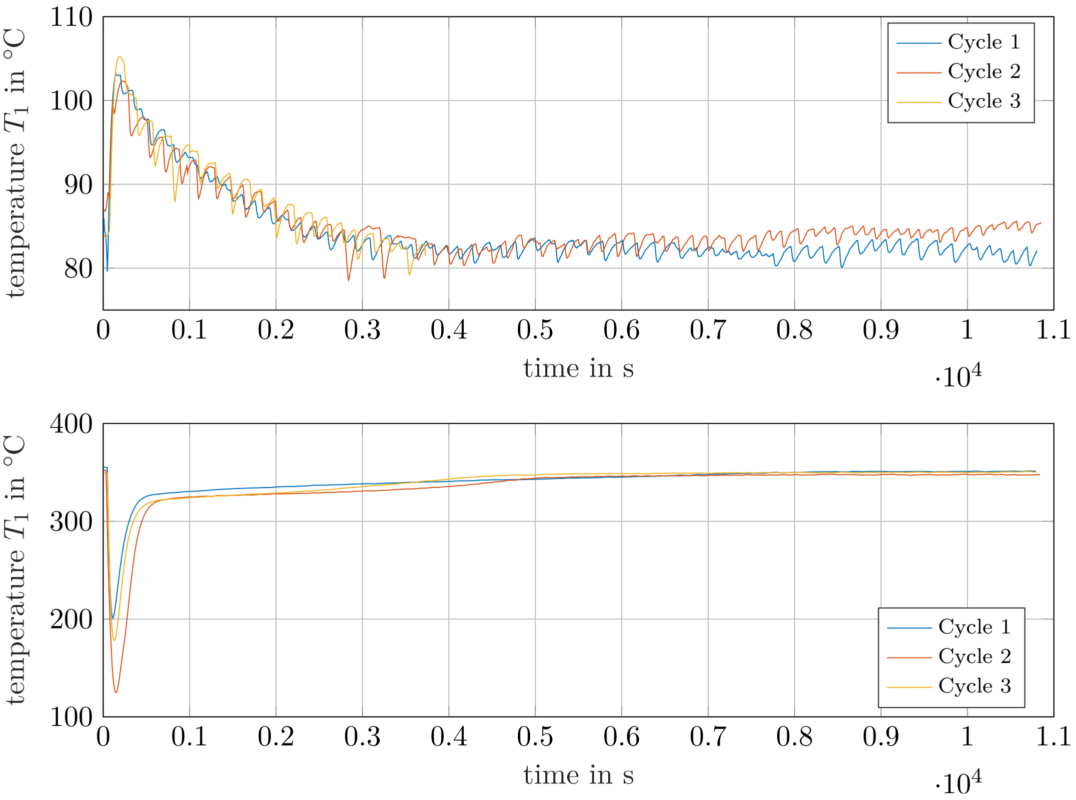

Figure 5.17: Temperature curves of cycle experiments with hydroxide-based $Mg(OH)_2$ coarse, material removed after every reaction

Figure 5.18: Coarse hydroxide-based material after first hydration

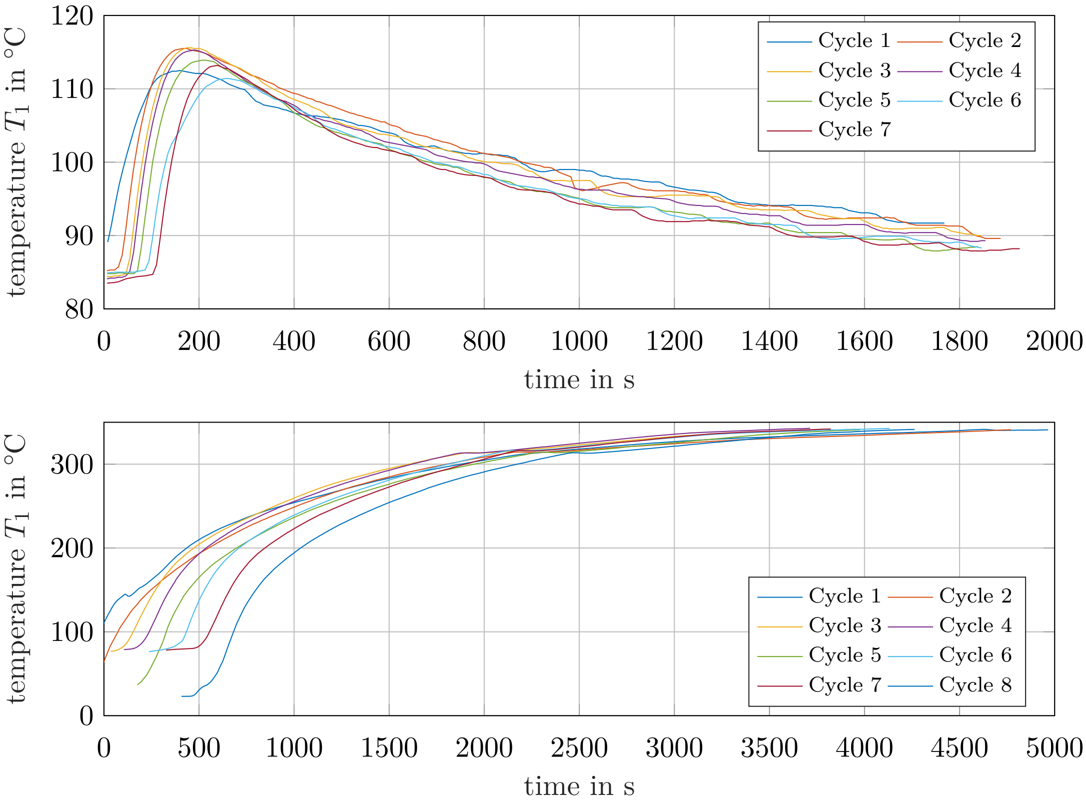

Figure 5.19: Temperature curves of cycle experiments with carbonate-based MgO(2) coarse, material stays in reactor

Condensation is only an issue, once temperatures fall back to initial levels. This is supported by the fact, that the (unheated) reactor wall temperature is still higher than in equilibrium because of the dehydration reaction carried out directly before.
T_{in} and T_{mantle} are set to 380 °C for dehydration. Fluidization velocity is set to 0.33 $\frac{\mathrm{m}}{\mathrm{s}}$ for hydration. Dehydration is, for the sake of speed, carried out at a constant mass flow rate of 22 $\frac{\mathrm{kg}}{\mathrm{h}}$. Superficial velocity is therefore varying and reaches a maximum of 0.56 $\frac{\mathrm{m}}{\mathrm{s}}$.
Fig. 5.19 depicts temperature curves. Note, that the graphs are displayed with a horizontal offset for better legibility. Dehydration temperatures would have still risen by 0.5 $\frac{°\mathrm{C}}{\mathrm{min}}$. It is therefore possible that complete conversion is not yet reached. However, the most important factor is, that cycles are identical. Reproducibility is at its maximum for these experiments. Dehydration temperatures are closely spaced and reaction time is always around 65 min (except for the first cycle with 80 min).

Liquid water is another option to carry out the hydration reaction. Because the first cycle seems to be slow, an experiment is conducted where carbonate-based material is preconditioned with liquid water. 1.5-times the stoichiometric amount of water (at ambient temperature) is poured in a beaker filled with MgO(2) coarse and mixed constantly. After a few minutes the reaction starts and temperatures start to rise (in the beginning reaction kinetics are slow, because temperatures are too low and water needs to be heated up first). Slightly over 100 °C are measured. Excessive water evaporates in this phase. Once the reaction is concluded, 3 hours of dehydration follow. The second cycle hydration is performed as always. The advantages and drawbacks of using liquid water were already discussed in section 3.2.1. It should only be said that this approach is simply used to ‘activate’ material in the first cycle and not to actually store/release thermal energy.

6 Evaluation

For evaluation, a few quantification methods are intended. First, methods for evaluation are described, then measurement methods are applied to experiments.

6.1 Methods

6.1.1 Humidity measurement

The oxygen probe measures humidity of air after it passes the fluidized bed (X_{out}). A humidity balance, including the theoretically calculated value at reactor entry (X_{in}), would constitute an online continuous measurement method for conversion.
Integral over the water balance:

$$n_{\mathrm{H_2O}}(t) = \frac{1}{M_{\mathrm{H_2O}}} \int\limits_{t_0}^{t} \dot{m}_a(\tau)\,(X_{in}(\tau) - X_{out}(\tau))\,\mathrm{d}\tau \tag{6.1}$$

Where $n_{\mathrm{H_2O}}(t)$ is the desired molar amount of water reacted. Since stoichiometric coefficients are all equal to one, it equals the reacted amount of MgO ($n_{\mathrm{H_2O}}(t) = n_{\mathrm{MgO}}(t)$). Conversion can thus be written as

$$\alpha(t) = \frac{n_{\mathrm{MgO},0} - n_{\mathrm{MgO}}(t)}{n_{\mathrm{MgO},0}}. \tag{6.2}$$

Unfortunately, when material is added to the reactor, no difference in water loading is measurable whatsoever. Fig. 5.8 shows this quite distinctly. Material is added at 2400 s on the time axis, but no change in p_{out} is observed. All other conducted experiments show same behavior in this regard. The most obvious explanation is slow reaction kinetics. Anticipating a result (cf. Fig. 6.3) that is obtained later, theoretical change in $X_{\mathrm{H_2O}}$ and $p_{\mathrm{H_2O}}$ can be calculated. With sufficient approximation linear conversion of 50 % over a time span of 90 min can be assumed. $\dot{n}_{MgO}$ can be calculated by using Eq. 6.2. With an air mass flow rate of $\dot{m}_a = 14\,\frac{\mathrm{kg}}{\mathrm{h}}$, change in water loading is

$$\Delta X_{\mathrm{H_2O}} = \frac{\dot{n}_{\mathrm{MgO}} M_{\mathrm{H_2O}}}{\dot{m}_a} = 0.00425. \tag{6.3}$$

Expressed in molar amount and partial pressure this yields

$$\Delta x_{\mathrm{H_2O}} = 0.0026 \approx 0.0026\,\mathrm{bar}. \tag{6.4}$$

This change is below the accuracy limits of the oxygen sensor. Even if a drop in partial pressure would be seen, changes are to small for a quantitative evaluation of conversion. Especially if fluctuations due to unsteady steam production rates are taken into account, the signal would get lost in the noise.

Two other problems are found to be an issue with the oxygen probe measurement. As was already mentioned before, dust is able to enter the sensor, possibly altering results (and destroying the sensor in the long run). Also, ground fault seems to be an issue. If the sensor gets in contact with metallic parts of the test rig, measurement differs from values obtained when the sensor is insulated electrically. The offset in Fig. 5.8, before steam is actually added, could be caused by this effect. This is possible, because ground fault offset is constant, only if the probe is moved, values start to jump. Which effects (or none, or both) influence measurement cannot be determined. The issue with material entering the sensor was only just found, because the sensor was sent back to the manufacturer to fix the ground fault problem. It is, howsoever, clear that a sensor of this type should not be brought into contact with dust loaded air and therefore cannot be used in this application. Measurement after the filter could be a solution. In this case, however, filter temperatures during hydration are low and condensation occurs, falsifying results again.

As replacement for the oxygen sensor, humidity measurement is tried out. However, as already described above (cf. section 3.1.3), it is also unsuitable for use in this application.

6.1.2 Enthalpy balance

Another option for quantification is to perform an enthalpy balance with the reactor as the control volume boundary. The reactor wall, however, cannot be assumed to be adiabatic as the temperature curves show. Heat losses are too dominating and calculated reaction enthalpies would be positive for exothermic reactions.

T_1 reflects reaction temperature very well. An enthalpy balance just enclosing the bed material is a different approach. At the control volume entry a constant temperature is assumed ($T_{baseline}$ – this temperature is measured before material is added to the reactor, with the temperature sensor measuring T_1). The temperature level at control volume exit is also measured with the T_1 temperature sensor. This is possible because isothermal conditions within the bed and adiabatic boundary conditions towards the reactor wall is assumed. This value is a function of time. The released heat can then be calculated by simply taking the difference in temperature between control volume entry and exit. Numerical integration over time gives the reaction enthalpy at time t.

$$h_{baseline}(t) = X_{in}\left(h_{evap} + c_{p,s}T_{baseline}(t)\right) + c_{p,a}T_{baseline}(t) \tag{6.5}$$

$$h_1(t) = X_{in}\left(h_{evap} + c_{p,s}T_1(t)\right) + c_{p,a}T_1(t) \tag{6.6}$$

$$\Delta H_R = \int_{t_0}^{t} \dot{m}_a \left(h_1(\tau) - h_{baseline}(\tau)\right) \mathrm{d}\tau \tag{6.7}$$

Where X_{in} is water loading at reactor inlet, h_{evap} enthalpy of evaporation, $\dot{m}_a$ air mass flow rate and c_p specific heat capacities of steam and air. Results, however, underestimate true values by far. For the experiment according to Fig. A.1.1 calculation yields a reaction enthalpy of $\Delta H_R = -75\,\mathrm{kJ}$ within the first 90 min, whereas the true value lies at $\Delta H_R = -389\,\mathrm{kJ}$ (It is calculated by using conversion determined by XRD further down). Many factors have an influence on the result. First, T_{in} is not kept constant. Secondly, heat losses of unknown magnitude reduce calculated values. Some attempts are made to include them, but none deliver correct values. Heat losses would have to be calculated very exactly in order to correlate measured reaction enthalpies to conversion. Another factor is, that the baseline temperature might be completely different if it is determined with (inert) material in the reactor (Fig. 5.12 shows this clearly).

6.1.3 Loss on ignition

An easily feasible way of measuring conversion offline is by loss on ignition. A weighed sample of reacted material is placed into a crucible and heated to a predefined temperature for a certain amount of time. Afterwards sample weight is measured again. Difference gives loss on ignition. This value can be used to calculate conversion. In the presented case 10 g of material is placed into a ceramic crucible and heated up to 450 °C in a muffle furnace for a holding time of 3 h. The mathematical procedure for calculation of conversion is explained shortly. Definition of conversion is given in Eq. 3.23. We have to find the molar amount of reacted MgO in relation to the initial amount of MgO. In the furnace, the reverse chemical reaction to Eq. 5.6 takes place. Water is released and evaporates, resulting in weight loss. This weight loss expressed in molar amount equals the molar amount of $Mg(OH)_2$ present in the probe since stoichiometric coefficients are one. The molar amount of $Mg(OH)_2$ then again has to match the molar amount of MgO reacted during hydration. The initial amount of MgO before the reaction is calculated by taking the 10 g of sample weight and subtract loss on ignition.

$$\alpha(t) = \frac{n_{\mathrm{MgO},0} - n_{\mathrm{MgO}}(t)}{n_{\mathrm{MgO},0}} = \frac{\frac{|m_{\mathrm{H_2O}}|}{M_{\mathrm{H_2O}}}}{\frac{10\,\mathrm{g} - |m_{\mathrm{H_2O}}|}{M_{\mathrm{MgO}}}} \tag{6.8}$$

Where $m_{\mathrm{H_2O}}$ is loss on ignition. All samples produced with the first setup are analyzed this way. Two problems arise using this method. As TGA reveals, temperature in the furnace is too high. Since material contains varying amounts of magnesium carbonate, decarbonization takes place to an undefined degree. Even if temperatures would be increased further, in order to achieve full decarbonization, varying carbonate contents would falsify results. Additionally, varying amounts of surface water are present, also influencing results. The only thinkable way to use this method would be, to keep temperatures low enough, for carbonate to stay inert and dry samples before weighing, in order to remove surface water. If carbonate share is determined once by TGA, its influence on conversion can be mathematically subtracted (only if carbonate contents is constant). Nevertheless, because of its inaccuracy, this method of evaluation is not further pursued.

6.1.4 TGA & PXRD

Thermogravimetric analysis (TGA) and powder diffraction (PXRD) are used to determine sample composition offline. The TGA principle is simple. A few milligrams of sample material is placed on a highly sensitive scale which is located in a furnace. The sample is heated at a constant temperature rate and mass loss is measured meanwhile. As a result, temperature is plotted versus percentage mass loss (of initial mass). Since reaction temperature is characteristic for a certain reaction, mass loss can be assigned accordingly. This, of course, only works if all possible reactions which could occur are known and multiple reactions occurring at same temperature levels are not present. Besides minor impurities, this should be the case for available materials. Three steps have to be distinguished. Mass loss due to surface adsorbed water

up to 200 °C, dehydration reaction of $Mg(OH)_2$ to MgO up to 400 °C and decarbonization of residual $MgCO_3$ to magnesium oxide up to 1000 °C.
The in this way acquired temperature - mass loss curves are evaluated and conversion as well as composition of the samples is calculated. Calculation method is similar to the one presented for loss on ignition, because its based on the same principle. First, percentage mass losses are transformed into mass shares of the sample.

$$\begin{aligned} w_{\mathrm{H_2O}} &= \Delta m_{\mathrm{H_2O}} \\ w_{\mathrm{Mg(OH)_2}} &= \frac{\Delta m_{\mathrm{Mg(OH)_2}}}{M_{\mathrm{H_2O}}} * M_{\mathrm{Mg(OH)_2}} \\ w_{\mathrm{MgCO_3}} &= \frac{\Delta m_{\mathrm{MgCO_3}}}{M_{\mathrm{CO_2}}} * M_{\mathrm{MgCO_3}} \\ w_{\mathrm{MgO}} &= 1 - w_{\mathrm{H_2O}} - w_{\mathrm{Mg(OH)_2}} - w_{\mathrm{MgCO_3}} \end{aligned} \tag{6.9}$$

Where Δm_i is the mass loss. This can be transformed into molar shares.

$$x_i = \frac{\frac{w_i}{M_i}}{\sum_i \frac{w_i}{M_i}} \tag{6.10}$$

Now, conversion can be calculated easily.

$$\begin{aligned} \alpha_{\mathrm{MgO}} &= \frac{x_{\mathrm{Mg(OH)_2}}}{x_{\mathrm{Mg(OH)_2}} + x_{\mathrm{MgO}}} \\ \alpha_{\mathrm{Mg(OH)_2}} &= \frac{x_{\mathrm{MgO}}}{x_{\mathrm{Mg(OH)_2}} + x_{\mathrm{MgO}}} \end{aligned} \tag{6.11}$$

PXRD utilizes the fact, that atoms of the sample diffract X-ray waves to a certain degree. Diffraction angles are characteristic for elements. Mathematical methods in combination with a database then allows calculation of powder composition. Samples have to be ground before analysis. Calculation of conversion is identical to TGA. Note, that residual carbonate and surface water cannot be detected in this particular case.

6.1.5 BET

The specific surface area of particles is an important quantity for gas-solid reactions and is in direct correlation to reaction rates. SSA is determined by measuring gas adsorption on particles and calculating the surface area, using the BET-method. For further information see literature.

6.1.6 Particle size analyzer

The Mastersizer 2000 (Malvern Instruments) performs this task in a wide range – from 0.02 µm to 2000 µm – detecting scattering of light when particles are passed through a laser beam. Mathematical models then calculate the particle size distribution. For measurement of MgO/$Mg(OH)_2$ this method works well.

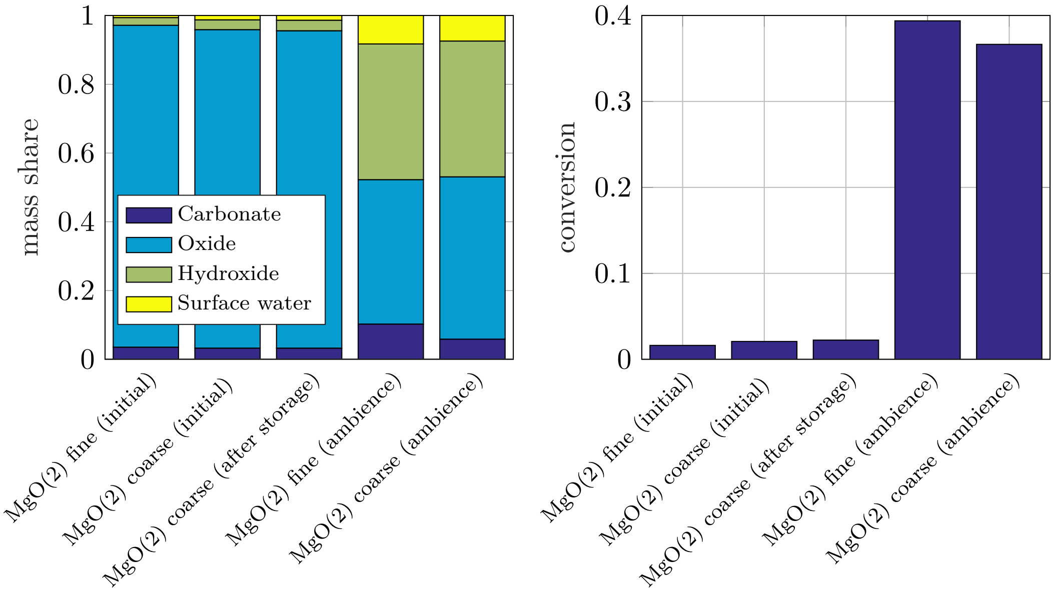

Figure 6.1: Molar share and conversion for MgO(2) fine and coarse during storage in closable containers and storage under ambient conditions

6.2 Storage

MgO is stored in closable containers. Both fractions of MgO(1) show only minor conversion during the storage period (about 3 months, see Fig. 6.2). For MgO(2) again some samples are taken to determine conversion during storage. Fig. 6.1 shows results for initial material (at the time experimentation was started). 'After storage' represents MgO(2) coarse after a storage period of about 3 months, in a regularly opened, but closable container. 'Ambience' stands for material stored directly under ambient conditions. Samples are also taken after about 3 months. Conversion already advanced about 35 % to 40 % and surface water contents rise to 8.3 $w\%$ (20 $mol\%$) and 7.4 $w\%$ (17.7 $mol\%$), respectively. Results make clear, that storage in a water free environment is necessary if stored energy is not to be released prematurely.

6.3 Hydration

6.3.1 First setup

For the first setup only TGA on some samples, according to Fig. 6.2, is performed.

Results are given for both initial MgO(1) fractions, for initial $Mg(OH)_2$, for the magnesite used in production of magensium oxide and for hydrated samples. The implications, considering initial material, are discussed in the section above.

The magnesite consists of almost only magnesium carbonate. The hydroxide contains other substances to some extent. 5.9 $w\%$ of magnesium oxide, 1 $w\%$ of surface water and 6.7 $w\%$ of carbonate are present.

As was already mentioned, materials show varying amounts of carbonate, most likely originating from non-uniform burning conditions in the top-hat oven. Especially the fine fraction has a high carbonate share of 10 $w\%$ to 19 $w\%$. Coarse fraction shows 4.6 $w\%$ to 11.5 $w\%$. Hydrated

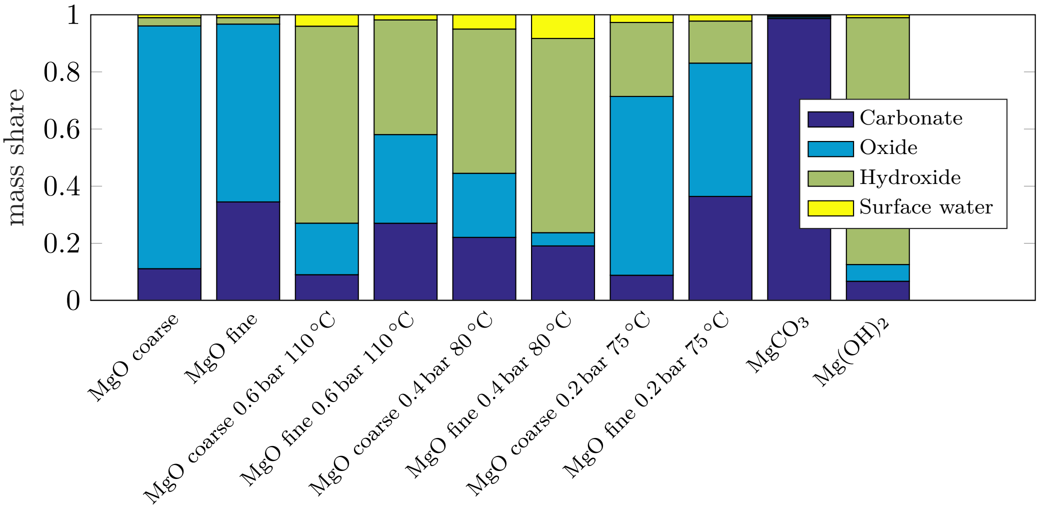

(a) molar share

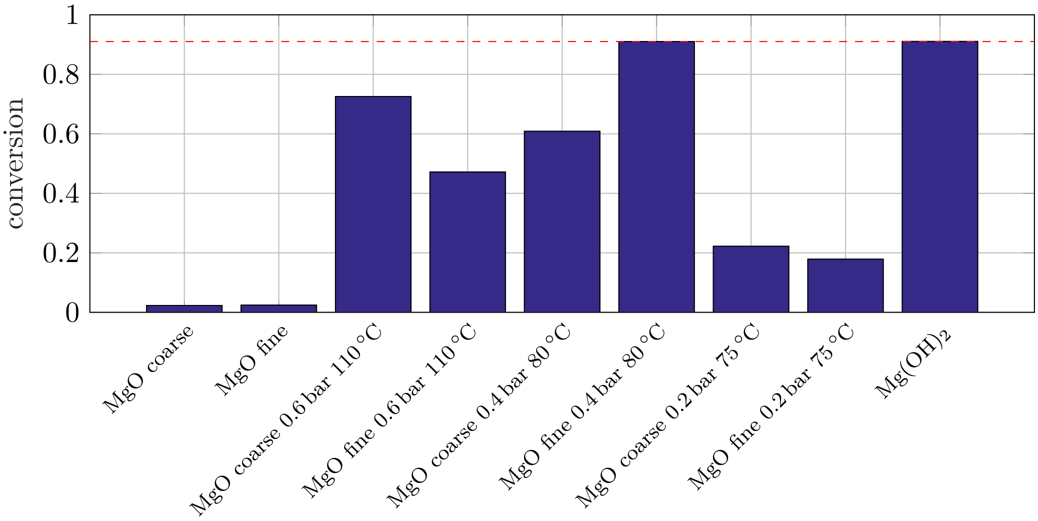

(b) conversion

Figure 6.2: TGA results of MgO(1) hydration

samples also show elevated surface water contents. It seems, not the whole amount of steam is able to react, but remains adsorbed on the particle surface. Additionally, water condensation in the region above the bed is an issue. Wet clumps are forming, resulting in increased water content. This was already described above. The MgO(1) fine sample at 0.4 bar and 80 °C shows especially high surface water contents at 8.3 $w\%$ (23.4 $mol\%$). As long as water is available, the reaction might proceed to an unknown degree. The implication must thus be, that conversion given in Fig. 6.2b, is not only determined by the controlled reaction in the reactor, but also a function of the water-reaction occurring afterwards. As substantiation, surface water content seems to correlate with conversion. Of course, different parameter settings also influence conversion. To what degree, can unfortunately not be interpreted from the graph. Also the effect of different particle sizes is not consistent, but varies strongly.

The dashed red line is added to display maximum conversion at 91 %. The exact production process of magnesium hydroxide is not known, but full conversion is not reached. That the hydrated sample of MgO(1) fine at 0.4 bar and 80 °C show same conversion can be coincidence, but could also mean that the remaining MgO is inhibited. Since only TG analysis is performed, the actual composition of the material is not known. From Eq. 6.9 it can be taken, that the mass share of magnesium oxide is calculated by subtracting every other known component. This, however, implies, that the rest really consists of oxide. If (stable) impurities are present, conversion is actually higher.

As a conclusion of the hydration of MgO(1) it is summarized, that no statement on kinetics can be made.

6.3.2 Second setup

Fig. 6.3 gives conversion-time curves for hydration experiments with MgO(2). Every data point represents a XRD measurement. Clearly, the influence of different parameters can be deduced. At 0.4 bar and 100 °C, conversion stays below 20 % for both fractions. The final conversion is already reached within the first 30 to 60 minutes. Longer holding time does not show any influence. This is in accordance with only minimal temperature increases presented earlier. In this case, distance to the equilibrium curve is too little for the material to show desired reaction rates. Increasing partial pressure to 0.6 bar or lowering temperature to 80 °C increases conversion significantly. Both effects influence conversion by approximately the same amount. Additionally, different particle size fractions do not show significant influence on conversion. This confirms the theory, that different particle sizes only have minor influence on reactivity. As already mentioned, SSA is directly linked to the reactivity of the material. Highly porous particles show large inner surface areas. Contribution of the outer surface area is negligible. In Table 5.1 both fraction are assigned the same SSA value, even though measurement is only performed on the coarse fraction (according to the manufacturer, this is a valid assumption).

For same hydration experiments Fig. 6.4 depicts TGA results. In Fig. 6.4a the mass-based composition is given. Compared to MgO(1), carbonate contents is more uniform (3 $w\%$ to 6 $w\%$ for MgO(2) coarse and 3 $w\%$ to 3.5 $w\%$ for the fine fraction). Again, hydrated samples show elevated water contents. Note, that samples were taken from macroscopic dry material. Data also shows, that carbonate contents seem to increase allegedly for hydrated samples. $MgCO_3$ should, however, not change during the reaction. This implicates, that TGA evaluation is not unambiguous to a certain degree. Remember, that evaluation is performed by taking the mass loss between 400 °C and 1000 °C. It is possible, that other unknown reactions occur. Three possible explanations are found. According to McKelvy et al. [43], surface water can actually

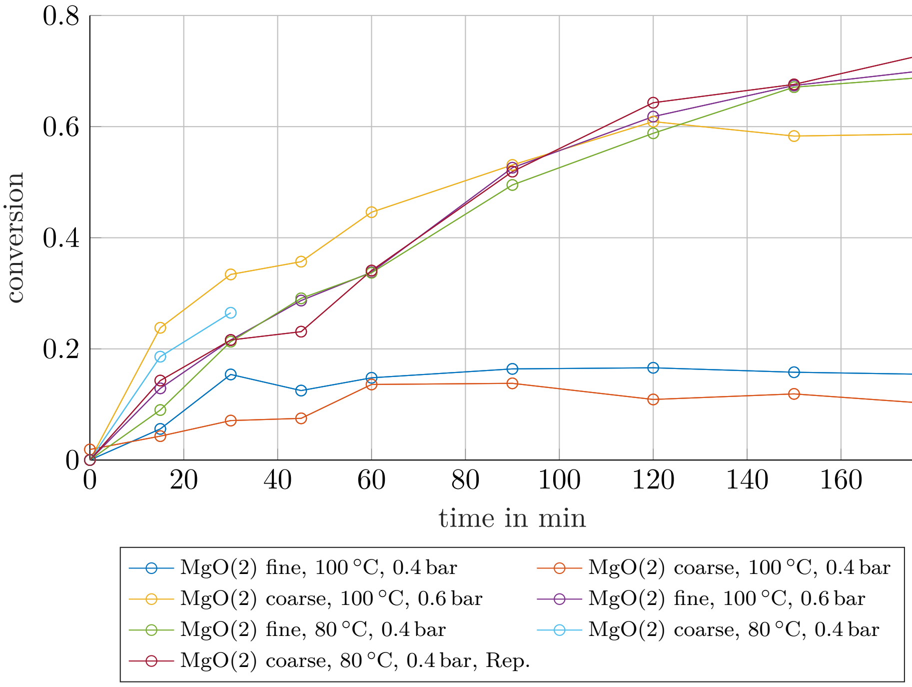

Figure 6.3: Conversion over time for different hydration parameters, XRD results

be retained up to 550 °C. Furthermore, CaO is present, which could have reacted to $Ca(OH)_2$. Dehydration temperatures of the latter would be within this range. An explanation, which would actually support an increase in carbonate content, assumes the formation of magnesium hydroxy carbonate (e. g. $(MgCO_3)_4 \cdot Mg(OH)_2 \cdot 4\,H_2O$) by the reaction of dissolved carbon dioxide in water with MgO.

Fig. 6.4b depicts conversion obtained from TG measurements. Comparing XRD and TGA, validates the applicability of XRD analysis. An absolute deviation of 0.0205 with a standard deviation 0.0236 is calculated.

Analysis of particle size distribution of hydrated samples reveal, that no change in particle size occurs during the reaction. Only the dust fraction is reduced again. Data also indicates, that the amount of dust carried out correlates with conversion. The higher conversion, the less dust is present.

6.4 Dehydration

The difficulty in evaluating dehydration experiments is given by the fact that no samples can be taken during the reaction. To generate sufficient data in order to correlate conversion and reaction time at different dehydration temperatures (similar to curves presented in Fig. 6.3 for the hydration reaction), would require too much time. Therefore only one data series is presented in Fig. 6.5, where conversion and SSA as a function of temperature at constant reaction time are shown. Additionally, associated Mastersizer curves are given.

Results show an substantial increase in conversion with higher temperatures. At 369 °C 100 % conversion is reached. In this case, XRD evaluation is applied. TG analysis on a sample with 100 % conversion according to XRD, shows lower conversion (90 %). Two possibilities come

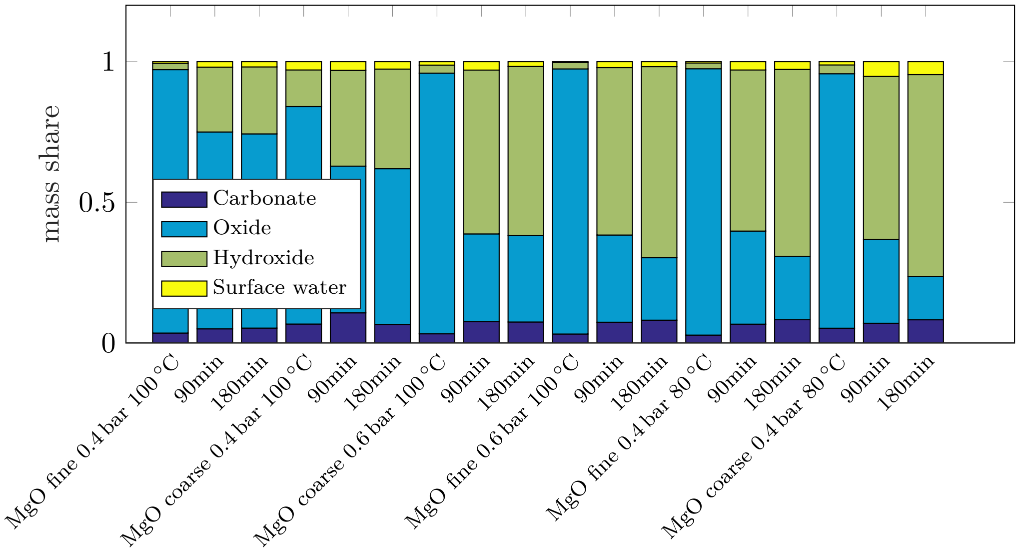

(a) molar share

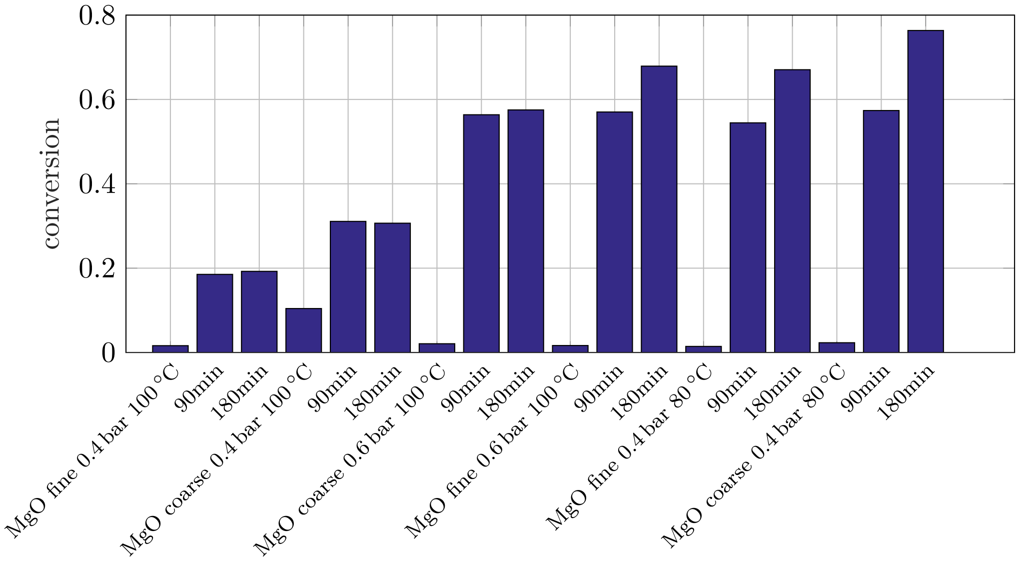

(b) conversion

Figure 6.4: TGA results of MgO(2) hydration

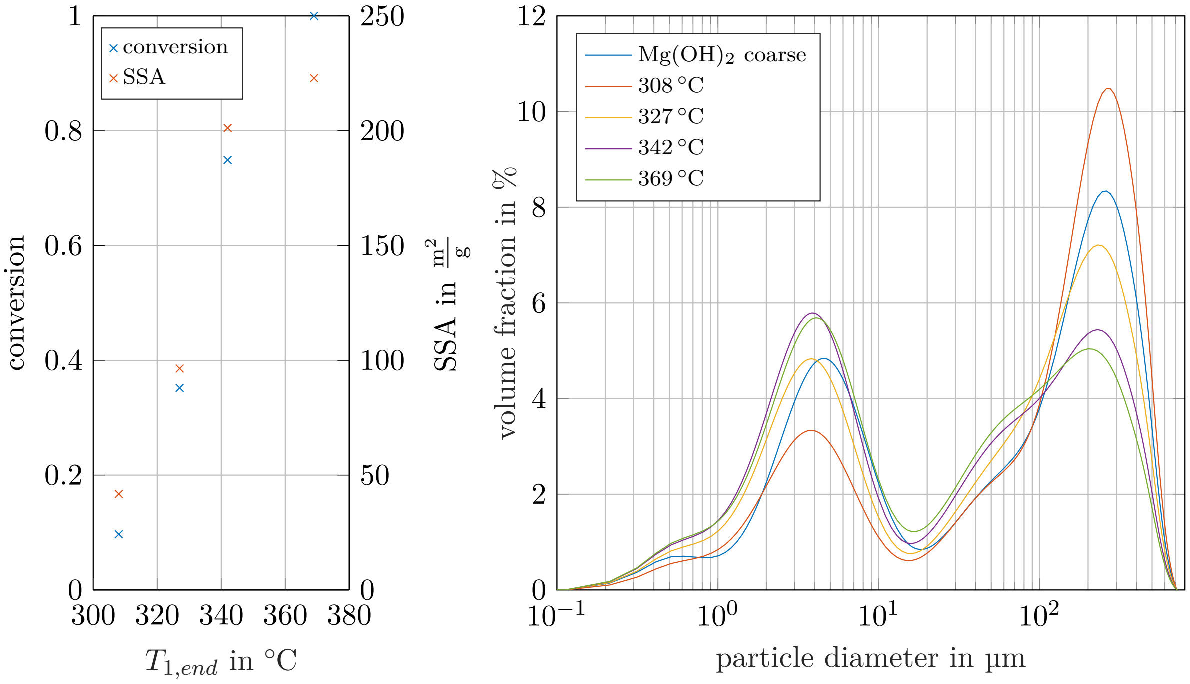

Figure 6.5: Conversion, SSA and particle size distribution of $Mg(OH)_2$ coarse after dehydration at different temperatures and constant dehydration time

to mind. Either XRD measurements do not detect residual $Mg(OH)_2$ or the sample hydrated while in storage, since dehydrated material is highly reactive.

Results from BET analysis shows, that SSA almost linearly increases with conversion. Except for the value at 369 °C. It is believed, that the, by comparison, lower SSA results from high conversion and not from temperature effects. If the above mentioned XRD error is believed, SSA – conversion dependency can be interpreted as linear again. BET measurement itself is very reliable. Four measurements on initial material samples result in $27.46\,\frac{m^2}{g} \pm 0.43\,\frac{m^2}{g}$. This also shows, that SSA is increasing about eightfold after complete dehydration.

Mastersizer analysis reveals a change in particle size distribution after dehydration. While the reaction at 308 °C leads to a reduction in dust fraction, experiments at higher temperatures/ higher conversion, exhibit proportionately more dust and less main fraction material. Also, fragmentation is clearly visible, noticeable by the bulge between 20 µm and 100 µm.

Various other dehydration experiments are depicted in Table 6.1. According to XRD, 100 % conversion is obtained with all listed experiments. Number 1 and number 2 show time-series at more or less constant reaction end temperature. A distinct influence of reaction time and SSA can be deduced. Two possible explanations arise. Either SSA is a complex, non-monotonous function of time, or experimental procedure is not representative.

Number 3 and 4 repeat already depicted experiments. It is given, to illustrate influence of reaction end temperature on SSA at constant reaction time. Unfortunately results are not conclusive either. The two comparisons contradict each other.

Another statement concludes, that at 313 °C full conversion is not reachable (81 % after 17 h). Higher temperatures are necessary.

Table 6.1: Influence of reaction time and reaction end temperature on SSA

ID	reaction time in min	$T_{1,end}$ in °C	SSA in $\frac{m^2}{g}$
1	75	369	222.9
	150	364	174.02
	180	368	210.89
	210	362	276.5
2	180	351	301.43
	210	348	217.48
	400	353	255.50
3	210	348	217.48
	210	362	276.5
4	180	351	301.43
	180	368	210.89

6.5 Cycle experiments

First, to give an overview, a short summary of conducted cycle experiments is given. Hereinafter the numeration below is used to simplify allocation.

1. 6 Cycles with carbonate-based MgO(2) coarse with 3 hours of reaction time each. Material is taken out of the reactor after every reaction (cf. Figs. 5.16 & 6.6 & 6.7).
2. 3 Cycles with carbonate-based MgO(2) coarse with 3 hours for the hydration reaction and dehydration until T_1 is constant (short dehydration, cf. Figs. A.2.1 & 6.8).
3. 2 Cycles with carbonate-based MgO(2) coarse and water conditioning during the first cycle (cf. Fig. 6.8).
4. 8 Cycles with carbonate-based MgO(2) coarse with 3 hours for both reactions during the first cycle, but short consecutive cycles (30 min for hydration – dehydration until 340 °C is reached). Material is left in the reactor after the first cycle (cf. Figs. 5.19 & 6.9).
5. 3 Cycles with hydroxide-based $Mg(OH)_2$ coarse with 3 hours of reaction time each. Material is taken out of the reactor after every reaction (cf. Figs. 5.17 & 6.10).

Conversion calculated from XRD analysis for cycle experiment 1 is depicted in Fig. 6.6, associated particle size distributions in Fig. 6.7. As temperature profiles already suggested, reaction kinetics accelerate after the initial cycle. Reaction rates are especially high within the first 15 min. Conversion climbs to 40 % to 50 % within this time frame, equaling a mean conversion rate of $4.4 \times 10^{-4}\,s^{-1}$ to $5.5 \times 10^{-4}\,s^{-1}$. Afterwards the reaction slows down significantly. Final conversion is again similar to values found for hydration experiments. Results are not explicit, but data suggests a small decrease in conversion after every consecutive cycle (except for cycle 6 – at cycle 4 the reaction had to be interrupted after 20 minutes, hence the higher conversion). Note, that dehydration end temperatures also increase from cycle to cycle, which could influence results as well.

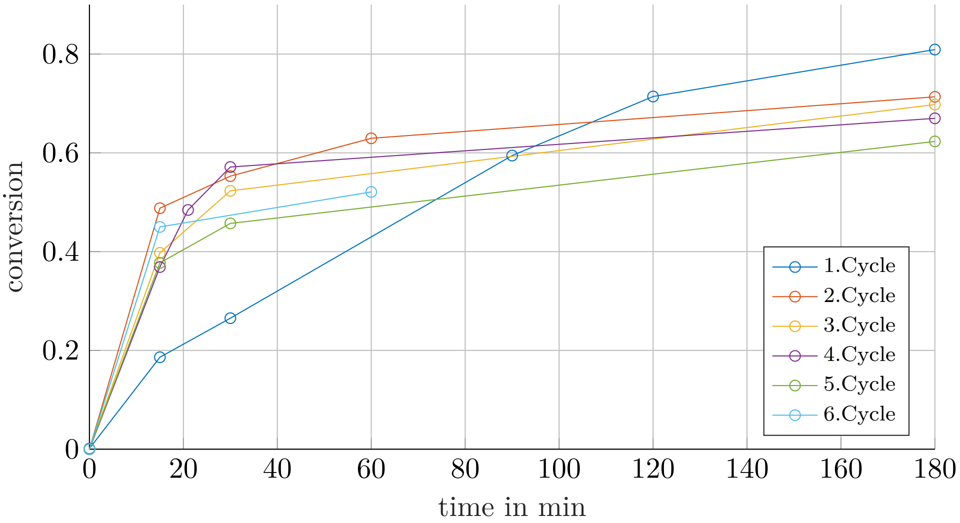

Figure 6.6: Cycle exp. 1: Conversion for carbonate-based MgO(2), 6 Cycles

Mastersizer curves show only minor alteration while cycling. Samples are taken from dehydrated material, except for cycle 6, where material is from an one hour hydrated sample. The dust fraction is again diminished with every consecutive cycle. Also, the mode-value slightly shifts to smaller values. Interesting is, that the peaks of the 4th and 5th cycles are lower, even though the dust fraction diminishes. This is possible because the variance increases marginally. The hydrated sample shows again a higher peak than the dehydrated sample from the previous cycle. Overall, it is safe to assume, that macroscopically no significant alteration occurs.

XRD results for cycle experiment 2 and 3 are depicted in Fig. 6.8. Even though the first cycle is always carried out under same conditions, results vary strongly. Since the first cycle hydration reaction is carried out 4 times, XRD results are compared. Within the first 30 min deviation is small. The longer the duration, the larger deviation is. This behavior has no apparent explanation. Results from consecutive cycles seem to fit quite well (for convenience this comparison is shown graphically in Fig. A.1.6). This is problematic, because the amount conversed during the first cycle influences the second cycle. Remember, that the dehydration reaction is responsible for the large increase in SSA. If only half the material is hydrated in the first step, the following dehydration process will not result in maximum surface area. XRD curves, however, show similar conversion rates than cycle experiment 1 (dashed lines are given for comparison). Two effects are therefore present, which are inseparable: Influence of the actually investigated shorter dehydration time and diminished conversion during first cycle hydration.

In order to save space, the second cycle hydration curve for cycle experiment 3 (water conditioning) is also shown in this graphics. On the right, the material's composition after water conditioning is shown. Besides elevated surface water contents, a conversion of about 83 % is reached. This is a good value and using liquid water is a feasible way for conditioning. Second cycle hydration, however, shows a lower conversion rate during the first 15 minutes. Change in particle size is not detected.

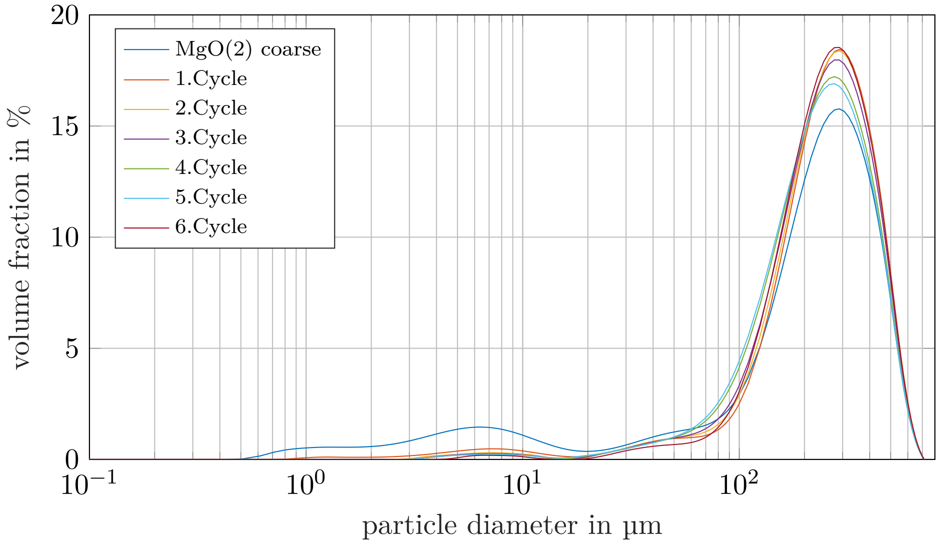

Figure 6.7: Cycle exp. 1: Particle size distribution for carbonate-based MgO(2), 6 Cycles

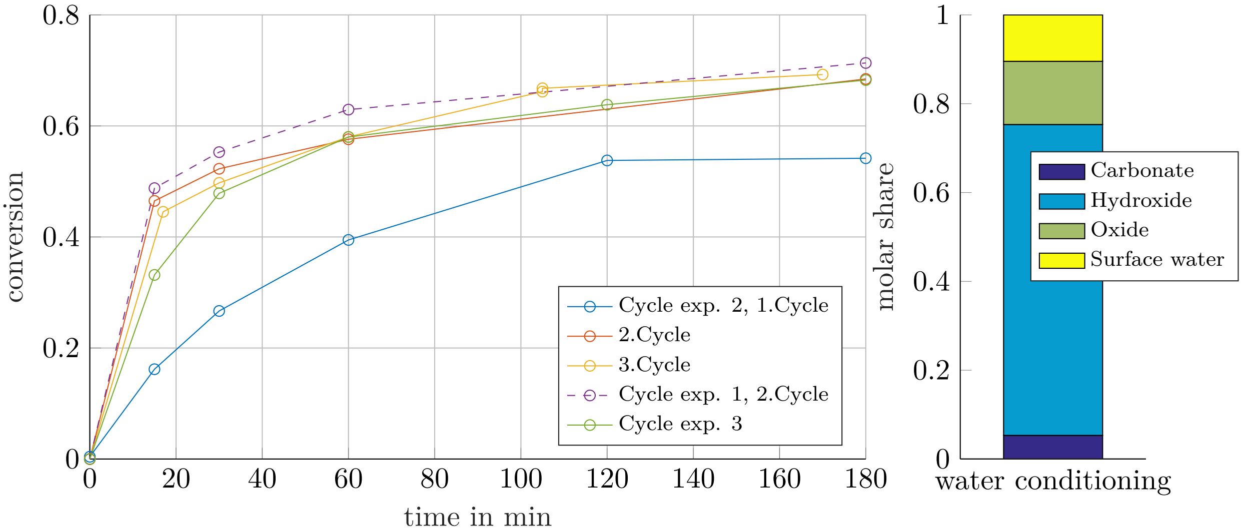

Figure 6.8: Cycle exp. 2 and 3: Conversion of carbonate-based MgO(2), 3 Cycles, shortened dehydration time and water conditioning

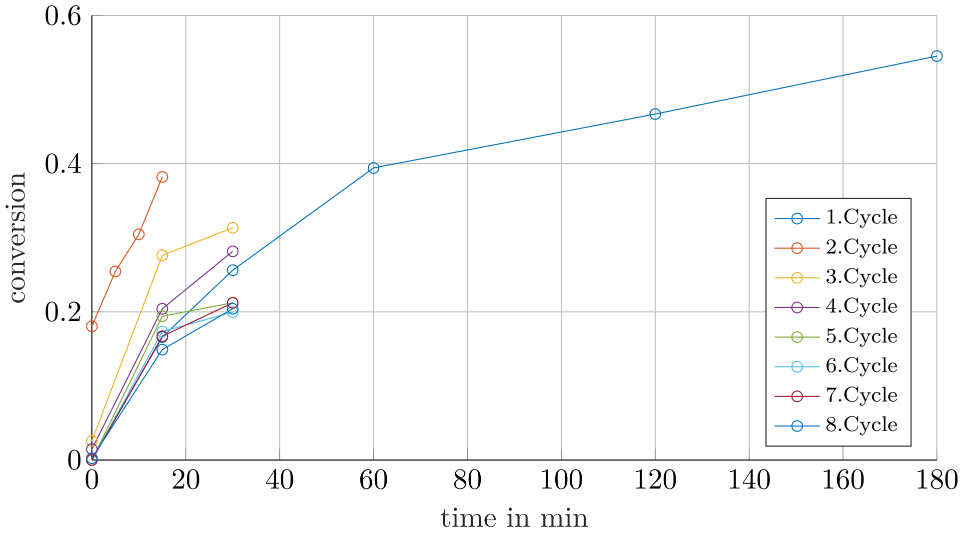

Figure 6.9: Cycle exp. 4: Conversion for carbonate-based MgO(2), 8 Cycles, material remains in reactor, 30 min hydration, shortened dehydration

Cycle experiment 4 is depicted in Fig. 6.9. Final conversion for the first hydration reaction is similar to cycle experiment 2. Because dehydration time is shortened even further, full conversion is (unintentionally) not reached. This seems to have a considerable influence on all consecutive cycles. Not only cycle 2 hydration is slower[1], but all following hydration reactions are hampered too, despite the fact that dehydration is complete from second cycle dehydration on. This suggests involvement of crystallographic processes, which need further investigation and are not described by the surface area alone. The question on why end conversion (considering all hydration experiments) never exceeds 80 % (or even stays far below) could also be worth investigating.

Once again looking at Fig. 6.9, also shows consistent decrease in conversion with every consecutive cycle. Here, cycle 3 is the fastest. For cycle 2 hydration, resolution is increased and one sample every 5 minutes is taken. In this particular instance, conversion seems to change linearly with time, i. e. conversion rate is constant. Unfortunately, the only hydration reaction is chosen, where dehydration is not complete, thus making transferability to other reactions difficult at best. Again Mastersizer analysis does not show any influence on particle size.

Hydroxide-based material is tested with cycle experiment 5 (Fig. 6.10). As expected, the first cycle hydration reaction is the fastest, because initial material is $Mg(OH)_2$ and hence the porosity increasing dehydration reaction is carried out first. Dashed lines again are given for easier comparability to carbonate-based material. Results show lower conversion rates within the first 30 min, but a higher value after 60 min. Consecutive cycles show rapid degradation.

Particle size distribution considering this cycle experiment shows some interesting changes (Fig. 6.11). Samples for the first and second cycle are taken from dehydrated material. The third cycle sample is from one hour hydrated material. During the first dehydration, par-

---

[1] Here another influencing factor has to be considered: reaction kinetics are a function of conversion (see Eq. 3.22). Since hydration reaction in cycle 2 starts at $\alpha = 0.2$, reaction rates will be slower due to this fact. A deceleratory model can be assumed.

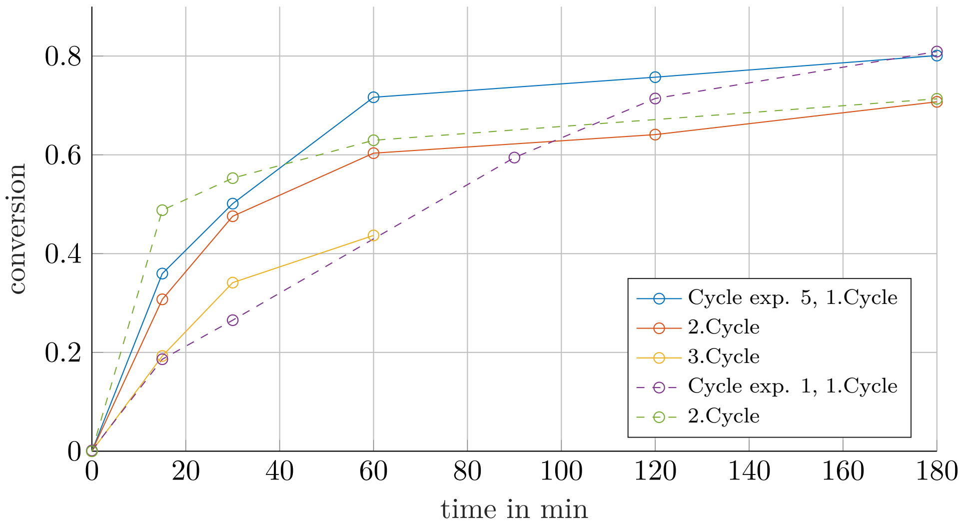

Figure 6.10: Cycle exp. 5: Conversion for hydroxide-based $Mg(OH)_2$, 3 Cycles, for comparison the first two cycles from Fig. 6.6 are given

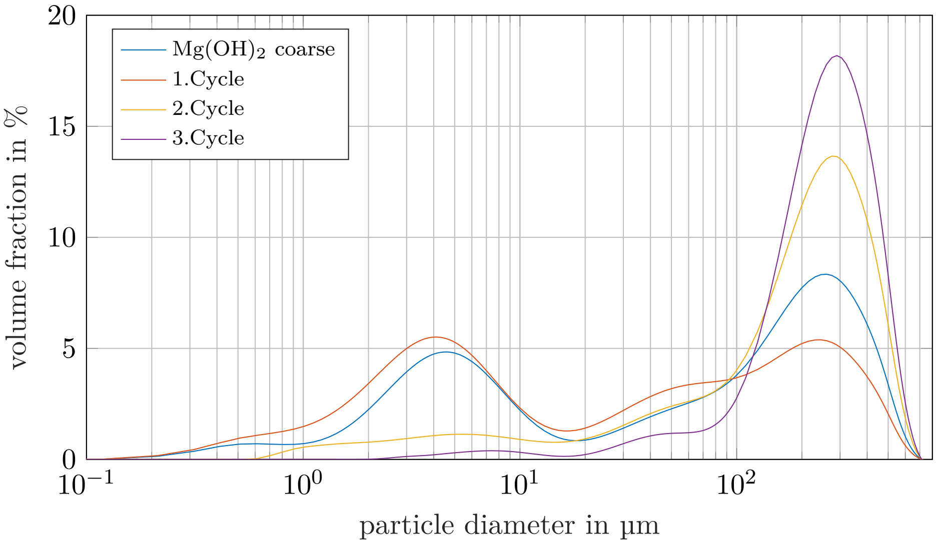

Figure 6.11: Cycle exp. 5: Particle size distribution for hydroxide-based MgO, 3 Cycles

ticles seem to fragment. Dust fraction increases proportionately, together with the fraction between 10 µm and 100 µm. This complies with Mastersizer analysis for dehydration experiments (Fig. 6.5). Looking at consecutive cycles, these fractions seem to be carried out. For following cycles this implies, that either no fragmentation occurs, or fragments are carried out right away. Since the third cycle sample is from hydrated material, the curve's shape can be influenced by the reaction as well.

Table 6.2: SSA of cycle experiments

	SSA in $\frac{m^2}{g}$				
	Cycle exp. 1	Cycle exp. 2	Cycle exp. 3	Cycle exp. 4	Cycle exp. 5
Cycle 1	~50	~50	~50	~50	301.43
Cycle 2	253.53	231.5	261.83	149.5 (181.2)[a]	299.03
Cycle 3	270.87	267.22		201.93	272.48
Cycle 4	261.27			185.34	
Cycle 5	249.90			176.08	
Cycle 6	241.17			169.18	
Cycle 7				158.19	
Cycle 8				153.80	

[a] Value in brackets is corrected to pure MgO, because dehydration was incomplete and sample consists of a MgO/$Mg(OH)_2$ mixture. It is assumed, that the $Mg(OH)_2$ still has the initial SSA of the carbonate-based MgO (50 $\frac{m^2}{g}$)

Specific surface area (SSA)

In Table 6.2 SSA for all cycle experiments are listed. Values are given for dehydrated material. Results are very consistent. All experiments result in a large increase in surface area during the first dehydration reaction. All carbonate-based samples have in common, that SSA reaches a maximum after second cycle dehydration[2]. This is believed to be the result of incomplete hydration during the first cycle, as was discussed above.

Cycle experiment 2 shows lower SSA for the second cycle compared to cycle experiment 1. Again, lower conversion during first cycle hydration and shortened dehydration time are the influencing factor. In this case, third cycle values are almost equal again, rendering the material's history insignificant.

Cycle exp. 3 shows the highest value at 261.83 $\frac{m^2}{g}$. Since first cycle conversion is highest with this experiment, the result strengthens the above made assumption.

Cycle experiment 4 does not only show lower conversion rates, but also lower SSA with a maximum value of 202 $\frac{m^2}{g}$. Incomplete dehydration during cycle 1 is believed to be the cause. One possible crystallographic process is identified. Dehydration is accompanied by formation of nanostructered MgO crystals. If dehydration is incomplete, these crystals might not be formed throughout the material, but bigger $Mg(OH)_2$ crystals are retained. This results in a reduced SSA compared to fully converted material. Completeness of the formation process during first cycle dehydration turns out to be crucial for all following cycles as well. If small MgO crystals are not formed during first cycle dehydration, later attempts do not allow this formation process to be repeated.

From the third cycle on, all carbonate-based experiments show successive decrease in SSA. This deterioration can be caused by the already mentioned formation of $MgCO_3$ by carbon dioxide. Magnesium carbonate does not decompose under investigated dehydration conditions, resulting in a successive accumulation and therefore reduced surface area. This is just one possible, unproven explanation and many other unknown crystallographic alterations can cause this

---

[2] Second cycle dehydration equals the surface area available for third cycle hydration. Hence the allocation to cycle 3 in Table 6.2.

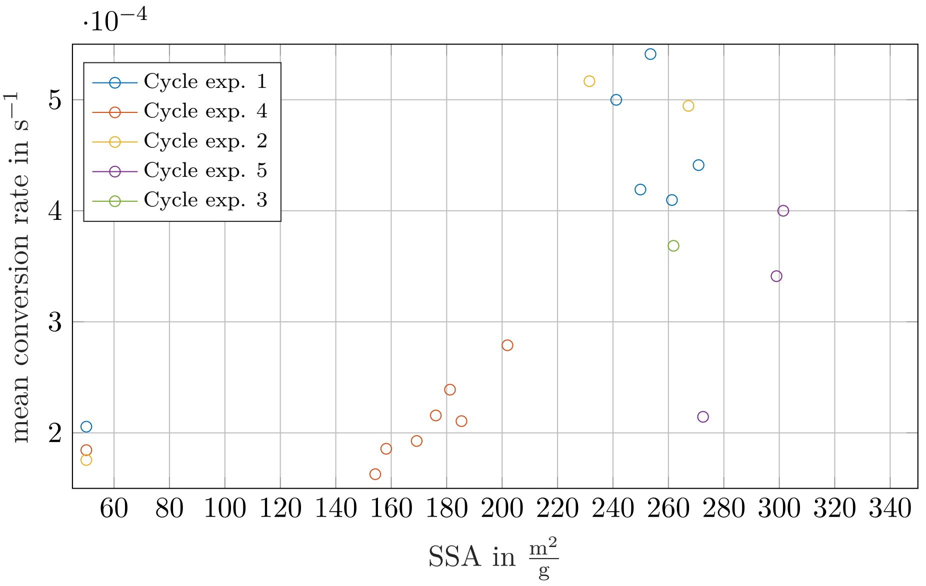

Figure 6.12: Correlation of SSA and reaction rate

deterioration.
Hydroxide-based material (cycle exp. 5) exhibits the highest SSA after initial dehydration (over 300 $\frac{m^2}{g}$), with a successive decrease afterwards. This is again explained by the fact, that hydroxide-based material consists of (almost) pure $Mg(OH)_2$. Thus allowing a full transformation to MgO and therefore maximization of surface area.

In order to correlate SSA and conversion, Fig. 6.12 is depicted. Mean conversion rate for hydration is simply calculated by taking XRD results for conversion at minute 15 and division by this time. This should be representative and close to true conversion rates.
For now, purple data points from cycle experiment 5 (hydroxide-based) are not taken into consideration. On the lower left edge, data points for the initial hydration reactions are depicted. All other points are from consecutive cycles. A clear trend is visible from the data. The cluster between 230 $\frac{m^2}{g}$ and 270 $\frac{m^2}{g}$ shows high conversion rates at $4 \times 10^{-4}\,s^{-1}$ to $5.5 \times 10^{-4}\,s^{-1}$. The second cluster relates to cycle experiment 4 and shows much lower conversion rates ($1.6 \times 10^{-4}\,s^{-1}$ to $2.8 \times 10^{-4}\,s^{-1}$) at SSA between 154 $\frac{m^2}{g}$ to 202 $\frac{m^2}{g}$. This drop is quite drastic and reaction rates diminish to initial levels, despite the more than three times larger surface area. This demonstrates involvement of crystallographic processes not covered by SSA, as was mentioned above.
For cycle experiment 4, correlation between SSA and reaction rate is clearly visible. Data points align almost perfectly and suggest a linear dependency. For other carbonate-based cycle experiments this is not unambiguously given. Cycle experiment 5 , utilizing hydroxide-based material, shows different behavior. SSA are higher, but corresponding reaction rates do not reach the same level as carbonate-based material. Also, fast degradation is clearly visible, even though SSA only diminish slightly. The lower reaction rates at higher surface areas could be explained by a different particle porosity. Surface area is determined by the size of $Mg(OH)_2$ crystals and not by the particle's porosity, i. e. two particles with the same value for SSA can still exhibit different particle morphology. This can influence transportation of steam to the

actual reaction site (e. g. diffusion) and therefore impact reaction rates.
As a conclusion, it can be said, that SSA reflects material degradation very well (cf. Table 6.2) and a good correlation between SSA and reaction rate is found. However, other factors, such as the material's pretreatment and its origin (carbonate/hydroxide) seem to have an influence as well. If not only kinetics is considered, but fluid dynamics (how steam is transported to its reaction site) too, differences in the particles' internal structure can impact results.

6.6 Further assessment

Discharge power

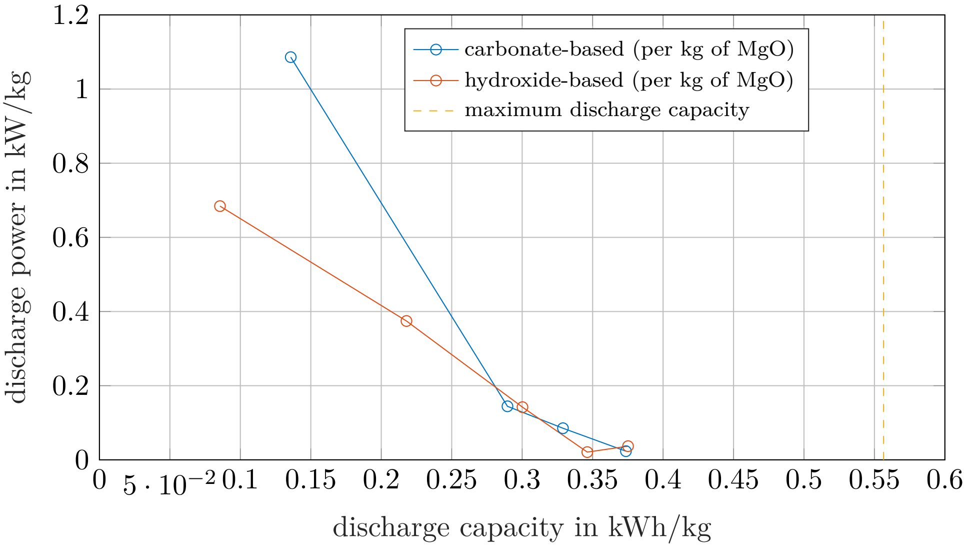

Figure 6.13: Correlation of discharge power and discharge capacity

In order to get a better understanding of the applicability considering this technology, Fig. 6.13 depicts the correlation between discharge power and discharge capacity. Results are displayed for the second cycle hydration reaction for carbonate-based material (cycle experiment 1) and hydroxide-based material (cycle experiment 5). Discharge capacity is simply calculated by multiplying conversion, obtained from XRD measurements, with theoretical reaction enthalpy. Discharge power results from division of difference in conversion between two data points by the corresponding time span. Discharge capacity is therefore calculated by taking conversion at the arithmetic mean time.
Results show an initially higher discharge power for carbonate-based material at 1.09 $\frac{\mathrm{kW}}{\mathrm{kg}}$ compared to 0.68 $\frac{\mathrm{kW}}{\mathrm{kg}}$ for hydroxide-based material. Once discharge capacity proceeds to 0.35 $\frac{\mathrm{kW\,h}}{\mathrm{kg}}$, both discharge powers drop to almost zero. This implies, that about 40 % of the material's capacity remains unused, if a technically practical performance is assumed. A short calculation is given, to illustrate the practical application. If a discharge power of 5 MW is assumed, 5000 kg of carbonate-based material is needed, if the reaction is operated at 1 $\frac{\mathrm{kW}}{\mathrm{kg}}$. This can only be done at the cost of storage capacity. Only 27 % of the theoretical maximum or 750 kW h can be stored. If a lower discharge power is accepted, more material is needed to meet the required value. For example, 25 t at 0.2 $\frac{\mathrm{kW}}{\mathrm{kg}}$.

Comparison to STA

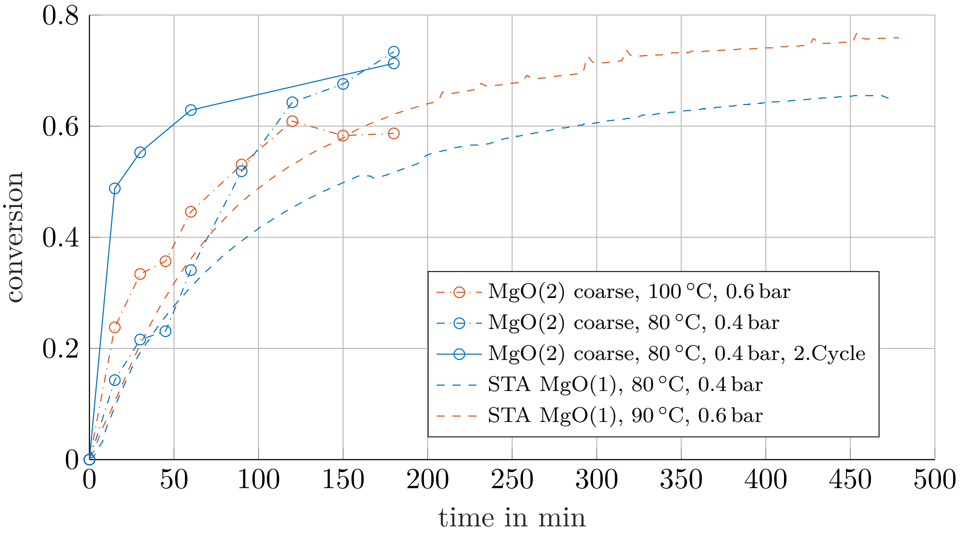

Figure 6.14: Comparison of measured conversion of STA and fluidized bed

Fig. 6.14 compares results from hydration experiments conducted in this work, to results obtained from lab-scale STA (simultaneous thermal analysis). Two parameter settings are compared, namely 0.4 bar and 80 °C and 0.6 bar and 100 °C. Note, that the STA data set for 0.6 bar is only available at 90 °C, which kinetically favors these results. Also, STA is carried out on MgO(1), fluidized bed reactions with MgO(2). This could influence results as well. Nevertheless comparison shows improved kinetics for fluidized bed experiments. STA is performed on a lab-scale with sample sizes of 40 mg to 50 mg allowing reactions under optimal conditions. The fluidized bed reactor on the other hand utilizes 400 g of material in a considerably larger testing plant. Here, fluid and thermodynamic effects cannot be neglected. This should stress, that despite the scale-up, kinetics have improved. The second cycle hydration reaction depicted, can of course not be directly compared to STA results, because STA is only done on initial material.

Comparison to literature

Bhatti et al. [3] already concluded in 1984, that MgO shows low reactivity but can be activated by a low temperature dehydration process. Pimminger et al. [46] and McKelvy et al [43] investigated the dehydration process more recently and confirmed that dehydration at low temperatures allows creation of nanostructured MgO crystals within the parent $Mg(OH)_2$ crystal, resulting in both high porosity and large SSA. This work is able to confirm these findings. Pimminger et al. were able to create surface areas of 317 $\frac{m^2}{g}$ but only at a conversion of 70 % at 370 °C and 3 h. Fluidized bed experiments result in much faster dehydration. After 75 min at 370 °C full conversion is reached. SSA is, however, lower at 223 $\frac{m^2}{g}$.
Kato et al. [34] conducted a kinetic study of the hydration of magnesium oxide. For sample preparation, they dehydrated material at 350 °C for 60 min and applied vacuum (1.3 kPa). Decreased pressure has a significant influence on dehydration kinetics. Maximum conversion was already reached after about 25 min. Both Pimminger et al. and Kato et al. found, that

reaction rates slow down after 90 % conversion. The latter even states that conversion does not proceed further. As already mentioned, XRD results in this work do not show this. TG analysis does, however, suggest the same[3].

Hydration experiments, following Kato et al., show somewhat similar behavior as result obtained in this work. Comparability is, however, limited, because different parameters (110 °C and 0.47 bar) as well as very fine powder (20 µm) is used. Second cycle hydration shows about 43 % of conversion after 15 min and 65 % after 2 h. Hydration is therefore not complete either and reaches values similar to findings in this work. Starting material is, however, already conversed to about 10 %, according to the above mentioned incomplete dehydration. From 10 % to 20 % conversion, weight increase proceeds almost instantaneously.

They propose a reaction model which includes four different processes. The first 10 % are assumed to be structural bound water in the form of inhibited $Mg(OH)_2$. The portion from 10 % to 20 % is stated to be physical adsorption, i. e. surface adsorbed water. Results in this work do not contradict. Remember, that evaluation is carried out by XRD analysis, which does not include surface water. TG analysis on the other hand, shows increased water contents after hydration. Kato et al. only measure weight change and not material composition. It is therefore possible, that the water uptake occurs within the first few seconds. The third mechanism introduced by Kato is the actual chemical reaction. The last mechanism is a sorption equilibrium, made up of both the chemical reaction and an adsorption equilibrium, which would explain why conversion never reaches 100 %.

Cycle experiments were performed again by Kato et al. [33] and Ervin [17]. The former used ultra fine $Mg(OH)_2$ powder (10 nm) and found, that reactivity only reduces minimal during the first four cycles, stabilizing afterwards at 50 % conversion (parameters: 0.47 bar, 90 °C and 60 min). Ervin reports a decline from 95 % to 60 % within the fortieth cycle and stabilization for the next 460 cycles. In this work 8 cycles at the most are achieved. A decrease in reactivity is clearly given, especially for hydroxide-based material.

---

[3] Note, that only three TG analysis on hydroxide-based material are available

7 Conclusion

In the course of this work, the $MgO/Mg(OH)_2$ system as a thermochemical storage material in a fluidized bed reactor has been investigated thoroughly. Operation in a fluidized bed gives certain advantages but also potential drawbacks compared to other reactor technologies.

For the successful utilization of the $MgO/Mg(OH)_2$ system in TCES technologies, the material needs to be mechanically and chemically stable. Also, reaction kinetics need to be on a level suitable for technical applications. This work has been able to answer these questions. Additionally, optimal reaction conditions were determined and limitations of the process were pointed out.

For investigation six different batches of material were used, four of them originating from magnesium carbonate and differing in particle size distributions and burning conditions during the production process. The other two batches are hydroxide-based and are extracted from seawater.

Mechanical stability and good fluidization behavior were proven for carbonate-based material under all investigated conditions. Hydroxide-based material, however, is not as robust. Bimodal particle size distributions (main fraction + dust fraction) were identified, which are detrimental for fluidization. Both material types should be optimized for utilization in a FBR.

Chemically, varying residual carbonate contents and relatively low specific particle surface areas (i. e. large crystals) pose a main obstacle which needs to be addressed. Both issues have been identified and some possible solutions have already been applied in this work. Particle surface areas were increased up to tenfold. The formation of nanoscale crystals during the dehydration reaction at low temperatures was identified as the surface area increasing process. This surface area increase allowed hydration reactions rates to be twice as high as reaction rates using initial material. A pretreatment of the material should thus be carried out, with the aim of maximizing SSA. In order to achieve this, a full cycle with high final conversion after hydration and complete dehydration at low temperatures should be carried out, before material is utilized in a TCES process.

To find optimal reaction conditions, the hydration reaction was investigated under varying parameters of temperature and steam partial pressure. The assumption of faster kinetics with increased distance to the equilibrium curve was confirmed. In other words, lower temperatures at constant partial pressure or higher partial pressures at constant temperature lead to improved kinetics. These experiments, however, also demonstrate the limitations of the process. Further acceleration of kinetics (i. e. larger distance to the equilibrium curve) is limited by water condensation. Using liquid water is another approach, which could be another process worth investigating.

The influence of reaction time and reaction temperatures during dehydration were also shown. A result which was not anticipated is, that reaction time during dehydration, after full conversion is already reached, has an influence on SSA. This influence is outweighing the temperature dependency of SSA within the investigated temperature ranges. Further research of the reaction time dependency has the potential to improve the process considerably.

To make $MgO/Mg(OH)_2$ economically viable, the material needs to be stable over a certain number of consecutive cycles (cycle stability). Our research suggests, that high levels of cycle stability can be achieved with carbonate-based material, if pretreatment conditions are optimized. Hydroxide-based material was not able to compete with carbonate-based material in this matter. Also, a relation between SSA and conversion during hydration was found. SSA is able to describe material deterioration to some extent. Other crystallographic processes, however, impact results as well. These unidentified processes should be the topic of further research. Limited end conversion during hydration is another issue, which cannot be explained, so far. A shift of the rate limiting step towards product layer diffusion could be the answer, if experiments can confirm this assumption.

This work has also been able to demonstrate the advantages of a FBR. Compared to lab-scale STA experiments, kinetic improvement was achieved, rendering the application of a fluidized bed a promising technology for the hydration and dehydration of $MgO/Mg(OH)_2$.

An application of the $MgO/Mg(OH)_2$ system as a low temperature storage medium (e. g. as seasonal storage for solar thermal power), could pose a feasible and interesting way of increasing energetic efficiencies. After initial 'activation', MgO shows technically interesting energy discharge rates. The material's storage capacity can, however, not be fully used (about 50 %) and steam needs to be available as a waste product in order for this process to be energetically useful.

Further research is needed if the reaction system of $MgO/Mg(OH)_2$ is to be utilized commercially in TCES processes. In particular, generating more knowledge on unidentified crystallographic processes could enhance the material's applicability.

Nomenclature

Acronyms

BET	Brunnauer-Emmet-Teller
CHP	chemical heat pump
CSP	concentrating solar power plant
FBR	fluidized bed reactor
FCC	fluid catalytic cracking
GHG	greenhouse gas
IET	Institute of Energy Systems and Thermodynamics
IG	ideal gas
P&ID	piping and instrumentation diagram
PCM	phase change material
PXRD	powder X-ray diffraction
SSA	specific surface area
STA	simultaneous thermal analysis
TCES	Thermochemical energy storage
TCSC	thermochemical standard condition
TES	thermal energy storage
TGA	thermogravimetric analysis
TPES	Total primary energy supply
UI	user interface
WBGU	Wissenschaftlicher Beirat der Bundesregierung Globale Umweltveränderung

Greek symbols

β	model parameter	-
$\frac{\mathrm{d}\alpha}{\mathrm{d}t}$	conversion rate	$\frac{1}{\mathrm{s}}$
μ_g	dynamic viscosity of gas	$\frac{\mathrm{kg}}{\mathrm{m\,s}}$
μ_i	chemical potential of species i	$\frac{\mathrm{J}}{\mathrm{mol}}$
ν_i	stoichiometric coefficient of species i	-
ϕ_s	sphericity	-
ρ	density	$\frac{\mathrm{kg}}{\mathrm{m}^3}$
ε	reaction coordinate	-
ε_p	porosity or void fraction	-
φ_i	fugacity coefficient of species i	-

Indices

0	for a pure substance in Section 3.2.1, for initial state or starting time $t = t_0$ in Section 3.2.2
a	air
abs	absolute
amb	at ambient conditions
b	bulk
$calc$	theoretically calculated value
eq	at equilibrium
$evap$	evaporation
exp	experimentally determined value
f	formation
g	gas
in	control volume entry
mf	minimum fluidization
out	control volume exit
p	particle

s	steam	
t	terminal	

Latin symbols

ΔG_R	molar reaction Gibbs energy	$\frac{\mathrm{J}}{\mathrm{mol}}$
ΔH_R	molar reaction enthalpy	$\frac{\mathrm{J}}{\mathrm{mol}}$
ΔH_{ads}	adsorption enthalpy	J
Δh_{ads}	specific adsorption enthalpy	$\frac{\mathrm{J}}{\mathrm{kg}}$
Δm_i	percentage mass loss of species i	%
$\dot{m}$	mass flow rate	$\frac{\mathrm{kg}}{\mathrm{s}}$
$\dot{n}$	mole flow rate	$\frac{\mathrm{mol}}{\mathrm{s}}$
$\mathbf{n}$	vector of n_i	mol
A	pre-exponential factor	depends on system
Ar	Archimedes number	-
$c^0_{p,i}$	molar isobaric heat capacity of species i at standard pressure	$\frac{\mathrm{J}}{\mathrm{mol\,K}}$
d^*	dimensionless diameter	-
d_{SV}	diameter of a sphere with the same surface to volume ratio as the particle–also called Sauter diameter or d_{32}	m
E_a	activation energy	$\frac{\mathrm{J}}{\mathrm{mol}}$
$f(\alpha)$	differential conversion dependency	-
f_i	fugacity of species i	Pa
G	molar Gibbs energy	$\frac{\mathrm{J}}{\mathrm{mol}}$
g	gravitational acceleration	$\frac{\mathrm{m}}{\mathrm{s}^2}$
$g(\alpha)$	integral conversion dependency	-
G^t	total Gibbs energy	J
H	molar enthalpy	$\frac{\mathrm{J}}{\mathrm{mol}}$
h	specific enthalpy	$\frac{\mathrm{J}}{\mathrm{kg}}$
$h(p)$	pressure dependency	-
H^t	total enthalpy	J
$k(T)$	temperature dependency	-

M	molar mass	$\frac{\mathrm{kg}}{\mathrm{mol}}$
$m_{\mathrm{H_2O}}$	loss on ignition	g
m_{ads}	adsorbed mass	kg
n_i	molar amount of species i	mol
p	pressure	Pa
p_i	partial pressure of component i	Pa
R	universal gas constant $R = 8.314$	$\frac{\mathrm{J}}{\mathrm{mol\,K}}$
S	molar entropy	$\frac{\mathrm{J}}{\mathrm{mol\,K}}$
S^t	total entropy	$\frac{\mathrm{J}}{\mathrm{K}}$
SA	surface area	m^2
T	temperature	°C
t	time	s
$T_{1,end}$	reaction end temperature for dehydration reactions	°C
u	velocity	$\frac{\mathrm{m}}{\mathrm{s}}$
u^*	dimensionless velocity	-
V^t	volume	m^3
v_i	molar volume of species i	$\frac{\mathrm{m}^3}{\mathrm{mol}}$
w	percentage mass share	%
X	loading	$\frac{\mathrm{kg}}{\mathrm{kg}}$
x_i	molar fraction of species i	-

Superscripts

0	at standard pressure $p^0 = 1\,\mathrm{bar}$
s	at saturation

Bibliography

[1] M. R. Allen et al. “Warming caused by cumulative carbon emissions towards the trillionth tonne”. In: *Nature* 458 (2009), pp. 1163–1166.

[2] D. Aydin, S. P. Casey, and S. Riffat. “The latest advancements on thermochemical heat storage systems”. In: *Renewable and Sustainable Energy Reviews* 41 (2015), pp. 356–367.

[3] A. S. Bhatti. “Magnesia from Seawater: A Review”. In: *Clay Minerals* 19.5 (1984), pp. 865–875.

[4] A. S. Bhatti, D. Dollimore, and A. Dyer. “The rates of hydration of sea water magnesias”. In: *Surface Technology* 22.2 (1984), pp. 181–188.

[5] T. Block, N. Knoblauch, and M. Schmücker. “The cobalt-oxide/iron-oxide binary system for use as high temperature thermochemical energy storage material”. In: *Thermochimica Acta* 577 (2014), pp. 25–32.

[6] B. Bogdanović, A. Ritter, and B. Spliethoff. “Active MgH2 - Mg Systems for Reversible Chemical Energy Storage”. In: *Angewandte Chemie International Edition in English* 29.3 (1990), pp. 223–234.

[7] Bruckner T. et al. “Energy Systems”. In: *Climate change 2014*. Ed. by R. K. Pachauri and L. Mayer. Geneva, Switzerland: Intergovernmental Panel on Climate Change, 2015, pp. 511–597.

[8] Chase, M.W., Jr. “NIST-JANAF Thermochemical Tables”. In: *Journal of Physical and Chemical Reference Data*. Ed. by AIP Publishing. Vol. 9, pp. 1–1951.

[9] C. K. Clayton and K. J. Whitty. “Measurement and modeling of decomposition kinetics for copper oxide-based chemical looping with oxygen uncoupling”. In: *Applied Energy* 116 (2014), pp. 416–423.

[10] J. Cot-Gores, A. Castell, and L. F. Cabeza. “Thermochemical energy storage and conversion: A-state-of-the-art review of the experimental research under practical conditions”. In: *Renewable and Sustainable Energy Reviews* 16.7 (2012), pp. 5207–5224.

[11] M. Deutsch. “A systematic approach to identify new thermochemical energy storage systems”. Dissertation. Vienna: TU Wien, 2017.

[12] M. Deutsch et al. “Systematic search algorithm for potential thermochemical energy storage systems”. In: *Applied Energy* 183 (2016), pp. 113–120.

[13] DIN. *Measurement of fluid flow by means of pressure differential devices inserted in circular cross-section conduits running full Part 1: General principles and requirements.* 2004.

[14] DIN. *Measurement of fluid flow by means of pressure differential devices inserted in circular cross-section conduits running full Part 2: Orifice plates.* 2004.

[15] DIN. *Thermocouples – Part 1: EMF specifications and tolerances.* 2014.

[16] P. E. Dodds and S. D. Garvey. “The Role of Energy Storage in Low-Carbon Energy Systems”. In: *Storing Energy.* Elsevier, 2016, pp. 3–22.

[17] G. Ervin. “Solar heat storage using chemical reactions”. In: *Journal of Solid State Chemistry* 22.1 (1977), pp. 51–61.

[18] S. Flegkas, F. Birkelbach, F. Winter, N. Freiberger, and A. Werner. “Fluidized bed reactors for solid-gas thermochemical energy storage concepts - Modelling and process limitations”. In: *Energy* 143 (2018), pp. 615–623.

[19] S. Flegkas et al. “Thermochemical Energy Storage Concept Based on a Reactor Cascade with Different Storage Materials”. In: *International Journal of Contemporary ENERGY* 4 (2018), pp. 40–49.

[20] S. Flegkas. “Thermochemical energy storage concept based on a fluidized bed reactor cascade with different storage materials and an internal chemical condensator for waste heat recovery”. In: *Wissens/Transfer/Ost* MO62/2016 (2016).

[21] S. Fujimoto, E. Bilgen, and H. Ogura. “CaO/Ca(OH)2 chemical heat pump system”. In: *Energy Conversion and Management* 43.7 (2002), pp. 947–960.

[22] M. I. Gasik. “Technology of Ferroalloys with Alkaline-Earth Metals”. In: *Handbook of Ferroalloys.* Elsevier, 2013, pp. 471–494.

[23] M. Grasserbauer. *Ecology and Sustainable Development.* 2015.

[24] W. M. Haynes. *CRC Handbook of Chemistry and Physics, 93rd Edition.* Baton Rouge, UNITED STATES: CRC Press, 2016.

[25] K. Heinloth. “1 Survey of renewable energy”. In: *Renewable Energy.* Ed. by K. Heinloth. Vol. 3C. Landolt-Börnstein - Group VIII Advanced Materials and Technologies. Springer Berlin Heidelberg, 2006, pp. 1–10.

[26] H. Hofbauer. “Wirbelschichttechnik”. TU Wien, 2017.

[27] S. Hongois, F. Kuznik, P. Stevens, and J.-J. Roux. “Development and characterisation of a new MgSO4−zeolite composite for long-term thermal energy storage”. In: *Solar Energy Materials and Solar Cells* 95.7 (2011), pp. 1831–1837.

[28] J. E. House. *Principles of Chemical Kinetics.* 2. Aufl. s.l.: Elsevier professional, 2007.

[29] ieso. *power data.* 2016.

[30] IFA Institut für Arbeitsschutz der Deutschen Gesetzlichen Unfallversicherung. *GESTIS Stoffdatenbank.*

[31] International Energy Agency. *World Energy Outlook 2011.* Organization for Economic, 2011.

[32] International Energy Agency. *World Energy Outlook 2017 -.* Paris: OECD Publishing, 2017.

[33] Y. Kato, J. Nakahata, and Y. Yoshizawa. “Durability characteristics of the hydration of magnesium oxide under repetitive reaction”. In: *Journal of Materials Science* 34.3 (1999), pp. 475–480.

[34] Y. Kato, N. Yamashita, K. Kobayashi, and Y. Yoshizawa. “Kinetic study of the hydration of magnesium oxide for a chemical heat pump”. In: *Applied Thermal Engineering* 16.11 (1996), pp. 853–862.

[35] H. Kerskes. “Thermochemical Energy Storage”. In: *Storing Energy.* Elsevier, 2016, pp. 345–372.

[36] D. Kunii, O. Levenspiel, and H. Brenner. *Fluidization Engineering.* 2nd ed. Burlington: Elsevier Science, 1991.

[37] D. Lager. “Evaluation of thermophysical properties for thermal energy storage materials - determining factors, prospects and limitations”. Dissertation. TU Wien, 2017.

[38] Leister. *Leister LHS 61S.* https://www.leister.com/en/process-heat/processes/lhs-61s-system.

[39] T. Li, R. Wang, J. K. Kiplagat, and Y. Kang. “Performance analysis of an integrated energy storage and energy upgrade thermochemical solid–gas sorption system for seasonal storage of solar thermal energy”. In: *Energy* 50 (2013), pp. 454–467.

[40] B. Liu, P. S. Thomas, A. S. Ray, and J. P. Guerbois. “A TG analysis of the effect of calcination conditions on the properties of reactive magnesia”. In: *Journal of Thermal Analysis and Calorimetry* 88.1 (2007), pp. 145–149.

[41] D. Mather. *Energy Conversion.* University of Waterloo, December 2016.

[42] H. Matsuda, T. Ishizu, S. K. Lee, and M. Hasatani. “Kinetic study of Ca(OH)2/CaO reversible thermochemical reaction for thermal energy storage by means of chemical reaction”. In: *KAGAKU KOGAKU RONBUNSHU* 11.5 (1985), pp. 542–548.

[43] M. J. McKelvy, R. Sharma, A. V. G. Chizmeshya, R. W. Carpenter, and K. Streib. “Magnesium Hydroxide Dehydroxylation: In Situ Nanoscale Observations of Lamellar Nucleation and Growth”. In: *Chemistry of Materials* 13.3 (2001), pp. 921–926.

[44] Mineralogical Society of America. *Handbook of Mineralogy.*

[45] P. Pardo, A. Deydier, Z. Anxionnaz-Minvielle, S. Rougé, M. Cabassud, and P. Cognet. “A review on high temperature thermochemical heat energy storage”. In: *Renewable and Sustainable Energy Reviews* 32 (2014), pp. 591–610.

[46] H. Pimminger, G. Habler, N. Freiberger, and R. Abart. “Evolution of nanostructure and specific surface area during thermally driven dehydration of Mg(OH)2”. In: *Physics and Chemistry of Minerals* 43.1 (2016), pp. 59–68.

[47] R. C. Ropp. “Group 16 (O, S, Se, Te) Alkaline Earth Compounds”. In: *Encyclopedia of the Alkaline Earth Compounds.* Elsevier, 2013, pp. 105–197.

[48] D. Saecker. “Ende der Verunsicherung Ende der Verunsicherung: DIN EN 60751:2009 legitimiert den industriellen Einsatz vieler Platin-Widerstandsthermometer”. In: *Chemical plants & processes : CPP : international journal of chemical and pharmaceutical engineering* 3 (2010).

[49] F. Schaube, L. Koch, A. Wörner, and H. Müller-Steinhagen. “A thermodynamic and kinetic study of the de- and rehydration of Ca(OH)2 at high H2O partial pressures for thermo-chemical heat storage”. In: *Thermochimica Acta* 538 (2012), pp. 9–20.

[50] M. A. Shand. *The Chemistry and Technology of Magnesia.* Hoboken, NJ, USA: John Wiley & Sons, Inc, 2006.

[51] A. Sharma, V. V. Tyagi, C. R. Chen, and D. Buddhi. “Review on thermal energy storage with phase change materials and applications”. In: *Renewable and Sustainable Energy Reviews* 13.2 (2009), pp. 318–345.

[52] A. Solé, I. Martorell, and L. F. Cabeza. "State of the art on gas–solid thermochemical energy storage systems and reactors for building applications". In: *Renewable and Sustainable Energy Reviews* 47 (2015), pp. 386–398.

[53] A. Stoppato and A. Benato. "The Importance of Energy Storage". In: *Energy Storage*. Ed. by G. M. Crawley. Vol. 04. World Scientific Series in Current Energy Issues. World Scientific, 2017, pp. 1–26.

[54] Thangaraj N., Westmacott K., and Dahmen U. "HVEM Studies of the Sintering of MgO Nanocrystals Prepared by Mg(OH)sub 2 Decomposition". In: *Ultramicroscopy* 27 (1991), pp. 362–374.

[55] *VDI-Wärmeatlas: Mit 320 Tabellen*. 11., bearb. und erw. Aufl. VDI-Buch. Berlin: Springer Vieweg, 2013.

[56] Wissenschaftlicher Beirat der Bundesregierung Globale Umweltveränderung. *Welt im Wandel: Gesellschaftsvertrag für eine große Transformation: Hauptgutachten*. Berlin and Deutschland, 2011.

[57] Wong B., Brown L., and Schaube F. "Oxide Based Thermochemical Heat Storage". In: *Proceedings of 16th Annual Solar PACES Conference*. 2010.

[58] W. Wongsuwan, S. Kumar, P. Neveu, and F. Meunier. "A review of chemical heat pump technology and applications". In: *Applied Thermal Engineering* 21.15 (2001), pp. 1489–1519.

List of Figures

List of Tables

Appendix

A.1 Hydration

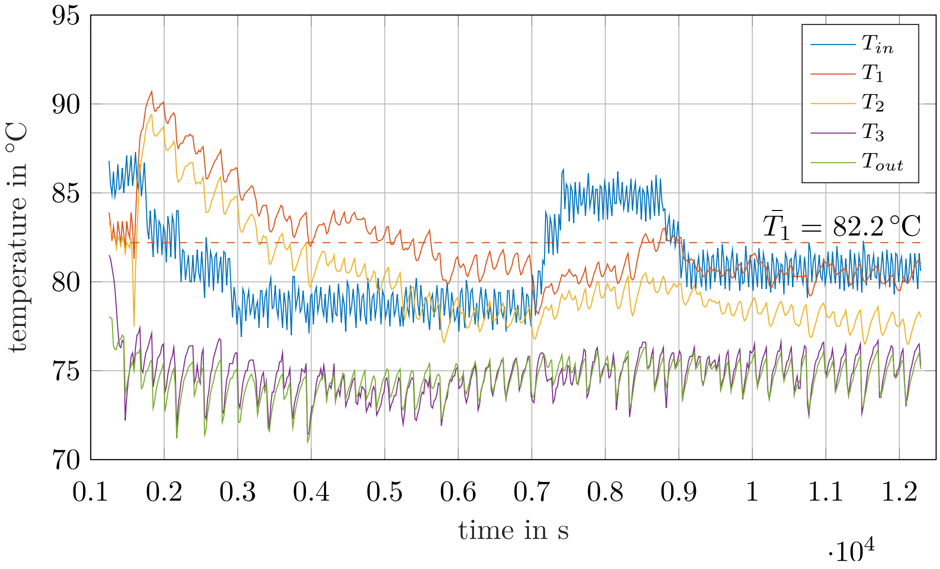

Figure A.1.1: Temperature curves of hydration reaction at 0.4 bar and 80 °C, MgO(2) coarse

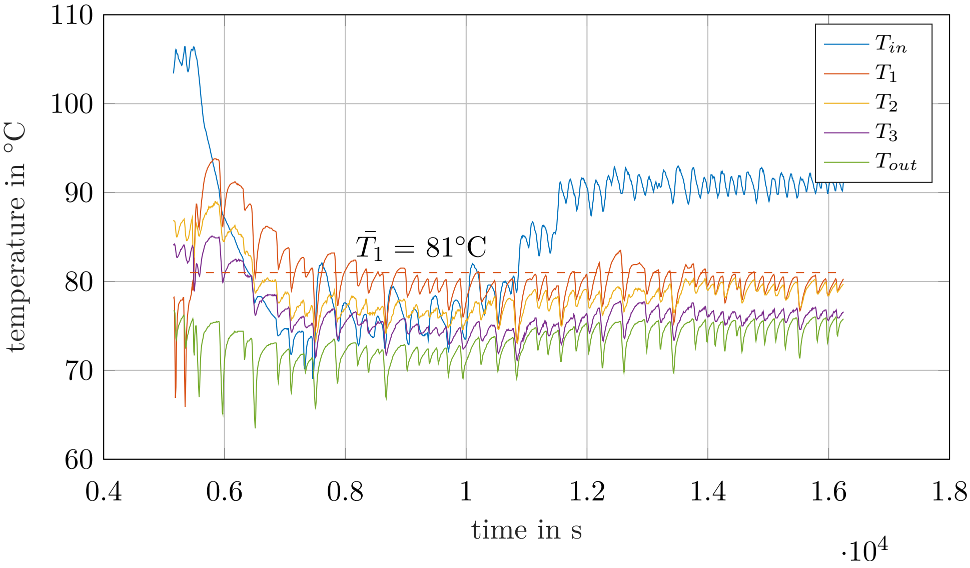

Figure A.1.2: Temperature curves of hydration reaction at 0.4 bar and 80 °C, MgO(2) fine

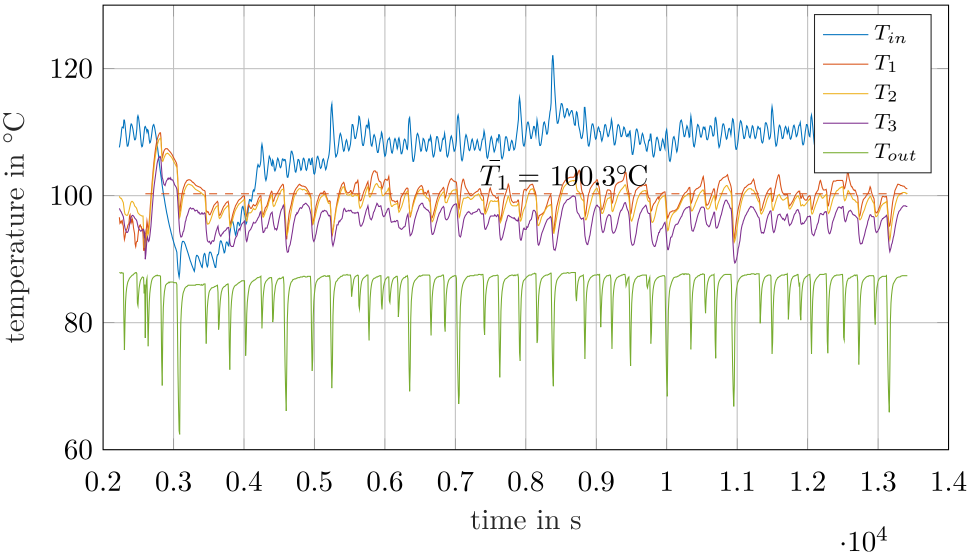

Figure A.1.3: Temperature curves of hydration reaction at 0.6 bar and 100 °C, MgO(2) coarse

The two collapses in temperatures seen with the MgO(2) coarse reaction at 0.4 bar and 100 °C (Fig. A.1.4) are not caused by condensation. Here, the reaction was shortly stopped because material is taken out of the reactor using the tube, as explained above. (This reaction is the first one done with sample extraction. A method on how to get the material out had to be found first. This made the interruptions necessary.) With all other reactions, sample extraction is done without interruption of the reaction. The same reaction also shows an increase in temperature within the last 20 minutes. This cannot be explained because conditions are unchanged. The initial temperature drop followed by the increase would be characteristic for material being added to the reactor (which is not done).

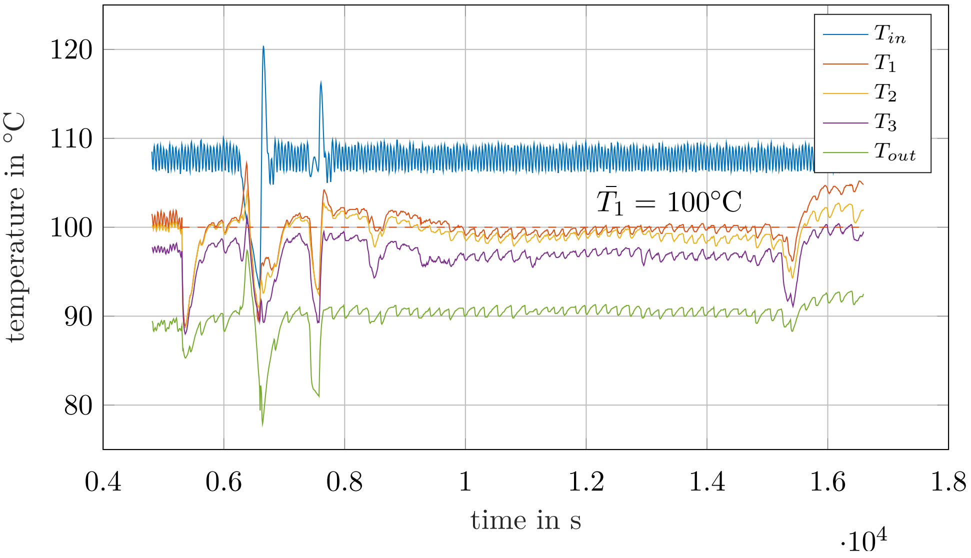

Figure A.1.4: Temperature curves of hydration reaction at 0.4 bar and 100 °C, MgO(2) coarse

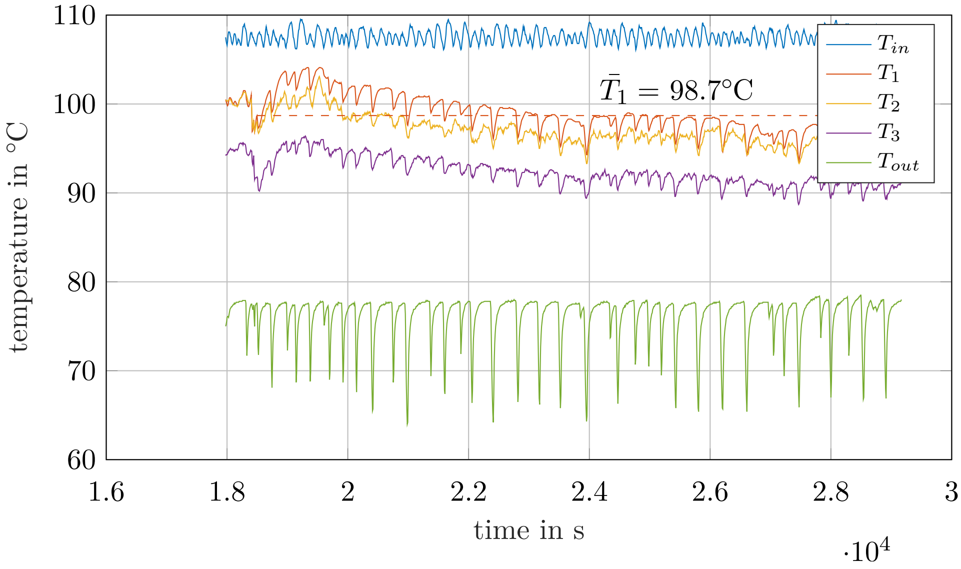

Figure A.1.5: Temperature curves of hydration reaction at 0.4 bar and 100 °C, MgO(2) fine

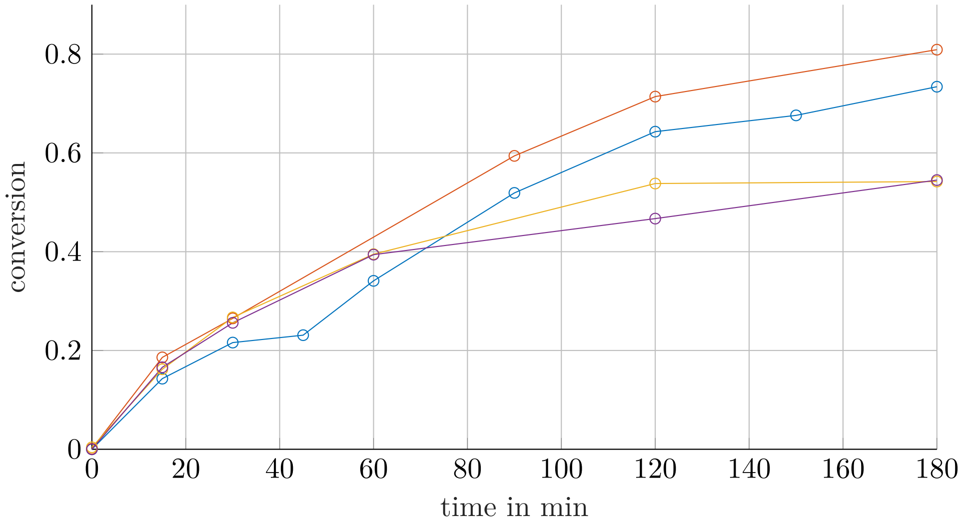

Figure A.1.6: Comparison of XRD results from the four conducted first cycle hydration experiments

A.2 Cycle experiments

The temperature surge between seconds 6000 and 7000 is caused by a malfunction of the plant. The experiments is actually interrupted here and continued later. Restarting results in a renewed temperature increase. The reason are circuit breakers, which are installed in the power supply circuit. They should be avoided in industrial plants. Power interruption occurs multiple times during experimentation, making experiment repetitions necessary.

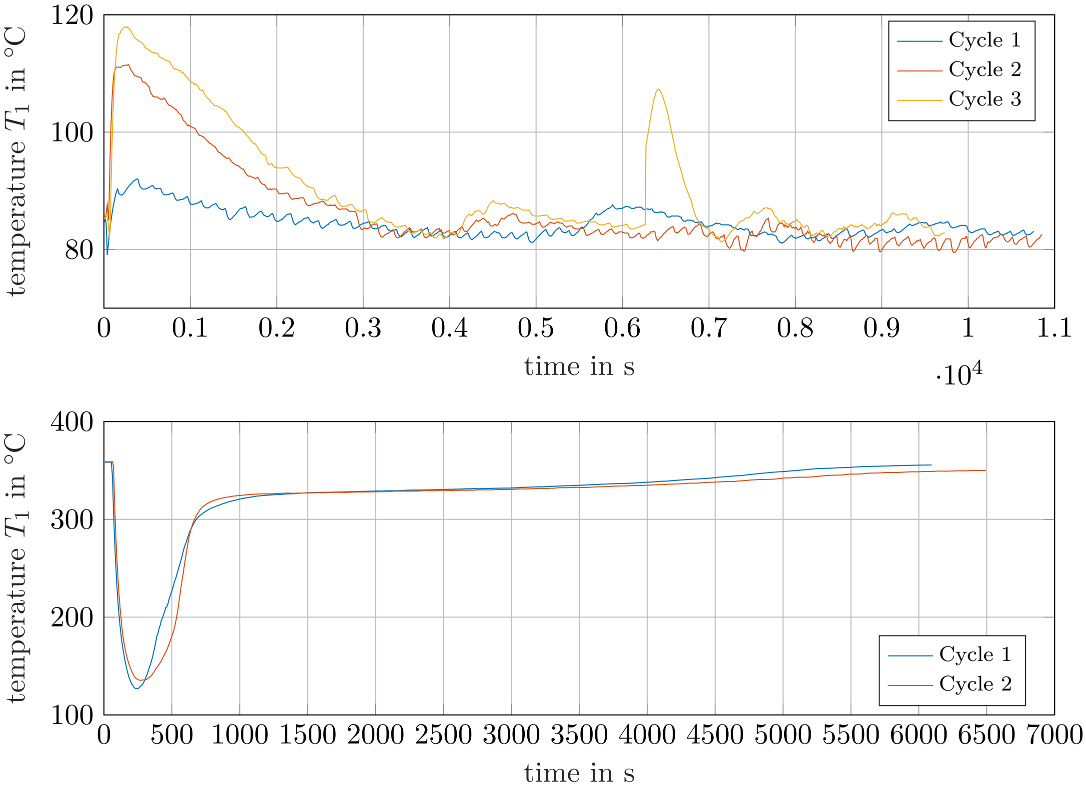

Figure A.2.1: Temperature curves of cycle experiments with carbonate-bases MgO(2) coarse, shorter dehydration reaction